UNIVERSITY OF BIRMINGHAM

Exploring the Behaviour of Capped Metal Nanoparticles on Metallic Surfaces

By

Nashwa Awais

A thesis submitted to the University of Birmingham for the degree of

DOCTOR OF PHILOSOPHY

School of Chemistry

College of Engineering and Physical Sciences

University of Birmingham

December 2024

Abstract

Thiolated gold nanoparticles are known to undergo a redistribution of their capping layer upon immobilisation onto gold substrates, leading to the disintegration of both the ligand shell and the Au core. In-depth characterisation of these systems has demonstrated that this decomposition arises from a balance between entropic and enthalpic factors, which are influenced by substrate reactivity.

This thesis explores the behaviour of mixed metal systems to investigate how variations in the substrate and nanoparticle materials affect nanoparticle stability and the resultant surface properties. Systems of Au, Ag, and Pt nanoparticles (NPs) immobilised onto complementary substrates were studied to evaluate their stability and structural evolution, with particular attention given to whether the properties of the modified surfaces reflect those of the substrate, the nanoparticle core, or new properties arising from interactions between the two metals.

The central aim of this work was to examine how the substrate material influences the stability, chemical identity, and functionality of immobilised nanoparticles, providing new insights into the design principles for nanoparticle-based surfaces. Combinations of Ag NPs on Au and Pt, Pt NPs on Au and Ag, and Au NPs on Pt and Ag were investigated using scanning tunnelling microscopy (STM), X-ray photoelectron spectroscopy (XPS), and cyclic voltammetry.

The thesis is structured as follows: Chapter 1 introduces the foundational work on the Au NP–Au substrate system, identifies key driving forces in mixed metal combinations, and outlines the experimental techniques employed. Chapter 2 details the materials and

methodologies used in the experimental work. Chapter 3 examines the modification of Au and Pt substrates with Ag NPs, characterising the resulting surfaces and their electrochemical properties. Chapter 4 explores Pt NPs immobilised onto Au and Ag substrates, while Chapter 5 focuses on Au NPs deposited onto Pt and Ag substrates. Finally, Chapter 6 summarises the findings across these configurations, discusses their implications, and identifies potential directions for future research.

Dedication

بِسْمِ اللَّهِ الرَّحْمَنِ الرَّحِيم

In the name of God, the Most Gracious, the Most Merciful

I would like to take this space to dedicate this thesis to my parents, Onaiza and Awais. You have both sacrificed so much in life to provide for us, keep us safe, and to allow us to embrace every opportunity. I am eternally grateful to you both.

I am extremely lucky to have so many wonderful people in my life, all of whom deserve their flowers for the support they have shown me throughout my studies. Asharab, for always being a source of strength and love. You're not only my brother, but my best friend. My sister Hina, for the sleepovers, movie nights, and for all the love you give. Khala and Afi Mamu, for always taking care of me so lovingly. Mamu Chand, for always making me laugh and encouraging me to see the best in a bad situation.

My wonderful husband Suhail, your constant light and love has pushed me through to the end. Words cannot express how much you mean to me. For you, I will be forever thankful.

To Ammi, Dad, Alisha and Akib, thank you for embracing me and supporting me, and always checking I'm on track.

My beautiful friends, sixteen years of friendship and still you all bring continuous laughter and joy into my life. Thank you for being there for all the ups and downs!

Finally, Junior, Ghost and Casper. One of you started this journey with me, and two of you are here for the end. I love you all.

Acknowledgements

I would like to thank my supervisors, Professor Tim Albrecht and Dr Paramaconi Rodriguez. Thank you both for the initial opportunity to join your groups, and all the subsequent guidance you have given me. Para, thank you for everything. I wish you had stayed, but I'm glad for the success you have found. Tim, thank you for all your patience, and for helping me remain focused whenever things became overwhelming.

I would like to thank all of my colleagues, past and present. Thank you to Chris for your camaraderie, and your continued help even after your time at the university ended. Lauren, thank you for the zoom calls and to-do lists – we got back on track! Joe, you've been a great friend both in and out of university, thank you for everything. A big thank you to Jake for being the best lab buddy and a great friend. Rand, Oliver and Cengiz, you've all helped me in so many ways, and I appreciate you all very much.

I would like to thank Santiago M. Solans and Pilar Cea at the University of Zaragoza, for their contributions with XPS measurements and analysis. I would also like to acknowledge Yisong Han and the Electron Microscopy Research Technology Platform, University of Warwick, for their help in TEM imaging.

Table of Contents

Contents

1. Introduction

Chapter Contents

Small metal nanoparticles (NPs) have garnered significant attention due to their unique electronic, optical, and catalytic properties, which often lie between those of bulk materials and molecular systems. Their size-dependent properties can offer increased sensitivity and selectivity, making them highly desirable in applications ranging from catalysis to electronics and sensing.[1–4] To harness these properties effectively, immobilising nanoparticles onto macroscopic substrates is a crucial step in the design of functional surfaces.

Functional surfaces created with immobilised nanoparticles may find applications in a range of fields. For instance, catalytic surfaces containing different active materials can catalyse multiple reactions simultaneously, leveraging the selectivity of each component to significantly increase the efficiency and applicability of a single catalytic surface. Similarly, in sensing and electronic applications, the interplay between the nanoparticle and the substrate can produce enhanced sensitivity.

Despite their promise, the long-term use of small metal nanoparticles is often limited by their inherent instability. Stable operation - defined as the retention of atomic arrangement, overall structure, and chemical identity - is essential for ensuring the continued functionality of nanoparticles immobilised onto substrates. When nanoparticles lose stability, they may dissolve, aggregate, or undergo chemical transformations, which can compromise the properties of the surface over time.

Nanoparticles are often kinetically stabilised through the use of ligand-based protective layers.[4,5] The ligand capping layer is a crucial factor for the effective use of nanoparticles, as it ensures particle stability while allowing surface sites to remain accessible. Various methods exist to remove thiols from supported nanoparticles, such as annealing or high-

temperature treatments. However, these processes can affect the shape and size of the nanoparticles, potentially altering properties such as their catalytic activity.[6,7]

This work focuses on the influence of substrate material on nanoparticle stability, a critical factor in advancing the design of functional surfaces that remain stable and effective over extended periods of operation. By investigating how substrate materials affect the stability, chemical identity, and functionality of immobilised nanoparticles, this study aims to provide new insights into the design principles for nanoparticle-based surfaces.

1.1 Modification of Au substrates with Au Nanoparticles

The characterisation of Au nanoparticle immobilisation on Au single crystal substrates has demonstrated the significant influence of substrate reactivity on nanoparticle stability. More detailed investigations into the modified surface have revealed that the underlying instability and particle decomposition processes are complex and multifaceted. Key studies on this system are highlighted here to provide a foundation for the work presented in this thesis.

1.1.1 Structure of Some Thiolated Au Nanoparticles

The literature under consideration focuses on Au nanoparticles of two sizes, stabilised with a thiol capping layer of 1-hexanethiol (HT). The particle systems examined are $Au_{25}(HT)_{18}$ and $Au_{144}(HT)_{60}$, both of which are well-studied with respect to their electrochemical and optical properties.[2,8–11] In addition to their scientific interest, their synthesis is also well-reported.[12]

Figure 1.1 shows the structure of $Au_{144}(HT)_{60}$, which consists of a core of 12 Au atoms, surrounded by a shell of 42 Au atoms, and an additional outer shell of 60 Au atoms, which forms the surface layer. The capping layer comprises 30 RS-Au-SR staple motifs, where SR denotes a thiolate ligand, with R representing the organic chain of the thiol (in this case, hexanethiol).[11,13,14]

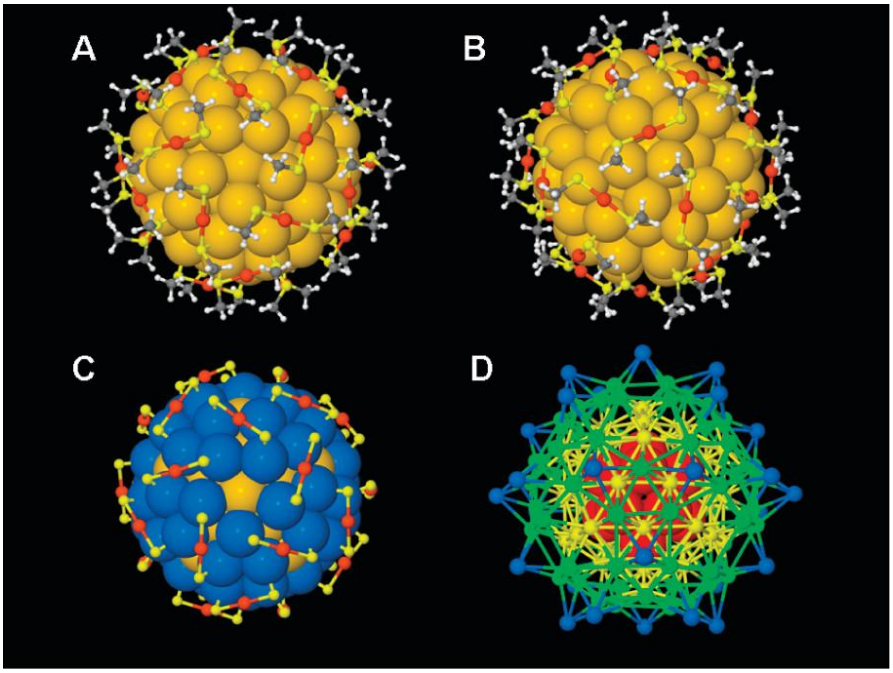

Figure 1.1 (A), (B) The relaxed structure of an $Au_{144}(SR)_{60}$ nanoparticle, viewed down a 5-fold and 3-fold symmetry axis (A, B respectively). (C) The arrangement of the RS–Au–SR staple units covering the surface layer (blue) of the Au_{114} core. (D) all the 144 gold atoms, with different atom shells denoted by different colours.

Key: yellow, Au in the Au_{114} core; orange, Au in the RS–Au–SR unit; bright yellow, S; grey, C; white, H. Adapted with permission, *J. Phys. Chem. C 2009, 113, 13, 5035-5038*.

The $Au_{25}(HT)_{18}$ structure is shown in Figure 1.2, and is composed of a 13-atom core surrounded by a single shell of 12 Au atoms. Each exterior Au pair (six pairs of outer Au atoms) is bridged by -SR ligands, with two additional -SR ligands bridging between the surface atoms and the internal core to form the ligand shell. The staple motif in $Au_{25}(HT)_{18}$ is dimeric in nature, taking the form of RS-Au-(SR)-Au-SR.[15,16]

Much of the work on nanoparticle stability focuses on their structure or the properties of the ligand shell, with comparatively less attention given to the influence of the substrate material and its reactivity on nanoparticle integrity.[2]

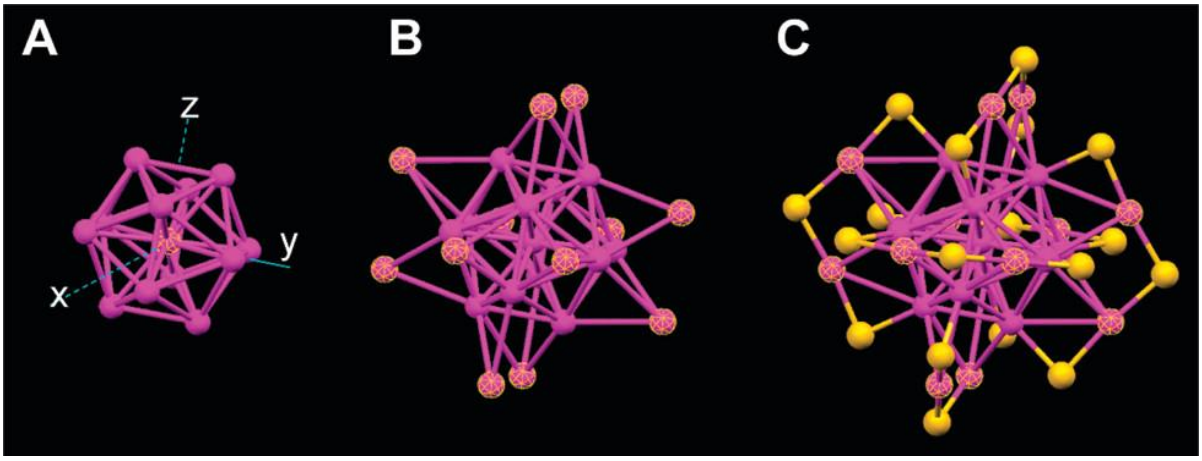

Figure 1.2 The structure of a $Au_{25}(SR)_{18}$ nanoparticle (R is phenylethyl group): (A) The 13 atom icosahedral core; (B) the Au_{13} core plus the 12 exterior Au atoms; (C) the whole Au_{25} cluster protected by 18 thiolate ligands in an extended staple structure. Key: magenta, Au; yellow, S. Adapted with permission, *J. Am. Chem. Soc. 2008, 130, 18, 5883-5885*.

We now discuss the studies by Pensa et al. on the Au NP-Au substrate system and their findings regarding the influence of the substrate on Au NP stability.

1.1.2 Observed Instability of Au NPs on Au (111)

Work by Pensa et al. aimed to investigate the stability of Au NPs when immobilised onto an Au (111) substrate.[17] The primary objective was to study the structural evolution of the NPs upon immobilisation, and examine the effect of substrate reactivity on their stability, using high-resolution in situ scanning tunnelling microscopy (STM).

In-air STM imaging of the Au (111) surface modified with Au144(HT)60 particles revealed that, instead of discrete particles, round islands with a height of approximately 0.24 nm, or multiples of this value were observed (Figure 1.3 a, b). These heights indicated the presence of monolayers or multiple layers of Au. Periodic patterns were also detected on and around the islands, corresponding to thiols in a 'lying down' (LD) configuration (Figure 1.3 I, II). This same formation of Au islands surrounded by thiol domains, this time in a

standing up (SU) c-(4x2) lattice or disordered, was observed when Au25(HT)18 was deposited on the Au substrate (Figure 1.3 III, IV), demonstrating that the decomposition process was not dependent on the size of the NPs.

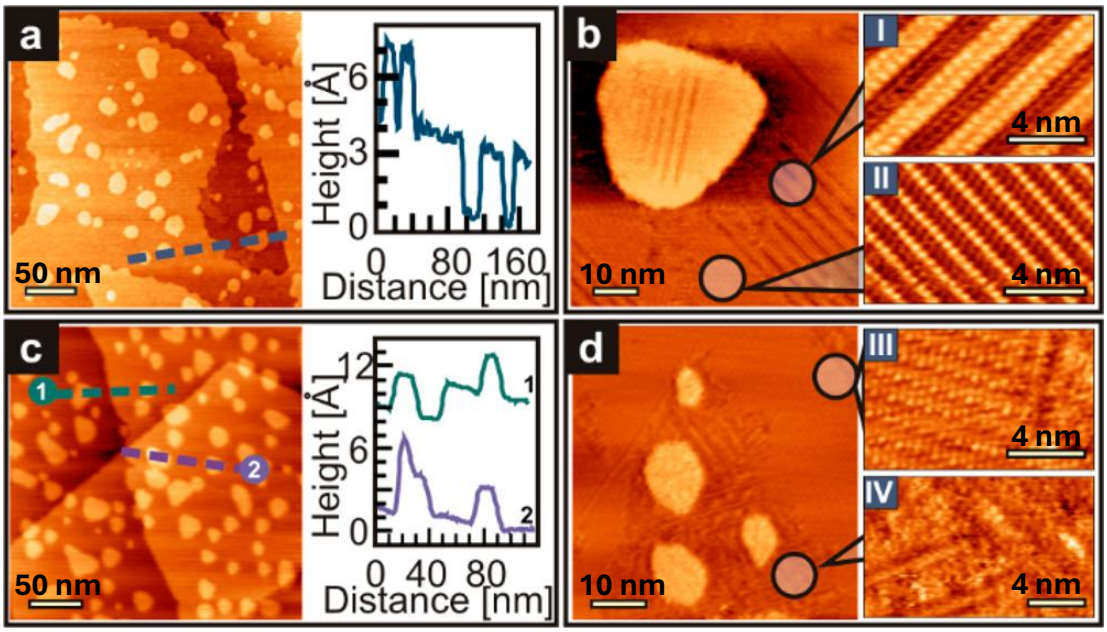

Figure 1.3 In air STM images of an Au (111) substrate after immersion in a dispersion of (a, b) $Au_{144}(HT)_{60}$ and (c, d) $Au_{25}(HT)_{18}$. Thiol domains surrounding Au islands were observed in different arrangements: (i) LD head-to-head, (ii) LD head-to-tail, (iii) in a *c*-(4×2) lattice structure, and (iv) in a disordered configuration. *Adapted with permission, J. Phys. Chem. Lett. 2018, 9, 1, 57-62.*

The S-Au bond is not rigid, with evidence suggesting its mobility on both flat Au substrates and Au nanoparticles or clusters.[18] It was proposed that the thiol binding to the Au substrate and Au particle surface was likely similar, facilitating the migration of thiol units onto the Au (111) surface. The process was proposed to be driven by the entropic favourability due to a large number of available binding sites on the substrate in comparison to the nanoparticle surface. Following thiol redistribution, the reactive Au core becomes exposed, triggering the decomposition and restructuring of the nanoparticle into Au islands on the substrate surface.

To investigate whether the reactivity of the substrate affected this process, Au (111) was passivated using two different molecules: strongly with a thiol solution and weakly with mesitylene (1,3,5-trimethylbenzene). The thiol passivation was carried out using an ethanolic solution containing a 9:1 ratio of 1-hexanethiol (HT) to 1,16-hexadecanedithiol (HDDT). When Au_{144} NPs were deposited onto the strongly passivated substrate, STM imaging revealed bright spots with heights of approximately 3.2 nm, which closely matched the diameter of the intact NPs, indicating that the nanoparticles retained their structural integrity upon immobilisation. This outcome was a result of the removal of the entropic driving force for thiol redistribution, with the kinetically stabilised NPs maintaining their structure for a time exceeding the 12-hour timescale of the imaging experiment.

In the system where Au (111) was less strongly passivated with mesitylene, STM imaging still showed the NPs as bright spots. However, even in the initial images, the height of the Au features was approximately half the diameter of a single Au NP, indicating that decomposition had already begun. Complete degradation into monoatomic Au islands occurred within approximately 24 minutes.

To summarise, the decomposition process was fastest on bare Au (111) substrates. On weakly passivated Au (111) with mesitylene, decomposition was slower, as thiol migration from the Au NP to the Au (111) substrate required a vacant binding site, which depended on mesitylene desorption into the solution. The process was further slowed on Au (111) substrates passivated with thiols. It was clearly demonstrated that the reactivity of the substrate surface therefore plays a significant role in the stability of the nanoparticles.

1.1.3 Mechanisms for the Decomposition of Au NPs

The processes underlying the disintegration of Au nanoparticles on the Au (111) substrate, along with the driving factors, have been explored in detail and are outlined in this section.

1.1.3.1 Decomposition of Au25(HT)18 Nanoparticles on Au (111)

As observed in Figure 1.3 d (iii, iv), the thiol domains surrounding decomposed $Au_{25}(HT)_{18}$ nanoparticles are arranged in two distinct configurations: (iii) a c-(4×2) lattice structure and (iv) a disordered configuration. These arrangements are shown more clearly in Figure 1.4.[19] Notably, no pitting was observed on the Au substrate, which is typically associated with the formation of self-assembled monolayers (SAMs).[18,20,21]

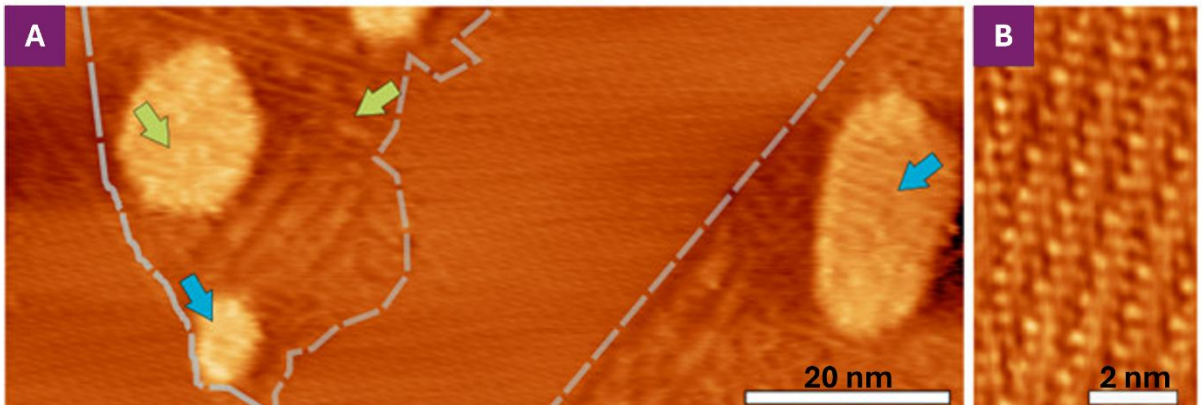

Figure 1.4 In-air STM images of an Au (111) substrate after immersion in a dispersion of $Au_{25}(HT)_{18}$. (A) Two distinct thiol domains are observed: outside the grey dashed line, thiols are in a disordered configuration, also present on the Au islands themselves (blue arrow); inside the dashed line, thiols are arranged in a *c*(4×2) lattice structure, shown in high resolution in (B). Green arrows indicate areas of agglomeration. *Adapted with permission, J. Phys. Chem. C 2020, 124, 9, 5452-5459.*

This indicates that the Au adatoms required for the formation of the thiol lattice were not provided by the Au substrate, but rather originated from the Au nanoparticles.

Pensa et al. observed that, over time, there was no continuous adsorption and decomposition of additional Au nanoparticles. Instead, the sizes of the thiol domains and Au islands progressively increased. This increase in thiol coverage likely reduced the reactivity of the substrate, thereby slowing down the degradation process of the Au nanoparticles.[22]

It was also noted that the thiol moieties on the Au (111) substrate were arranged as RS-Au-SR (monomeric) structures. In contrast, on the Au25 NP surface, the thiol moieties were arranged in the dimeric configuration RS-Au-(SR)-Au-SR. Density functional theory (DFT) calculations were used to determine the binding energies (BE) and surface free energies (SFE) associated with sulfur bonding in each configuration; sulfur in the dimeric unit on the NP surface, in the dimeric unit on the Au (111) substrate, and in the monomeric unit on the Au (111) substrate.

The data revealed that sulfur was most strongly bound in the monomeric unit on Au (111), followed by the dimeric unit on Au (111), and least strongly bound in the dimeric structure on Au_{25}. Despite the disintegration of the Au NP being a thermodynamically favourable process, the thermodynamic stability determined by the SFE showed that the dimeric structure on the Au_{25} NP surface was the most stable.

Table 1.1 Binding energy (BE) and surface free energy (SFE) data for RS in three surface structures. Data from Pensa et al.: Table 1, *J. Phys. Chem. C 2020, 124, 9, 5452-5459*.

Unit Structure	BE (eV)	SFE (meV Å^{-2})
$Au_{25}(SR)_{18}$	-2.96	-166.91
RS-Au-(SR)-Au-SR on Au (111)	-3.23	-148.04
RS-Au-SR on Au (111)	-3.47	-158.96

The energetics at each stage of the decomposition process were subsequently calculated, leading to the proposal of the following mechanism for the adsorption, disintegration, and decomposition of the $Au_{25}(HT)_{18}$ nanoparticle on an Au (111) substrate.

The adsorption of the Au nanoparticle onto the Au (111) substrate initiates the migration of dimeric thiol units from the NP surface to the substrate, exposing the core Au atoms. The dimeric staple structure then breaks down into monomeric staples, which subsequently decompose into RS-Au, RS, and Au adatoms, as has been evidenced at room temperature.[23,24] Au adatoms released from the NP core then react with RS species to form RS-Au units, which in turn form monomeric staple units and Au adatoms as their surface coverage increases, forming the ordered c-(4x2) lattice structure. Au atoms from the NP core and Au adatoms released upon the disintegration of the dimeric staple then form Au islands.

In addition to the mechanism of decomposition, the factors triggering this process were determined. Entropically, decomposition is favoured. However, when the thermodynamics and energetics of the process were examined, the situation proved more complex, involving a balance between the stability of the thiol capping layer on the Au NP surface and the core cohesive energy. While thiols are more thermodynamically stable on the NP surface than on the substrate, decomposition becomes energetically favourable due to the formation of Au islands from Au adatoms in the gas phase, released as a result of the core's instability once exposed. The balance between these opposing factors is disrupted when the Au NPs adsorb onto the Au (111) substrate, triggering thiol migration and the subsequent decomposition of the NP core.

1.1.3.2 Decomposition of Au144(HT)60 Nanoparticles on Au (111)

STM imaging demonstrated that $Au_{144}(HT)_{60}$ immobilised on Au (111) resulted in the formation of monoatomic Au islands and SR units on the substrate, arranged in two domains: head-to-head and head-to-tail, both in an LD (lying down) configuration.[25] The LD structures were shown to consist of RS-Au-SR units incorporating Au adatoms, with these adatoms partially supplied by the NP cores themselves, as observed with Au_{25}.[19] Consequently, etch pits were not observed in this case either, consistent with the results for Au_{25} NPs.

DFT calculations were performed to understand the energetics of RS species on the Au_{144} surface and the Au (111) surface. Binding energies (BE) and surface free energies (SFE) were calculated for each structure—head-to-head (H-H) and head-to-tail (H-T)—on Au (111), as well as for RS species on the Au_{144} surface. As with the Au_{25} energetics, while the thiol is more strongly bound to the Au (111) surface in both LD configurations, it is most thermodynamically stable on the NP surface. Therefore, for both NP sizes, decomposition cannot be attributed solely to the intrinsic instability of the nanoparticles themselves.

Table 1.2 Binding energy (BE) and surface free energy (SFE) data for RS in three surface structures. Data from Pensa *et al.*: Table 1, *Chem. Mater. 2021, 33, 9, 3428-3435*.

Unit Structure	BE (eV)	SFE (meV Å^{-2})	LD Config.
RS-Au-SR on Au (111)	-3.68	-63.22	H-H
RS-Au-SR on Au (111)	-3.73	-64.08	H-T
$Au_{144}(SR)_{60}$	-2.85	-192.85	

It should be noted that the products of ligand migration from Au_{25} resulted in a higher surface coverage of thiols in the SU (standing up) configuration, whereas for Au_{144}, an LD

configuration was observed, indicating lower surface coverage under the same experimental conditions. The lower number of decomposed Au_{144} NPs was attributed to their higher core cohesive energy compared to Au_{25}, as well as the greater stability conferred by their thiol capping layer. Specifically, Au_{144} features 30 staple structures contributing to its stabilisation, compared to only 6 on Au_{25} (see 1.1.1 Structure of Some Thiolated Au Nanoparticles).[13–16]

It was found that the Au islands formed upon the decomposition of Au_{144} were primarily located at the step edges of the Au (111) substrate, whereas for Au_{25}, the features were distributed across both step edges and terraces. This suggests a preferential decomposition of Au_{144} NPs at the more reactive (low coordinated) step edges, consistent with Au_{144} being less reactive than the smaller Au_{25}.[26–28]

The following decomposition mechanism was proposed for Au_{144}: at the more reactive step edges, RS-Au-SR staples break down into RS-Au and RS radicals, which interact with low-coordinated Au atoms at the step edges. The migration and opening of the capping layer expose the Au core, which subsequently decomposes into Au islands. The RS-Au components and Au adatoms combine to form RS-Au-SR units. Since this process is limited to step edges and the Au core has a high cohesive energy, the resulting RS-Au-SR coverage is low. This explains why thiol units on the substrate are observed in an LD configuration rather than a higher-coverage SU configuration.

1.2 Beyond the Au-Au System

The instability of $Au_{144}(HT)_{60}$ and $Au_{25}(HT)_{18}$ nanoparticles on an Au (111) substrate, along with the energetics and decomposition mechanisms that explain the resultant substrate structure, have been explored in detail. The findings revealed that both entropic and enthalpic factors play a role, providing valuable insights into key aspects of the surface stability of metal nanoparticles.

Returning to the effect of substrate reactivity, it is evident that it significantly influences the integrity of nanoparticles. This raises the question of what occurs when the energetics of the system are altered and whether this can be exploited to create new nanomaterials or nanostructured features on surfaces, as demonstrated by the controlled growth of Au islands on Au (111).[29] Would the appropriate choice of core metal, substrate material, and capping chemistry enable well-defined surface modification and functionalisation with one or more additional metallic species? For instance, in a study by Hosseini *et al.*, a thiolated Au nanoparticle underwent ligand place exchange to incorporate 4-(4'-pyridyl)thiophenols into its capping layer. When deposited onto a Pt (111) substrate, the modified capping layer acted as a rigid linker between the particle and substrate, preventing the Au core from directly contacting the Pt surface. As a result, no signs of disintegration were observed for up to three days.[30,31]

While more changes were made than simply altering the substrate material, this highlights an important point: changing the substrate material onto which Au nanoparticles are deposited to a different metal alters the energetics of the system, particularly the metal-thiol bond, and may consequently affect the stability of the

nanoparticles. While the entropic driving force may still drive the thiol redistribution process, the different metal-thiol binding energies may counteract this effect.

A study was conducted on $Au_{144}(HT)_{60}$ nanoparticles immobilised onto a polycrystalline Pt electrode, as well as the reverse system of Pt nanoparticles – protected with 1-hexanethiol – deposited onto a polycrystalline Au electrode.[32] Cyclic voltammetry performed on each modified surface revealed that, for Au NPs on Pt, there was a suppression of current density associated with Pt activity features but no Au-specific voltammetric features were observed. This finding was consistent across both alkaline media and in the presence of glycerol. These results suggested that the Au NPs remained intact on the Pt substrate but were not electrochemically active, which aligned with the authors expectations, as the Au-thiol bond is stronger than the Pt-thiol bond.[33,34] Consequently, there was no significant enthalpic driving force for thiol migration and formation of Pt-thiol bonds at the expense of Au-thiol bonds.

The opposite behaviour was observed for the reverse system, in which Pt nanoparticles were deposited onto an Au substrate. Cyclic voltammetry showed a suppression in the current density of Au-specific voltammetric features and the emergence of Pt-specific features. This indicated the presence of exposed, electrochemically active Pt on the Au substrate. This study highlighted the importance of both entropic and enthalpic driving forces in the process. While the redistribution of thiols is entropically favoured due to the larger number of available binding sites on the substrate, the enthalpy associated with metal-thiol bond breaking and formation must also be taken into account.

The study demonstrated that Pt islands on an Au substrate exhibited electrochemical behaviour identical to that of bulk Pt, as observed through cyclic voltammetry. This

finding is crucial when considering the exploitation of thiolated NP instability for designing functional substrates. Careful consideration must be given to whether the resultant metal features—whether intact nanoparticles or those with some degree of decomposition—retain the same properties as their bulk counterparts or whether interactions between metal species give rise to new properties and characteristics. This, along with evaluating the stability of thiolated metal nanoparticles on substrates composed of materials different from the nanoparticle core, forms the central focus of this thesis.

1.2.1 Mixed Metal Systems

In this thesis, Pt and Ag are incorporated into the experimental matrix. While the literature reports interactions among Au, Pt, and Ag in both bulk and nanoscale systems, relatively little attention has been given to systems where one metal is at the nanoscale and the other is in bulk form. This section will briefly review the different metal interactions that may arise, focusing on metal-metal interactions as well as the variations in metal-thiol binding. These considerations will inform the expectations for the mixed nanoparticle-metal substrate experiments presented in this work.

1.2.1.1 Comparative Metal - Thiol Bond Strengths

The relative strengths of Au–S, Pt–S, and Ag–S bonds have been quantified both in terms of gas-phase bond dissociation energies (BDEs) and adsorption energies of thiolates on single-crystal surfaces (Table 1.3).

Table 1.3 Reported values for metal–sulfur bond strengths (gas-phase bond dissociation energies and thiolate adsorption energies on (111) surfaces). [a] Values reported by Petrovykh *et. al.*[34], [b] Cristina *et. al.*[35], [c] Karhánek *et. al.*[36], [d] Cometto *et. al.*[37]

Metal-Sulfur Bond	Gas-phase BDE (kJ mol^{-1})	Thiolate adsorption energy (kJ mol^{-1})	Notes
Au-S	418 [a]	145-174 [b] ($C_6H_{13}S$ on Au(111) SAMs)	Stable intact SAMs
Pt-S	234 [a]	≥193 [c] (CH_3S on Pt(111), dissociated fragments)	Intact SAMs are unstable; thiol dehydrogenates and fragments
Ag-S	217 [a]	106–138 [d] (CH_3S on Ag(111), DFT)	No data for 1-hexanethiol; shorter-chain data used

The gas-phase BDE values place Au–S at 418 kJ·mol^{-1}, significantly stronger than Pt–S (~234 kJ·mol^{-1}) and Ag–S (217 kJ·mol^{-1}). Adsorption energies provide a more surface-specific measure but show greater variability. For Au(111), values for 1-hexanethiol and related alkanethiolates fall in the range 145–174 kJ·mol^{-1}, consistent with the stability of ordered self-assembled monolayers. Ag(111) exhibits weaker adsorption, with reported energies of 106–125 kJ·mol^{-1} for short-chain thiolates such as CH_3S. On Pt(111), reported adsorption energies for CH_3S are comparatively high (≥193 kJ·mol^{-1}), but these correspond to dissociated species, as intact alkanethiol SAMs are unstable and decompose through dehydrogenation and C–S bond cleavage.

Taken together, these data support the overall ordering Au–S > Pt–S > Ag–S when considering intact thiol binding. However, because direct adsorption energies for 1-hexanethiol are not consistently available across all three metals, the gas-phase BDE

values provide the most reliable basis for comparison in this work. This distinction is important in the context of nanoparticle–substrate interactions.

1.2.1.2 Au and Pt

For Au nanoparticles on a Pt substrate, the entropic driving force is expected to favour the migration of thiols from the Au NP surface to the Pt substrate. Counteracting this effect is the fact that the Au-thiol bond is stronger than the Pt-thiol bond.[34] Reports suggest that the latter factor dominates, as Au nanoparticles have been shown to remain intact upon immobilisation onto Pt supports.[31,32] A similar entropic factor applies for Pt nanoparticles on an Au substrate. However, the scenario reverses in terms of enthalpic considerations, as the formation of more favourable Au-thiol bonds would be expected to drive the thiol redistribution process in this case.

It has been shown that Pt nanoparticles, upon thiol redistribution exposing the Pt core, exhibit electrochemical activity identical to that of bulk Pt. The interaction between Pt and Au varies depending on the scale. At the bulk level, Pt and Au exhibit a miscibility gap, with the two metals expected to segregate into Pt-rich and Au-rich phases.[38–40] At the nanoscale, alloy nanoparticles have been synthesised across various size ranges; however, the degree of alloying and phase segregation is influenced by multiple factors, including preparation conditions, particle size, and the local environment, such as the support substrate.[41,42] Au is often reported to phase-segregate on top of Pt, resulting in core-shell nanoparticles, with Au typically surrounding a Pt core.[43,44] This behaviour is attributed to the lower surface energy and larger atomic size of Au compared to Pt.[40,45]

1.2.1.3 Ag and Pt

For a system of Ag NPs on a Pt substrate, and conversely Pt NPs on an Ag substrate, the entropic factor is expected to drive the thiol migration process in both cases. However, the Ag-S bond is weaker than the Pt-S bond, which suggests that for Ag NPs on a Pt substrate, thiol redistribution might be favoured both entropically and enthalpically, with the thiols preferentially binding to the larger Pt substrate.[34]

The interaction between Ag and Pt metals at the bulk scale exhibits a greater miscibility gap than that between Au and Pt, although silver enrichment is expected.[40] At the nanoscale, alloy nanoparticles of various metal compositions have been synthesised across the miscibility gap, but their stability is influenced by factors such as particle size and the metal ratio.[46,47] Furthermore, the alloying of Ag and Pt is often facilitated by methods such as laser irradiation, high-temperature annealing, or controlled chemical deposition.[48–50] Given these conditions, it remains unclear whether enrichment, phase segregation, alloy formation, or even independent behaviour of the metals would result from the interaction of Ag and Pt metals as a result of thiol redistribution.

1.2.1.4 Au and Ag

As with the other systems discussed, whether involving Ag NPs on Au or Au NPs on Ag, the entropic argument remains in favour of a thiol redistribution process. However, the relative strengths of the Au-S and Ag-S bonds influence the enthalpic contributions. With the Au-S bond being stronger than the Ag-S bond, Au NPs on an Ag substrate are likely to experience enthalpic hindrance to the migration of thiols from the Au surface to the Ag substrate. In contrast, for Ag NPs on an Au substrate, the difference in thiol binding energies may drive the redistribution process, exposing Ag features on the Au substrate.[34]

In terms of their interaction, Ag and Au are completely miscible at the bulk scale, readily forming alloys.[51,52] Additionally, Ag has been shown to segregate at the surface in both bulk systems and in bimetallic alloy nanoparticles composed of the two metals.[53,54]

1.2.1.5 Important Considerations

It is evident from these discussions that the miscibility of metals changes as the size regime transitions from bulk to nanoscale. At the nanoscale, the surface area-to-volume ratio is significantly higher, resulting in more of the metal being exposed to its surroundings. Additionally, a greater proportion of atoms are located at the edges and corners of nanoparticles compared to a bulk surface. These atoms exhibit lower coordination numbers, leading to increased reactivity, and contributing to the changes in miscibility observed in some metal systems.[51,55]

This discussion has covered expectations regarding metal-thiol binding energy differences and explored some key metal-metal interactions. Within the context of this thesis, it is crucial to note that the systems investigated do not exist solely at the bulk or nanoscale. Instead, they involve one material at the bulk scale and another at the nanoscale, making it unclear how the interactions between the materials will be influenced by the difference in size regimes.

1.2.2 Objectives of the Study

This discussion has highlighted how interactions differ as the size regime transitions from bulk to nanoscale. Building on this, we aim to explore the substrate modifications in the following mixed-metal systems: Au NPs on Ag and Pt substrates, Pt NPs on Au and Ag substrates, and Ag NPs on Pt and Au substrates.

It is important to bear in mind that the 'enthalpic' factors and the energetics of NP decomposition processes are complex, as discussed in 1.1.3 Mechanisms for the Decomposition of Au NPs. In this work, a more generalised perspective on the NP disintegration process is adopted, focusing on preferential thiol binding due to variations in metal-thiol bond strengths. This approach aims to provide initial insights and rationalise the properties of the modified substrate surfaces observed following NP immobilisation.

The objectives are to explore whether thiol redistribution occurs, determine if the NP core remains stable upon exposure or undergoes decomposition (and to what extent), and assess whether the resulting metal feature is electrochemically active. If electrochemical activity is observed, it is crucial to evaluate whether it mirrors the behaviour of the bulk counterpart or differs, and to understand the reasons behind this difference. Addressing these points is essential for the informed design of new electrochemical surfaces.

1.3 Overview of Experimental Techniques

This section provides an overview of the experimental techniques employed in this thesis, outlining their principles and relevance to the study. These methods were selected to offer insights into the structural and electrochemical changes in thiolated metal nanoparticles upon their immobilisation on different substrates.

1.3.1 Synthesis of Nanoparticles via Cathodic Corrosion

There are numerous methods for the synthesis of metal nanoparticles, each with their advantages and limitations. These methods can be classified into two categories: top-down and bottom-up approaches.

Top-down approaches involve breaking down bulk materials or solids into nanoparticles. Techniques such as ball milling, lithography and sputtering are used to mechanically decrease the size of a starting material.[2,56] Top-down approaches can be straightforward, in the sense that the methods are generally simpler versus those involving multi-step chemical reactions and are also easier to employ for the bulk production of nanoparticles. However, they often lead to a wide distribution in particle size and may potentially damage the crystal structure of the particles, as well as other contaminations of the particle surface.[3]

Bottom-up approaches involve the assembly of atoms or molecules into nanoparticles through chemical reactions, and generally afford good control over the structure and morphology of the resultant nanoparticles.[3,4] These approaches include chemical reduction, where a metal salt is reduced to metal atoms via reaction with a reducing agent in the presence of a stabilising agent; sol-gel processes and biological synthesis, among others.[57]

Cathodic corrosion is a process by which a metal wire, submerged in a conductive electrolyte solution, is converted into an aqueous suspension of metal nanoparticles.[58] The process has been demonstrated to produce a variety of catalytically active monometallic, metal oxide and alloy nanoparticles, depending on the material chosen as the working electrode.[59–61] As it is a one-step process that takes place in the absence

of organic reagents such as reducing agents or stabilisers, and requires little manual intervention during the synthesis, it can be a more desirable pathway as compared to multi-step synthesis techniques. Further, the size, shape and composition of the nanoparticles produced can be tuned by varying the applied square wave parameters electrochemical conditions.[60,62–64]

The system comprises a working electrode (WE), a metal wire composed of the target material, and a counter electrode (CE) that is a high surface area metal flag. The WE and CE are submerged in an aqueous conductive electrolyte, and an alternating current (AC) square wave-form is applied, and an offset also applied to ensure the WE is held under a cathodic condition.[58] As a result, hydrogen gas evolution at the WE surface leads to the formation of a water-free layer, while the oxygen evolution reaction takes place at the CE. The metal wire undergoes reduction into its anionic form, and this intermediate species is stabilised by adsorption of cations from the electrolyte.[61] The intermediate detaches from the surface of the WE as a result of the switching of the applied potential and encounters free water molecules beyond the depletion-layer, as well as other reactive oxygen species produced at the CE.[62] Reaction of the intermediate with these species and water oxidises the intermediate into its metallic state, which possesses a high surface energy and subsequently coalesces to form nanoparticles that are suspended in the electrolyte.[58,65]

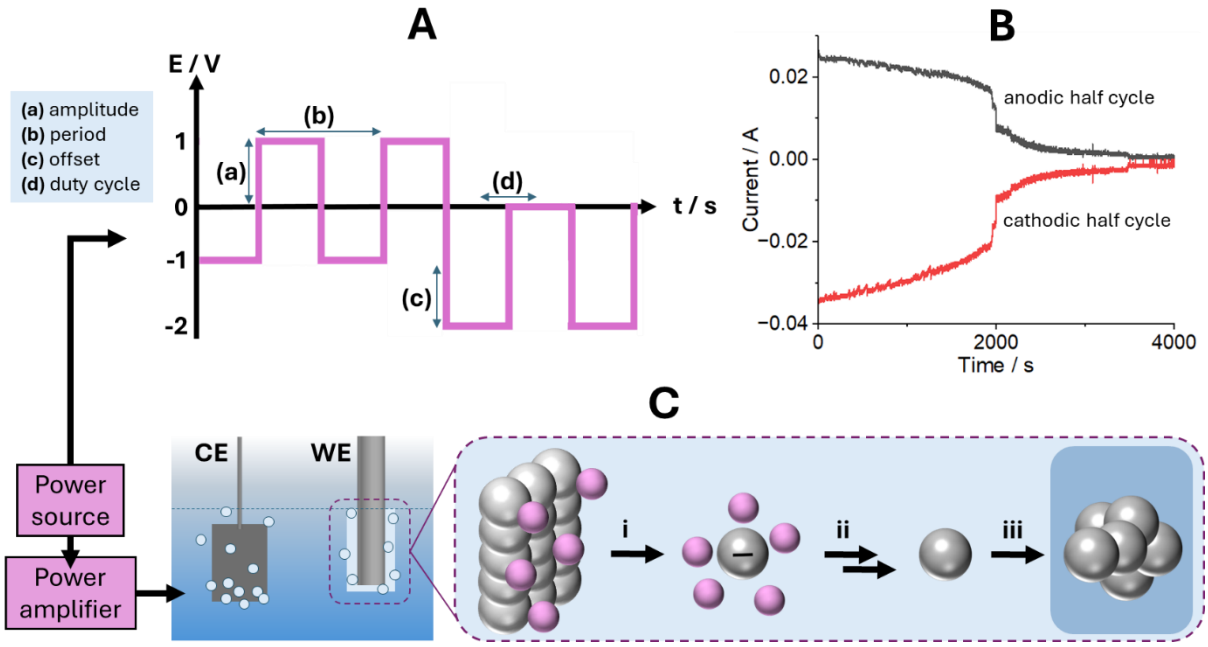

Figure 1.5 (A) Illustration of the AC potential square wave form applied across the electrodes, including the effect of an applied offset. Features of the square wave are labelled. (B) Example of the AC current measured during the cathodic corrosion of a Pt wire. (C) Illustration of the 2-electrode setup for cathodic corrosion. An AC square wave form is generated via a power source (power supply, potentiostat) and the potential difference applied across the working (WE) and counter (CE) electrodes. Oxygen gas evolution at the CE results in observable effervescence, hydrogen gas evolution at the WE results in a high pH, water free layer at the metal interface, where the metal is reduced into its anionic form, stabilised by cations in the depletion layer (i) the metal anionic species detaches due to switching of the wave-form, (ii) oxidises into its metallic state upon encountering water and reactive oxygen species beyond the depletion layer and (iii) agglomerates to form nanoparticles.

Though 3-electrode configurations have also been used for cathodic corrosion,[66] this research project employed only the 2-electrode system, with the setup as illustrated in Figure 1.6 (A).[59] The WE was attached with both a coarse and micrometric screw, and was first lowered to the surface of the electrolyte using the coarse screw, and then immersed by the desired amount via the micrometric screw.

The parameters used to define the square waveform applied are amplitude, offset, frequency and duty cycle (Figure 1.5 (A)). The parameter values vary depending on the

nanoparticle material to be synthesised. Typically, a lower amplitude results in smaller nanoparticles being formed, while the offset potential is generally the same value as the amplitude to ensure a negative AC potential is applied throughout the synthesis.[65] The frequency value used in this work was generally 100 Hz, and the duty cycle 50%. The duty cycle represents percentage of time the signal is at the maxima of the square wave per wavelength *e.g.* a duty cycle of 50% indicates an equal ratio of time at the maxima and minima of the wave form.

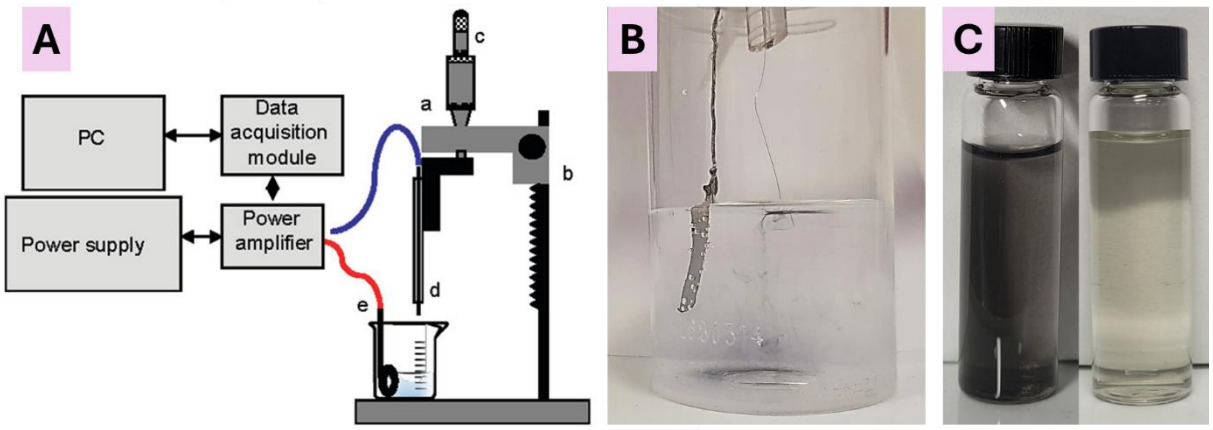

Figure 1.6 (A) Illustration of the experimental setup of cathodic corrosion synthesis. (a) A support, attached to (b) a coarse screw and (c) a micrometric screw, (d) WE wire and (e) CE. (B) Picture taken during the synthesis of Pt nanoparticles. (C) *Left* Pt and *right* Ag nanoparticles synthesised using cathodic corrosion. A - Adapted with permission, *J. Am. Chem. Soc. 2011, 133, 44, 17626–17629. Copyright 2011 American Chemical Society.*

The completion of the cathodic corrosion process is indicated via monitoring of the current-time trace, which should display the anodic and cathodic half cycles each decreasing towards a current of zero (Figure 1.5 (B)), or by visual inspection of the amount of wire in solution. The latter is not the optimal way to monitor the process, however, as the solution may be too opaque to clearly see the WE wire, as well as instances of wire

passivation leaving wire in solution without further cathodic corrosion activity taking place, in which case parameters must be re-evaluated and adjusted.

In this thesis, cathodic corrosion was employed to synthesise Pt and Ag nanoparticles, making an understanding of this process essential.

1.3.2 Electrochemical Characterisation of Modified Substrates

Electrochemistry, a branch of physical chemistry, examines the relationship between chemical changes and the flow of electrons. Measurements are typically performed at the interface between a solid electronic conductor (the electrode) and a liquid ionic conductor (the electrolyte).[67] While electrochemical studies can also focus on solid/solid or liquid/liquid interfaces, this work is centred on solid/liquid interfaces.

1.3.2.1 Working principles of Electrochemistry

The working principle of electrochemistry is based on the charge transfer that occurs between the electrode and the electrolyte when an external power source applies a potential difference across the system. The driving force behind these charge transfer processes is the energy of the electrons in the electrode of interest, known as the working electrode (WE). Applying an increasingly negative (cathodic) potential to the WE raises the energy of the vacant electrons above the lowest unoccupied molecular orbital (LUMO) of the species in solution, resulting in electron transfer from the electrode to the electrolyte species. This process generates a reduction current. Conversely, applying a positive (anodic) potential to the WE causes charge transfer from the species in solution to the electrode, leading to the flow of oxidation current. These processes are represented in Figure 1.7 (reproduced from reference[67]).

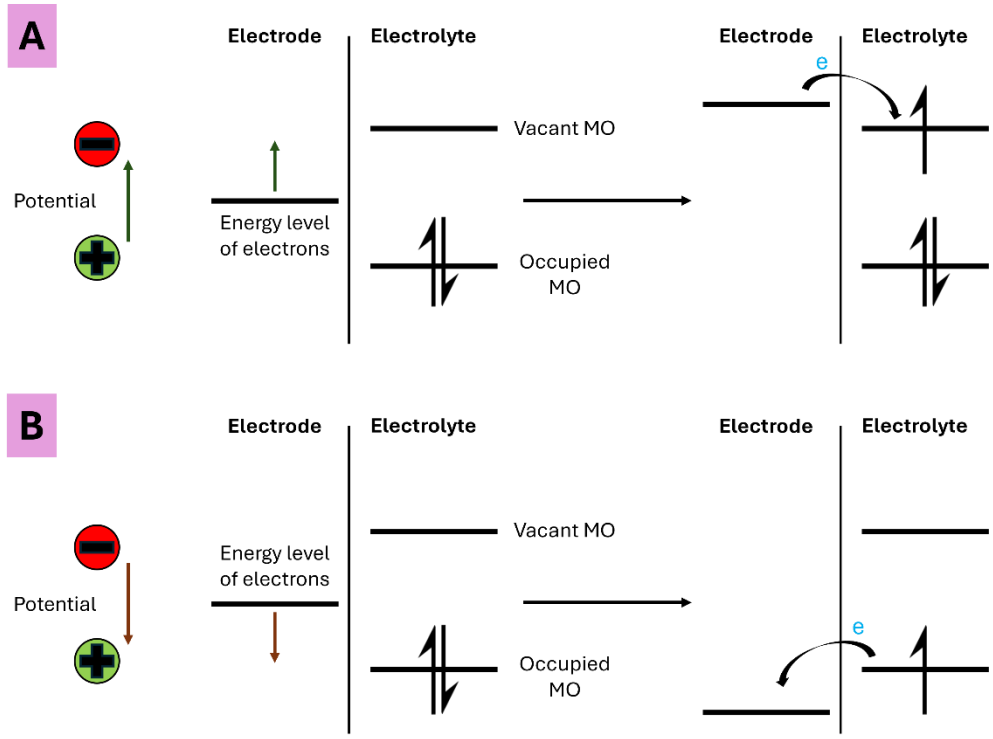

Figure 1.7 Illustration of the (A) reduction and (B) oxidation processes on an electrolyte species. *Reproduced with permission, Copyright © 2000, John Wiley and Sons.*

Charge transfer reactions are typically studied using a three-electrode system, which consists of a WE, a reference electrode (RE), and a counter electrode (CE). In voltammetry, a potentiostat applies a varying potential difference between the WE and the RE across a defined range, referred to as the potential window, to the WE. This potential is standardised using the RE, and the resulting current is measured.[68]

At the CE, often a large surface area electrode such as a Au flag, a complementary reaction that balances the charge transfer occurring at the WE takes place. The high surface area of the CE ensures that the reaction taking place there does not become a limiting factor for the reaction or the measurement at the WE.

When the WE is in contact with the electrolyte but no external current is drawn and no electrochemical processes are externally driven, the system reaches an open circuit

potential (OCP). At this potential, the system is in thermodynamic equilibrium. For a given redox couple, the OCP represents the potential at which the rates of oxidation and reduction are balanced.

1.3.2.2 Faradaic and non-faradaic processes

Two types of processes can occur at an electrode: faradaic and non-faradaic. Faradaic processes involve charge transfer and are governed by Faraday's law, which states that the amount of chemical reaction caused by the flow of current is proportional to the amount of electricity passed.

Within an applied potential window, there exists a double-layer region where no charge transfer reactions occur. In this region, non-faradaic process may occur, for example the adsorption or desorption of electrolyte species from the electrode surface. While these processes are not always the primary focus of study, it is important to note that faradaic and non-faradaic processes occur in parallel.[67]

For faradaic processes involving charge transfer, the reduced species must be transported to the electrode surface, where electron transfer and oxidation reactions take place.

1.3.2.3 Mass transport

Mass transport of species in an electrochemical system occurs through three processes: migration, convection, and diffusion. Migration refers to the movement of charged electrolyte species under the influence of an electric field. Convection involves the movement of species due to mechanical forces. This can be natural, arising from density gradients within the bulk solution, or forced, as in the case of stirring the solution.

Mass transport via diffusion refers to the movement of species from areas of high concentration to areas of low concentration. When a potential is applied to the working electrode (WE) such that, for example, oxidation of a redox species occurs, the reduced species is consumed near the electrode interface. This consumption creates a concentration gradient, inducing a flux of molecules from the bulk solution to the electrode. This effect is described by Fick's laws of diffusion. Fick's first law is expressed as:

$$J = -\mathrm{D}\frac{\mathrm{d}c}{\mathrm{d}x} \tag{1}$$

where J is the flux, D is the diffusion coefficient, c is the concentration, x is the position, and dc/dx is the concentration gradient. Fick's first law is an expression that the flux of electrolyte species is proportional to the concentration gradient.

Fick's second law describes time-dependent diffusion process, where the concentration gradient evolves over time. It is expressed as:

$$\frac{dc}{dt} = \mathrm{D}\left(\frac{\mathrm{d}^2c}{\mathrm{d}x^2}\right) \tag{2}$$

While all three mass transport processes are typically present in a system, the effects of convection and migration can be minimised through careful experimental design.

1.3.2.4 Cyclic voltammetry

Cyclic voltammetry involves sweeping the potential at the working electrode (WE) between two setpoints at a fixed scan rate while recording the resulting current.[67,68] When a redox couple is present, sweeping the potential anodically induces the faradaic process of oxidation, which is observed as oxidation peaks in the voltammetric features.

Consider a simple one-electron transfer reaction, such as the oxidation of ferrocene (Fc) to ferrocenium (Fc^+):

$$Fc \rightleftharpoons Fc^+ + e^-$$

As the applied potential increases, the Fc molecules near the electrode surface are oxidised, depleting their concentration and forming a diffusion layer. This creates a concentration gradient between the electrode surface and the bulk solution, driving the diffusion of Fc molecules toward the electrode.

The electrode potential is related to the concentrations of the oxidised and reduced species through the Nernst equation:

$$E = E^0 + \frac{RT}{nF} \ln \frac{a_{\mathrm{Ox}}}{a_{\mathrm{Red}}} \tag{3}$$

where E is the electrode potential, E^0 is the standard electrode potential, a is the activity of Ox or Red (related to concentration via $a_A = \gamma_A[A]/[1\ \mathrm{mol\ dm^{-3}}]$ where γ is the activity coefficient), R is the universal gas constant, T is the temperature, n is the number of electrons transferred, and F is Faraday's constant. For the example system of ferrocene (Fc), this equation becomes equation 4, where $E^{0\prime}$ is the formal potential:

$$E = E^{0\prime} + \frac{RT}{F} \ln \frac{[\mathrm{Fc}^+]}{[\mathrm{Fc}]} \tag{4}$$

The initial change in potential to more positive values, and the subsequent oxidation of Fc, generates an output current that is recorded. As the potential continues to become more positive, the diffusion layer expands, and the oxidation process becomes limited by mass transport. This results in a gradual decrease in the measured current until the potential reaches the switching potential. During this process, the concentration of the

reduced species [Fc] decreases, while the concentration of the oxidised species [Fc^+] increases, maintaining the balance described by the Nernst equation.

When the switching potential is reached, the cathodic sweep begins. As the applied potential becomes more negative, Fc^+ is reduced back to Fc, producing a reduction peak. For a chemically and thermodynamically reversible one-electron reaction, the peak-to-peak separation between the oxidation and reduction peaks is 59 mV, which arises from the diffusion of the analyte to and from the electrode. In electrochemically irreversible reactions, sluggish electron transfer kinetics result in a larger peak-to-peak separation.

1.3.2.5 Effect of electrode geometry

The faradaic current measured depends on the diffusion behaviour of the species, and is influenced by the geometry of the WE. Macroelectrodes, typically with a diameter ≥100 µm, exhibit linear diffusion, where the diffusion layer develops in a single direction perpendicular to the electrode surface. In this case, electrochemical processes are more affected by mass-transport limitations.

In contrast, microelectrodes, generally with a diameter up to 25 µm, exhibit hemispherical diffusion. Here, the diffusion layer is curved, allowing species to approach the electrode from multiple directions. As a result, electrochemical processes at microelectrodes are less affected by mass-transport limitations and exhibit smaller capacitive currents. Due to their increased sensitivity and reduced susceptibility to mass-transport limitations, microelectrodes were used in the work presented in this thesis.

Cyclic voltammetry was used to evaluate the electrochemical activity of nanoparticle-modified substrates, with changes in the voltammetric profiles serving as confirmation of exposed NP cores if they were electrochemically active. An understanding of cyclic voltammetry is therefore crucial to interpreting the subsequent work.

1.3.3 Transmission Electron Microscopy (TEM)

Transmission electron microscopy (TEM) is an imaging technique often employed to study the size and morphology of materials, including nanoparticle samples.[69] Samples are deposited onto a TEM grid, typically copper-carbon though other materials are widely available. Upon sample insertion into the instrument, the system is under vacuum, to prevent the scattering of electrons by gas molecules and to preserve the integrity of the electron beam. A beam of electrons is accelerated by an electron gun and directed onto a specimen, where the electrons may either be absorbed, scattered, or pass through the sample. The sample must be sufficiently electron-transparent, with a thickness below 100 nm, to allow the transmission of electrons.[70]

Transmitted electrons are focused to form a two-dimensional image, where the image contrast is directly correlated with the sample's density. Regions where the sample is more dense result in less electrons transmitted through the sample, resulting in those areas appearing darker on the image. Conversely, regions of lower density correspond to lighter areas in the image.[69,70]

TEM was used in this work to characterise the Au, Ag and Pt nanoparticles and determine their average diameter.

1.3.4 Scanning Tunnelling Microscopy (STM)

STM of a conductive surface can reveal information such as its electronic properties and surface topography. The technique operates on the principle of quantum tunnelling across a nanoscale gap between an atomically sharp conductive tip and a substrate.[71] Tips are freshly prepared via chemically etching a wire, typically W or a Pt-Ir alloy, to an atomic point.[72] A piece of wire is cut and immersed into an etching solution as a working electrode, with a platinum counter electrode surrounding the tip to ensure uniform etching during the process. Once etched, the tip is removed from the setup and its sharpness and quality (*i.e.* bending, contamination) is evaluated visually. This may also be gauged through microscopy and imaging techniques, or simply through the resultant STM image quality. The tip is then mounted into a scanner, which is used to control the height and position of the tip during an experiment.

When the tip and sample are within a fraction of a nanometre of each other, electron wavefunctions in both the tip and substrate surface overlap, and the application of a bias voltage between the two results in a tunnelling current being generated.[73] This tunnelling current is sensitive to the tip-sample distance, and in combination with tip position can used to create a topographical map of the substrate surface (for conducting samples). This is achieved by operating the STM in a constant-current mode.

In constant-current mode, a setpoint current is defined in the operating software. The tunnelling current is measured and converted into a voltage by an amplifier. A feedback system controls the height of the tip by comparing the tunnelling current and setpoint value, producing a signal that is applied to the piezoelectric scanner (more specifically, the z-piezoelectric driver) to move the tip closer or further from the surface, maintaining

the tunnelling current. The voltage that is applied to the z-piezo driver is recorded as a function of the position of the tip (x, y axis), producing a topographical map of the surface.[74] Lighter areas on a topographical image represent a higher z-value, *i.e.* the tip has been moved away from the surface, and vice versa.[73]

In this thesis, some nanoparticle-modified substrates are characterised using STM imaging. The heights and diameters of the nanoparticle features allowed us to determine the degree of decomposition of particles, upon their immobilisation.

1.3.5 X-ray Photoelectron Spectroscopy (XPS)

XPS is a surface sensitive analytical technique that can provide information including the composition of a surface and the chemical state of its components. The principle on which this method is established is the photoelectric effect.[75]

A surface of interest is bombarded with soft x-rays under an ultra-high vacuum (UHV) environment. This is to prevent collisions of the x-rays with gas molecules before they can reach the analyte surface, to prevent the ejected electrons from being scattered before reaching the detector and to prevent surface contamination during the measurement process.[76] The energy of an x-ray (hv) may be transferred to a core electron, and if this value is sufficient to overcome its binding energy this results in its excitement and the ejection of a photoelectron from the surface.[77]

The relationship between these values is expressed as follows, where BE is the binding energy of an electron to its orbital of origin, hv is the energy of the x-ray, KE is the kinetic energy of the emitted photoelectron, and ϕ is the work function of the electron spectrometer:

$$BE = hv - KE - \phi \quad (5)$$

The terms $h\nu$ and ϕ will have known values, dependent upon instrumentation, while the value for KE is measured during the course of an XPS measurement, thereby allowing binding energies to be determined.[76]

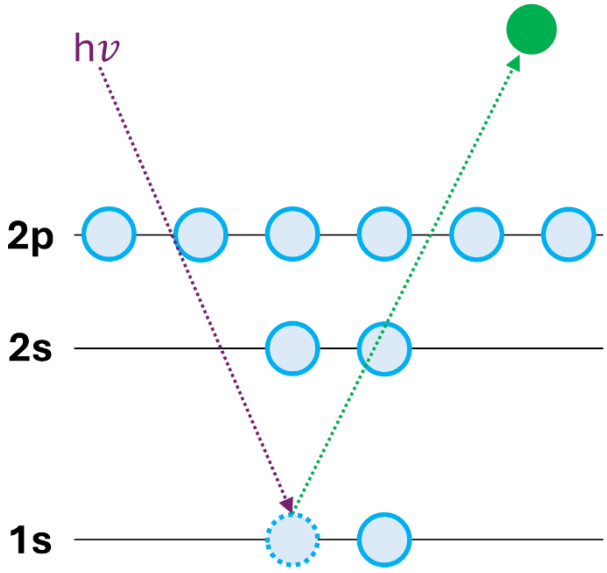

Figure 1.7 Schematic of the process of the emission of a photoelectron, as part of the XPS process.

Electrons emitted without energy loss contribute to the spectrum peaks produced by XPS, while those electrons that undergo inelastic scattering (i.e. collisions causing the loss of energy) instead contribute to the background region of the spectrum.[77] After initial survey scans, spectra can be obtained in binding energy ranges of interest and the peaks fitted, providing details of the chemical bonding of surface features as both the peak shapes and binding energies are characteristic to the chemical and oxidation state of the atom from which the electron was emitted.[4,75]

The XPS analysis of some modified substrates was done to determine if a thiol redistribution effect had taken place upon nanoparticle immobilisation, by evaluating the metal-thiol binding energies and assessing where the thiols were preferentially bound.

1.4 References

1 T. Kawawaki and Y. Negishi, *Nanomaterials* , 2020, **10**, 238.

2 A. Mathew and T. Pradeep, *Particle & Particle Systems Characterization*, 2014, **31**, 1017–1053.

3 M. Sajid and J. Płotka-Wasylka, *Microchemical Journal*, 2020, **154**, 104623.

4 R. Ferrando, J. Jellinek and R. L. Johnston, *Chem Rev*, 2008, **108**, 845–910.

5 B. Kumar, T. Kawawaki, N. Shimizu, Y. Imai, D. Suzuki, S. Hossain, L. V Nair and Y. Negishi, *Nanoscale*, 2020, **12**, 9969–9979.

6 E. Dieterich, S.-J. Kinkelin, M. Steimecke and M. Bron, *Nanoscale Adv*, 2022, **4**, 5154–5163.

7 L. Prati and A. Villa, *Acc Chem Res*, 2014, **47**, 855–863.

8 S. Antonello, N. V Perera, M. Ruzzi, J. A. Gascón and F. Maran, *J Am Chem Soc*, 2013, **135**, 15585–15594.

9 K. Hirata, K. Yamashita, S. Muramatsu, S. Takano, K. Ohshimo, T. Azuma, R. Nakanishi, T. Nagata, S. Yamazoe, K. Koyasu and T. Tsukuda, *Nanoscale*, 2017, **9**, 13409–13412.

10 T. Ohta, M. Shibuta, H. Tsunoyama, Y. Negishi, T. Eguchi and A. Nakajima, *The Journal of Physical Chemistry C*, 2013, **117**, 3674–3679.

11 K. M. Ø. Jensen, P. Juhas, M. A. Tofanelli, C. L. Heinecke, G. Vaughan, C. J. Ackerson and S. J. L. Billinge, *Nat Commun*, 2016, **7**, 11859.

12 R. Jin, C. Zeng, M. Zhou and Y. Chen, *Chem Rev*, 2016, **116**, 10346–10413.

13 O. Lopez-Acevedo, J. Akola, R. L. Whetten, H. Grönbeck and H. Häkkinen, *The Journal of Physical Chemistry C*, 2009, **113**, 5035–5038.

14 H. Qian and R. Jin, *Nano Lett*, 2009, **9**, 4083–4087.

15 M. Zhu, C. M. Aikens, F. J. Hollander, G. C. Schatz and R. Jin, *J Am Chem Soc*, 2008, **130**, 5883–5885.

16 J. Akola, M. Walter, R. L. Whetten, H. Häkkinen and H. Grönbeck, *J Am Chem Soc*, 2008, **130**, 3756–3757.

17 E. Pensa and T. Albrecht, *J Phys Chem Lett*, 2018, **9**, 57–62.

18 T. Bürgi, *Nanoscale*, 2015, **7**, 15553–15567.

19 P. Carro, E. Pensa, T. Albrecht and R. C. Salvarezza, *The Journal of Physical Chemistry C*, 2020, **124**, 5452–5459.

20 Y. Wang, Q. Chi, N. S. Hush, J. R. Reimers, J. Zhang and J. Ulstrup, *The Journal of Physical Chemistry C*, 2011, **115**, 10630–10639.

21 P. M. Spurgeon, D.-J. Liu, T. L. Windus, J. W. Evans and P. A. Thiel, *ChemPhysChem*, 2021, **22**, 349–358.

22 C. Vericat, G. A. Benitez, M. E. Vela, R. C. Salvarezza, N. G. Tognalli and A. Fainstein, *Langmuir*, 2007, **23**, 1152–1159.

23 J. Gao, H. Lin, X. Qin, X. Zhang, H. Ding, Y. Wang, M. Rokni Fard, D. Kaya, G. Zhu, Q. Li, Y. Li, M. Pan and Q. Guo, *J Phys Chem B*, 2018, **122**, 6666–6672.

24 S. Holmes, R. E. Palmer and Q. Guo, *The Journal of Physical Chemistry C*, 2019, **123**, 24104–24110.

25 P. Carro, L. M. Azofra, T. Albrecht, R. C. Salvarezza and E. Pensa, *Chemistry of Materials*, 2021, **33**, 3428–3435.

26 C. García, S. Pollitt, M. van der Linden, V. Truttmann, C. Rameshan, R. Rameshan, E. Pittenauer, G. Allmaier, P. Kregsamer, M. Stöger-Pollach, N. Barrabés and G. Rupprechter, *Catal Today*, 2019, **336**, 174–185.

27 Z. Wu, Y. Jin, L. Xu, Q. Yuan, F. Xiong, Z. Jiang and W. Huang, *The Journal of Physical Chemistry C*, 2014, **118**, 8397–8405.

28 R. Gaspari, C. A. Pignedoli, R. Fasel, M. Treier and D. Passerone, *Phys Rev B*, 2010, **82**, 41408.

29 H. Cao, D. Waghray, S. Knoppe, W. Dehaen, T. Verbiest and S. De Feyter, *Nat Commun*, 2018, **9**, 4889.

30 N. Bodappa, U. Fluch, Y. Fu, M. Mayor, P. Moreno-García, H. Siegenthaler and T. Wandlowski, *Nanoscale*, 2014, **6**, 15117–15126.

31 S. Hosseini, N. Alsiraey, A. J. Riley, T. Zubkov, T. Closson, J. Tye, N. Bodappa and Z. Li, *Langmuir*, 2018, **34**, 15517–15525.

32 N. Awais, P. Rodriguez and T. Albrecht, *ECS Trans*, 2020, **97**, 885.

33 M. A. Floridia Addato, A. A. Rubert, G. A. Benítez, M. H. Fonticelli, J. Carrasco, P. Carro and R. C. Salvarezza, *The Journal of Physical Chemistry C*, 2011, **115**, 17788–17798.

34 D. Y. Petrovykh, H. Kimura-Suda, A. Opdahl, L. J. Richter, M. J. Tarlov and L. J. Whitman, *Langmuir*, 2006, **22**, 2578–2587.

35 L. J. Cristina, G. Ruano, R. Salvarezza and J. Ferrón, *The Journal of Physical Chemistry C*, 2017, **121**, 27894–27904.

36 D. Karhánek, T. Bučko and J. Hafner, *Journal of Physics: Condensed Matter*, 2010, **22**, 265005.

37 F. P. Cometto, P. Paredes-Olivera, V. A. Macagno and E. M. Patrito, *J Phys Chem B*, 2005, **109**, 21737–21748.

38 O. Malis, M. Radu, D. Mott, B. Wanjala, J. Luo and C.-J. Zhong, *Nanotechnology*, 2009, **20**, 245708.

39 G. Bond, C. Louis and D. Thompson, *College Press: Joplin, MO, USA*, 2006, preprint.

40 V. Ponec and G. C. Bond, *Catalysis by metals and alloys*, Elsevier, 1995, vol. 95.

41 B. N. Wanjala, J. Luo, B. Fang, D. Mott and C.-J. Zhong, *J Mater Chem*, 2011, **21**, 4012–4020.

42 L. Deng, W. Hu, H. Deng and S. Xiao, *The Journal of Physical Chemistry C*, 2010, **114**, 11026–11032.

43 Y. Ma and P. B. Balbuena, *Surf Sci*, 2008, **602**, 107–113.

44 S. Xiao, W. Hu, W. Luo, Y. Wu, X. Li and H. Deng, *The European Physical Journal B - Condensed Matter and Complex Systems*, 2006, **54**, 479–484.

45 M. Chatzidakis, S. Prabhudev, P. Saidi, C. N. Chiang, J. J. Hoyt and G. A. Botton, *ACS Nano*, 2017, **11**, 10984–10991.

46 Z. Peng and H. Yang, *J Solid State Chem*, 2008, **181**, 1546–1551.

47 J. Wisniewska, H. Guesmi, M. Ziolek and F. Tielens, *J Alloys Compd*, 2019, **770**, 934–941.

48 K. Mariandry, R. Kokate, S. V Somerville, L. Gloag, S. Cheong, L. R. Carroll, P. V Kumar, J. J. Gooding and R. D. Tilley, *Chemistry of Materials*, 2023, **35**, 8636–8644.

49 T. Hu, Y. Fan, Y. Ye, Y. Cai, J. Liu, Y. Ma, P. Li and C. Liang, *Catalysts*, 2023, **13**, 1018.

50 K. A. Kane, A. C. Reber, S. N. Khanna and M. F. Bertino, *Progress in Natural Science: Materials International*, 2018, **28**, 456–463.

51 G. Guisbiers, R. Mendoza-Cruz, L. Bazán-Díaz, J. J. Velázquez-Salazar, R. Mendoza-Perez, J. A. Robledo-Torres, J.-L. Rodriguez-Lopez, J. M. Montejano-Carrizales, R. L. Whetten and M. José-Yacamán, *ACS Nano*, 2016, **10**, 188–198.

52 J.-M. Song, W.-T. Chen, K.-H. Hsieh, T.-H. Kao, I.-G. Chen, S.-J. Chiu and H.-Y. Lee, *Nanoscale Res Lett*, 2014, **9**, 438.

53 V. Grasmik, C. Rurainsky, K. Loza, M. V Evers, O. Prymak, M. Heggen, K. Tschulik and M. Epple, *Chemistry – A European Journal*, 2018, **24**, 9051–9060.

54 A. G. Garcia, P. P. Lopes, J. F. Gomes, C. Pires, E. B. Ferreira, R. G. M. Lucena, L. H. S. Gasparotto and G. Tremiliosi-Filho, *New Journal of Chemistry*, 2014, **38**, 2865–2873.

55 E. Roduner, *Chem Soc Rev*, 2006, **35**, 583–592.

56 P. F. M. de Oliveira, R. M. Torresi, F. Emmerling and P. H. C. Camargo, *J Mater Chem A Mater*, 2020, **8**, 16114–16141.

57 S. Kumari, S. Raturi, S. Kulshrestha, K. Chauhan, S. Dhingra, K. András, K. Thu, R. Khargotra and T. Singh, *Journal of Materials Research and Technology*, 2023, **27**, 1739–1763.

58 A. I. Yanson, P. Rodriguez, N. Garcia-Araez, R. V Mom, F. D. Tichelaar and M. T. M. Koper, *Angewandte Chemie International Edition*, 2011, **50**, 6346–6350.

59 P. Rodriguez, F. D. Tichelaar, M. T. M. Koper and A. I. Yanson, *J Am Chem Soc*, 2011, **133**, 17626–17629.

60 Yu. I. Yanson and A. I. Yanson, *Low Temperature Physics*, 2013, **39**, 304–311.

61 M. L. Kromer, J. Monzó, M. J. Lawrence, A. Kolodziej, Z. T. Gossage, B. H. Simpson, S. Morandi, A. Yanson, J. Rodríguez-López and P. Rodríguez, *Langmuir*, 2017, **33**, 13295–13302.

62 A. I. Yanson, P. V Antonov, P. Rodriguez and M. T. M. Koper, *Electrochim Acta*, 2013, **112**, 913–918.

63 E. Bennett, J. Monzó, J. Humphrey, D. Plana, M. Walker, C. McConville, D. Fermin, A. Yanson and P. Rodriguez, *ACS Catal*, 2016, **6**, 1533–1539.

64 M. J. Lawrence, A. Kolodziej and P. Rodriguez, *Curr Opin Electrochem*, 2018, **10**, 7–15.

65 A. I. Yanson, P. V Antonov, Y. I. Yanson and M. T. M. Koper, *Electrochim Acta*, 2013, **110**, 796–800.

66 T. J. P. Hersbach, I. T. McCrum, D. Anastasiadou, R. Wever, F. Calle-Vallejo and M. T. M. Koper, *ACS Appl Mater Interfaces*, 2018, **10**, 39363–39379.

67 A. J. Bard, L. R. Faulkner and H. S. White, *Electrochemical Methods: Fundamentals and Applications*, Wiley, 3rd edn., 2003.

68 N. Elgrishi, K. J. Rountree, B. D. McCarthy, E. S. Rountree, T. T. Eisenhart and J. L. Dempsey, *J Chem Educ*, 2018, **95**, 197–206.

69 Z. L. Wang, *J Phys Chem B*, 2000, **104**, 1153–1175.

70 G. Huebschen, I. Altpeter, R. Tschuncky and H. G. Herrmann, *Materials Characterization Using Nondestructive Evaluation (NDE) Methods*, Woodhead Publishing, 2016.

71 D. M. Mattox, in *Handbook of Physical Vapor Deposition (PVD) Processing (Second Edition)*, ed. D. M. Mattox, William Andrew Publishing, Boston, 2010, pp. 25–72.

72 W. A. Hofer, A. S. Foster and A. L. Shluger, *Rev Mod Phys*, 2003, **75**, 1287–1331.

73 C. J. Chen, *Introduction to Scanning Tunneling Microscopy*, Oxford University Press, 2nd edn., 2007.

74 H. Siegenthaler, R. Wiesendanger and H. J. Guntherodt, *by R. Wiesendanger and HJ GUntherodt (Springer, Berlin, 1992) p*.

75 H. L. Lee and N. T. Flynn, *Handbook of Applied Solid State Spectroscopy*, Springer, New York, 1st edn., 2006.

76 F. A. Stevie and C. L. Donley, *Journal of Vacuum Science & Technology A*, 2020, **38**, 063204.

77 J. F. Watts and J. Wolstenholme, *An Introduction to Surface Analysis by XPS and AES*, John Wiley & Sons, 2nd edn., 2003.

2. Materials and Methods

Chapter Contents

This chapter outlines the experimental procedures for all experiments performed and reported in this thesis. It includes detailed protocols for glassware cleaning, the synthesis of nanoparticles used for surface modifications, the preparation (cleaning and modification) of metal substrates, and the methodologies for the experimental techniques of TEM, STM, XPS, and cyclic voltammetry.

2.1 Glassware Cleaning Procedure

All glassware used in the experimental work was cleaned using a standardised protocol to ensure the removal of organic and inorganic contaminants. The glassware was first immersed overnight in an acidified permanganate solution ($KMnO_4$). It was then removed from the solution and thoroughly rinsed with ultrapure water (MilliQ®, resistivity 18.2 MΩ cm, TOC ≤ 5 ppb). This was followed by rinsing with approximately 50 mL of a diluted 1:3 mixture of hydrogen peroxide (35%, Baker) and sulfuric acid (96%, Merck). The mixture was prepared by mixing 1 mL of sulfuric acid and 3 mL of hydrogen peroxide into 300 mL of ultrapure water and then diluting the mixture to a final volume of 1 L (caution advised—can cause explosion). Finally, the glassware was rinsed three times with boiling ultrapure water.

2.2 Synthesis of Nanoparticles

Au, Ag, and Pt nanoparticles were synthesised using two distinct protocols. Au nanoparticles were synthesised using a modified Brust-Schiffrin method[1], while Ag and Pt nanoparticles were prepared via the cathodic corrosion method.

2.2.1 Synthesis of Au Nanoparticles via the Brust-Schiffrin Method

$Au_{144}(HT)_{60}$ nanoparticles were synthesised following an established protocol, adapted from Qian *et. al*.[2–4] The reagents used were gold (III) chloride trihydrate ($HAuCl_4 \cdot 3H_2O$, ≥99.9%, Sigma), tetraoctylammonium bromide (ToABr, ≥99%, Sigma), methanol (99.9%, Sigma), 1-hexanethiol (HT, 95%, Sigma), sodium borohydride ($NaBH_4$, 99%, Sigma), dichloromethane (DCM, ≥99.9%, Sigma), and acetone (99%, VWR).

For the synthesis, 236 mg of $HAuCl_4 \cdot 3H_2O$ and 380 mg of ToABr were dissolved in 30 mL of methanol under vigorous stirring. Subsequently, 0.476 mL of HT was added to the solution with continuous stirring. To this mixture, 6 mL of freshly prepared 0.5 M $NaBH_4$ was added, leading to the formation of a black precipitate, indicating the successful synthesis of Au nanoparticles.

The precipitate was collected by centrifugation at 3500 rpm for 5 minutes. It was then washed with an excess of methanol and centrifuged again. This washing step was repeated at least ten times to ensure the complete removal of free thiol residues.

Following the cleaning process, smaller Au_{25} clusters were selectively removed using acetone. The desired Au_{144} clusters were subsequently extracted, dispersed in DCM, and stored for use in surface modification experiments.

2.2.2 Synthesis of Nanoparticles via Cathodic Corrosion

Two different setups were employed for nanoparticle synthesis by cathodic corrosion. *Setup A* consisted of LabVIEW software connected to a power supply and power amplifier, with the current-time trace recorded through a National Instruments DAQ module (NI-6211).[5] *Setup B* used a GAMRY Reference 600 potentiostat, with waveform

parameters controlled and the current-time trace monitored via the Virtual Front Panel software. The synthesis parameters for nanoparticles of various materials are reported in Table 2.1 and Table 2.2, where CE refers to the counter electrode, a high surface area Pt flag for all experiments listed.

Table 2.4 Parameters for the cathodic corrosion of various materials using *Setup A*.

Setup A								
Material	**Electrolyte**	**Amp. (V)**	**Offset (V)**	**Freq. (Hz)**	**CE**	**Product Formed ?**	**Characterisation**	**Observations**
Pt	0.5 M NaOH	±1.25	-1.25	100	Pt	Y	CV	Grey/black suspension of particles. Currents and etch time consistent across synthesis cycles (etch times of approx. 30 mins).
$Pt_{80}Rh_{20}$	1 M NaOH	±5	-5	100	Pt	Y	CV	Grey suspension of particles.
Rh	10 M NaOH	±5	-5	500	Pt	Y	CV	Long etch times, > 1 hr on average.
Pd	50% $CaCl_2$	±5	-3	100	Pt	Y	CV	Black suspension of particles.
Ag	1 M $NaNO_3$	±5	-5	100	Pt	Y	CV	
Au	10 M NaOH	±10	-10	100	Pt	Y	CV	Grey/black suspension obtained in over 1 hour. Product agglomerated during centrifugation and did not disperse as a result of ultrasonic treatment.
$Au_{60}Pd_{40}$	10 M NaOH	±10	-10	100	Pt	Y	CV	Vigorous bubbling at working electrode, grey/black suspension obtained in over 1 hr.
$Pt_{90}Ni_{10}$	0.3 M NaOH	±1.25	-1.25	100	Pt	Y	CV	Grey suspension of particles.
Ti	10 M NaOH	±3.33	-3.33	1000	Pt	Y		White suspension of particles. Product falls out of suspension.

Ni	1 M KOH	±5	-5	100	Pt	Y		Blue suspension of particles obtained.

Table 2.5 Table reporting the parameters for the cathodic corrosion of various materials using *Setup B*.

Setup B								
Material	**Electrolyte**	**Amp. (V)**	**Offset (V)**	**Freq. (Hz)**	**CE**	**Product Formed ?**	**Characterisation**	**Observations**
Pt	0.5 M NaOH	±1.25	-1.25	100	Pt	Y		Some product formation, black particles localised to WE wire. Measured currents and etch times inconsistent between cycles. Etch times vary between order of seconds to 10s of minutes.
Pt	0.5 M NaOH	±1.5	-1.5	100	Pt	Y		Grey/black suspension of particles. Etch times inconsistent and decrease with subsequent synthesis cycles.
Pt*	0.5 M NaOH	±2	-2	100	Pt	Y	TEM, UV-vis	Grey/black suspension of particles. Etch times consistently approx. 7 mins.
Pt	0.5 M NaOH	±2.25	-2.25	100	Pt	Y		First synthesis cycle gave an etch time of approx. 2min, but the wire was not fully atomised. In cycle two, the remainder of wire was mostly dissolved. Third cycle attempted to dissolve the remainder of wire, but no particle formation observed. Across cycles 2 and 3, particles were slow to form, and currents do not seem to decrease with time.
Pt	0.5 M NaOH	±2.5	-2.5	100	Pt	Y		Etch times of approx. 3 mins. Some wire remains in solution, not fully atomised.
Pt*	0.5 M NaOH	±3	-3	100	Pt	Y	TEM, UV-vis	Grey/black suspension of particles. Very quick, varying

								etch times, some in the order of minutes (1.5 mins).
Ag	0.1 M $NaNO_3$	±3	-3	10	Pt	N		No activity or particle formation observed for > 2 hrs.
Ag*	0.1 M $NaNO_3$	±5	-5	10	Pt	Y	TEM, UV-vis	Some effervescence at the Ag wire, observed a green/silver suspension after approx. 1 hr.
Ag	0.1 M $NaNO_3$	±5	-5	100	Pt	N		No activity or particle formation observed for >2 hrs.
Ag*	0.1 M $NaNO_3$	±5.5	-5.5	10	Pt	Y	TEM	Etch time of 1 mm of Ag wire > 5 hrs.
Ag	0.1 M $NaNO_3$	±5.5	-5.5	100	Pt	N		No activity or particle formation observed for >2 hrs.
Ag	0.1 M $NaNO_3$	±6	-6	10	Pt	N		No activity or particle formation observed for >2 hrs.
Ni	1 M KOH	±2	-2	100	Pt	N		No activity or particle formation observed for >1hr.
Ni	1 M KOH	±3	-3	100	Pt	N		Some bubbling seen at the Ni wire for ~10 sec, no further observations after this. No colour change > 1hr.
Ni	1 M KOH	±5	-5	100	Pt	Y		Vigorous effervescence at Ni wire, brown suspension of particles.
Ni	1 M KOH	±6	-6	100	Pt	N		No activity or particle formation observed for >1hr.

The Pt and Ag nanoparticles used in this thesis were synthesised using Setup B and are marked with an asterisk (*) in Table 2.2, with further details of the synthesis provided below.

2.2.2.1 Synthesis of Pt Nanoparticles

For the synthesis of Pt nanoparticles, 20 mL of 0.5 M sodium hydroxide (NaOH, 99.99%, Alfa Aesar) was prepared and placed in the reaction vessel. A Pt wire (99.95%, Alfa Aesar) was used as the working electrode and immersed 2 mm into the solution during each synthesis cycle. A Pt flag counter electrode was flame-annealed, quenched with ultrapure water (MilliQ®, 18.2 MΩ), and then immersed into the solution.

The resulting nanoparticles were cleaned via centrifugation at 3500 rpm for 15 minutes, and the supernatant replaced with ultrapure water. This washing step was repeated at least five times to ensure the removal of residual NaOH. Following this, HT (95%, Sigma) was added in a 1:5 ratio of thiol to Pt, and the mixture was placed in an ultrasonic bath until the nanoparticles were well dispersed. The cleaning process via centrifugation was then repeated at least ten times to ensure the removal of excess thiol.

2.2.2.2 Synthesis of Ag Nanoparticles

For the synthesis of Ag nanoparticles, 20 mL of 0.1 M sodium nitrate ($NaNO_3$, ≥99.5%, Sigma) was prepared and placed in the reaction vessel. An Ag wire (99.9%, VWR) was used as the working electrode and immersed 2 mm into the solution during each synthesis cycle. A Pt flag counter electrode was flame-annealed, quenched in ultrapure water (MilliQ®, 18.2 MΩ) and then immersed in the solution.

As with the synthesis of Pt NPs, the resulting nanoparticles were cleaned via centrifugation at 3500 rpm for 25 minutes, repeated at least five times, before the addition of HT (95%, Sigma) in a 1:5 thiol-to-metal ratio. The mixture was placed in an ultrasonic bath until well dispersed, after which it underwent further cleaning by centrifugation, repeated at least ten times.

2.2.2.3 Further Details of Ag and Pt Synthesis

For the synthesis of both Au and Pt nanoparticles, the mass of metal wire corroded was determined by first calculating the volume of wire consumed. This was obtained using the equation for the volume of a cylinder:

$$V = \pi r^2 h$$

where r is the radius of the wire and h is the measured length corroded. The mass of metal was then calculated by multiplying the volume by the density of the corresponding metal (ρ_{Pt} = 21.45 g cm^{-3}; ρ_{Ag} = 10.50 g cm^{-3}).

The number of moles of metal was obtained by dividing the calculated mass by the molar mass of the metal (M_{Pt} = 195.08 g mol^{-1}; M_{Ag} = 107.87 g mol^{-1}). A fivefold molar excess of thiol relative to the calculated number of metal atoms was then added to ensure complete surface coverage of the nanoparticles, as with the synthesis of Au NPs. The number of moles of 1-hexanethiol required was therefore determined as:

$$n_{thiol} = 5 \times n_{metal}$$

The corresponding volume of 1-hexanethiol was calculated from its molar mass (118.24 g mol^{-1}) and density (ρ = 0.832 g cm^{-3}):

$$V_{thiol} = \frac{n_{thiol} \times M_{thiol}}{\rho_{thiol}}$$

Since different lengths of wire were consumed in different syntheses, this procedure was repeated for each experiment to determine the specific amount of thiol required in each case.

2.3 Preparation of Substrates

The preparation steps for Au, Pt, and Ag electrodes and substrates used in XPS, STM, and cyclic voltammetry experiments are detailed below. These steps include both the preparation and cleaning of the substrates, as well as the immobilisation of nanoparticle samples onto their surfaces.

2.3.1 Preparation of Au (111) substrates for STM Studies

For STM measurements, a Au (111) single crystal disc was used (99.999% purity, polished surface roughness of <0.01 µm, orientation accuracy of <0.1°, MaTeck). The preparation of the substrate began with cleaning via electropolishing. For this purpose, the disc underwent electro-oxidation in 0.5 M H_2SO_4 at 5 V, using an Au counter electrode, to generate a thick layer of Au oxide. The disc was then immersed in 1 M HCl to dissolve the oxide layer, followed by rinsing with ultrapure water (MilliQ®, 18.2 MΩ). This procedure was repeated three to five times. After cleaning, the substrate was furnace-annealed at 850 °C for 12 hours using a NaberTherm LE 4/11/R6 furnace. Finally, the substrate was flame-annealed using a hydrogen flame and cooled in a nitrogen environment.

2.3.2 Preparation of Au (111) and Pt (111) substrates for XPS

2.3.1.1 Au (111) substrate

An Au (111) substrate on glass support (Arrandee™, Germany) was used. The substrate was flame-annealed until lightly glowing, then removed from the flame and allowed to cool for 30 seconds. This procedure was repeated at least three times to ensure a clean and well-ordered surface.

2.3.1.2 Pt (111) substrate

A Pt (111) single crystal disc (99.999% purity, surface roughness <0.01 µm, and orientation accuracy <0.1°, MaTeck, Germany) was used. The disc was furnace-annealed at 850 °C for 4 hours using a furnace (NaberTherm LE 4/11/R6, Germany). Following this, the disc was flame-annealed in a hydrogen flame and allowed to cool in a nitrogen environment.

2.3.3 Preparation of Au, Pt and Ag Electrodes for Cyclic Voltammetry

For electrochemical measurements, polycrystalline gold and platinum microelectrodes (ø = 25 µm, ALS Ltd) and a polycrystalline Ag electrode (ø = 2 mm, IJ Cambria Scientific Ltd) were used. Prior to use, the electrodes were polished using a diamond paste (0.5 µm, Kemet) mixed with ultrapure water (MilliQ®, 18.2 MΩ) to form a slurry on a polishing cloth (Buehler, MetaDi, 0.5 µm). After polishing, electrodes were rinsed thoroughly with ultrapure water.

2.3.4 Modification of Metal Substrates with Nanoparticles

The Au, Ag, and Pt substrates were modified with nanoparticles using similar procedures. The nanoparticle samples were first dispersed via ultrasonication in an ultrasonic water bath (42,000 Hz, 5-10 mins). Following the substrate preparation steps detailed above, each substrate was immersed in the nanoparticle solution for approximately 12 hours, with the beaker covered and sealed. Next, the substrates were removed from the nanoparticle solution and rinsed thoroughly with ultrapure water (MilliQ®, 18.2 MΩ). For electrochemistry, the electrodes were used immediately after this rinsing step. For STM and XPS measurements, the substrates were dried under a nitrogen flow prior to use.

2.4 Transmission Electron Microscopy

For TEM imaging, nanoparticle samples were well-dispersed via ultrasonication in an ultrasonic water bath (42,000 Hz, 5-10 mins) and then drop-cast onto TEM grids (Formvar/Carbon Supported Copper Grids, 400 mesh, Sigma). Au nanoparticle imaging was performed using a Jeol 1400 TEM at the University of Birmingham, UK, while Pt and Ag nanoparticle imaging was carried out using a 2100 LaB6 TEM by Han Yisong at the University of Warwick, UK.

TEM image analysis was performed using Gwyddion and ImageJ softwares.[6,7] Particle diameters were measured in one direction where particles exhibited overlap. For particles without overlap, diameters were measured in two perpendicular directions as a cross-section and then averaged.

2.5 Scanning Tunnelling Microscopy

STM measurements were performed using an Agilent 5100 (Keysight Technologies) STM equipped with a linear scanner. The Au (111) single crystal substrate was prepared as previously detailed. During measurements, the substrate was held in place using a Teflon holder and accompanying cell parts, all of which were cleaned following the glassware cleaning procedure. STM images were analysed using Gwyddion software.[6] Particle diameters were calculated by averaging two perpendicular cross-sections, while the heights of the features were extracted from the corresponding height profiles.

2.5.1 Tip Preparation

The STM tips were prepared using tungsten wire (ø = 0.25 mm, 99.95%, H. Cross Co.). The tungsten wire was connected to the positive voltage output, with a platinum ring counter

electrode connected to the negative voltage output. The tungsten wire was positioned at the centre of the platinum ring and lowered so that the ring was suspended halfway along the length of the wire. Etching was performed in a 2 M NaOH electrolyte held within the platinum ring, with a 3.5 V DC voltage applied. Upon completion of the etching process, the bottom half of the wire was caught in a glass beaker filled with shaving foam (Gillette Classic) to prevent the tip-end from contacting any surfaces.[8] The tip was then washed with ethanol and ultrapure water (MilliQ®, 18.2 MΩ) and examined under a microscope. If the tip was sufficiently sharp, it was stored upright in a container at room temperature until use. Before measurement, the tip was inserted into the tip holder of the linear scanner.

2.6 X-Ray Photoelectron Spectroscopy

XPS measurements were conducted on Au (111) and Pt (111) substrates prepared using the protocols detailed above. Where indicated, these substrates were modified with nanoparticles and a hexanethiol (HT) self-assembled monolayer (SAM) via immersion. Nanoparticles were also deposited onto highly oriented pyrolytic graphite (HOPG) via drop casting. XPS spectra were recorded using a Kratos AXIS Ultra DLD spectrometer equipped with an Al Kα monochromatic X-ray source (1486.6 eV) and a pass energy of 20 eV. Binding energies were calibrated to the C1s peak at 285.0 eV. XPS peak fitting was performed using CASA software with the Shirley background (BG) type.[9] The substrate preparation for XPS and subsequent measurements were carried out by Santiago M. Solans and Pilar Cea at the University of Zaragoza, Spain.

2.7 Cyclic Voltammetry

All electrochemical measurements were conducted using a three-compartment electrochemical cell (Figure 2.1). Measurements were performed with a μAutolab III potentiostat controlled with GPES software. The reference electrode for all experiments was a Hg/HgO electrode (0.1 M NaOH), and all potentials were converted to the reversible hydrogen electrode (RHE) scale upon data plotting using the formula as follows, where the pH was 13:

$$V_{RHE} = V_{Hg/HgO} + 0.165 + (0.059 \times pH)$$

Electrolyte solutions were prepared using NaOH (99.99%, Alfa Aesar) and glycerol (≥99%, Sigma). For experiments performed in 0.1 M NaOH and 0.1 M glycerol, glycerol was added directly to the NaOH electrolyte already in the electrochemical cell to act as a supporting electrolyte. Typically, the cell contained approximately 80 mL of the NaOH electrolyte. The amount of electrolyte was always specifically measured, to ensure the correct calculation of glycerol to be added. Prior to measurements, argon gas was bubbled through the electrolyte to deoxygenate it and was passed over the solution during measurements to maintain an inert atmosphere.

The working electrode was either an Au or Pt microelectrode (ø = 25 µm), or an Ag electrode (ø = 2 mm), cleaned and prepared as described previously. The counter electrode was a Au flag, with an approximate area of 50 mm^2. This was cleaned prior to use by flame annealing in a butane flame and quenching in ultrapure water (MilliQ®, 18.2 MΩ).

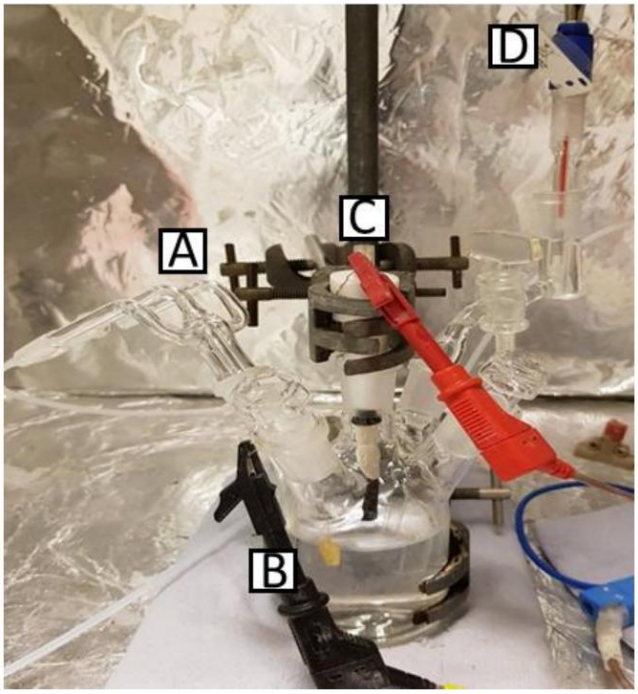

Figure 2.8 Experimental setup of the cell for electrochemical experiments showing (A) the Ar gas inlet, (B) gold working electrode, (C) working electrode and (D) the reference electrode.

2.8 References

1 M. Brust, M. Walker, D. Bethell, D. J. Schiffrin and R. Whyman, *J Chem Soc Chem Commun*, 1994, 801–802.

2 H. Qian and R. Jin, *Chemistry of Materials*, 2011, **23**, 2209–2217.

3 E. Pensa and T. Albrecht, *J Phys Chem Lett*, 2018, **9**, 57–62.

4 M. Brust, M. Walker, D. Bethell, D. J. Schiffrin and R. Whyman, *J Chem Soc Chem Commun*, 1994, 801–802.

5 A. I. Yanson, P. Rodriguez, N. Garcia-Araez, R. V Mom, F. D. Tichelaar and M. T. M. Koper, *Angewandte Chemie International Edition*, 2011, **50**, 6346–6350.

6 P. Klapetek, D. Nečas and C. Anderson, Gwyddion User Guide, http://gwyddion.net/.

7 C. A. Schneider, W. S. Rasband and K. W. Eliceiri, *Nat Methods*, 2012, **9**, 671–675.

8 Y. I. Yanson, *How additives affect Cu electrodeposition : an electrochemical STM Study*, Leiden Institute of Physics (LION), Faculty of Science, Leiden University, 2012.

9 G. H. Major, N. Fairley, P. M. A. Sherwood, M. R. Linford, J. Terry, V. Fernandez and K. Artyushkova, *Journal of Vacuum Science & Technology A*, 2020, **38**, 61203.

3. Modification of Gold and Platinum Substrates with Silver Nanoparticles

Chapter Contents

This chapter focuses on the modification of Au and Pt substrates with Ag nanoparticles (NPs). The metal-thiol (M-S) bond strength for both Au and Pt is known to be greater than that for Ag, which is expected to drive the thiol redistribution effect.[1,2] The disintegration of the capping layer may subsequently aid in driving the decomposition of the unstable Ag NP core on the Au and Pt substrates, as observed in the Au-Au NP system.[3–5] An entropic driving force favouring thiol migration is also anticipated for Ag NPs on both substrate materials. Therefore, the Ag NPs are expected to sit unprotected on these substrates. This outcome will be particularly interesting to characterise, as it may give rise to new electrochemical properties for the mixed-metal systems. It is known that Au and Ag are miscible at both the bulk and nanoscale, suggesting that the Au substrate modified with Ag may exhibit alloy-like electrochemistry.[6–9] In contrast, while Ag and Pt are immiscible at the bulk scale, bimetallic alloy NPs of these metals have been successfully synthesised.[10–14] It will be intriguing to see whether these metal interactions are reflected in the electrochemistry of the modified Pt substrate.

This chapter aims to determine whether thiol redistribution occurs, whether the exposed Ag NPs on the substrates remain intact, partially disintegrate, or fully disintegrate, and whether the modified substrates exhibit electrochemical behaviour reflective of these processes. It details the synthesis of Ag NPs via cathodic corrosion, their immobilisation onto Au and Pt substrates, and the characterisation of the modified substrates using XPS, STM, and cyclic voltammetry.

3.1 Silver Nanoparticle Synthesis and Characterisation

Silver nanoparticles were synthesised using the cathodic corrosion method. The NPs used for the reported surface modifications of Au and Pt surfaces in this chapter were produced using setup B, and a variety of different amplitude and frequency parameters were tested (detailed in 2. Materials and Methods). The two parameter sets that yielded particle product are shown in Table 3.1.

Table 3.1 Synthesis parameters for silver nanoparticles.

Sample	Electrolyte	Amp. (V)	Offset (V)	Freq. (Hz)	CE	Observations
AG_1	0.1 M $NaNO_3$	±5	-5	10	Pt	Some effervescence at WE. Observed a green/silver tint to solution after approx. 1 hour, and full dissolution of the 1 mm immersed wire.
AG_2	0.1 M $NaNO_3$	±5.5	-5.5	10	Pt	For 1 mm of immersed wire, synthesis time of >5hrs.

The morphology and particle size distribution of both samples was investigated via TEM imaging. It is important to note that the samples were prepared, cleaned and deposited onto TEM grids before thiol addition. This procedure was followed to prevent any potential organic contamination and to ensure that the particles were imaged as soon after their synthesis as possible.

TEM images of sample AG_1 (Figure 3.1) showed large structures; however, further magnification uncovered smaller, distinct features. These features generally appear spherical in shape, though some do vary in morphology. A size distribution analysis was conducted by manually measuring the diameter of the particles, and measurements were taken in one direction only, rather than averaging across a cross-section, as the

particles often lay at the edge of a larger structure, which obstructed the ability to measure the diameter in the perpendicular direction.

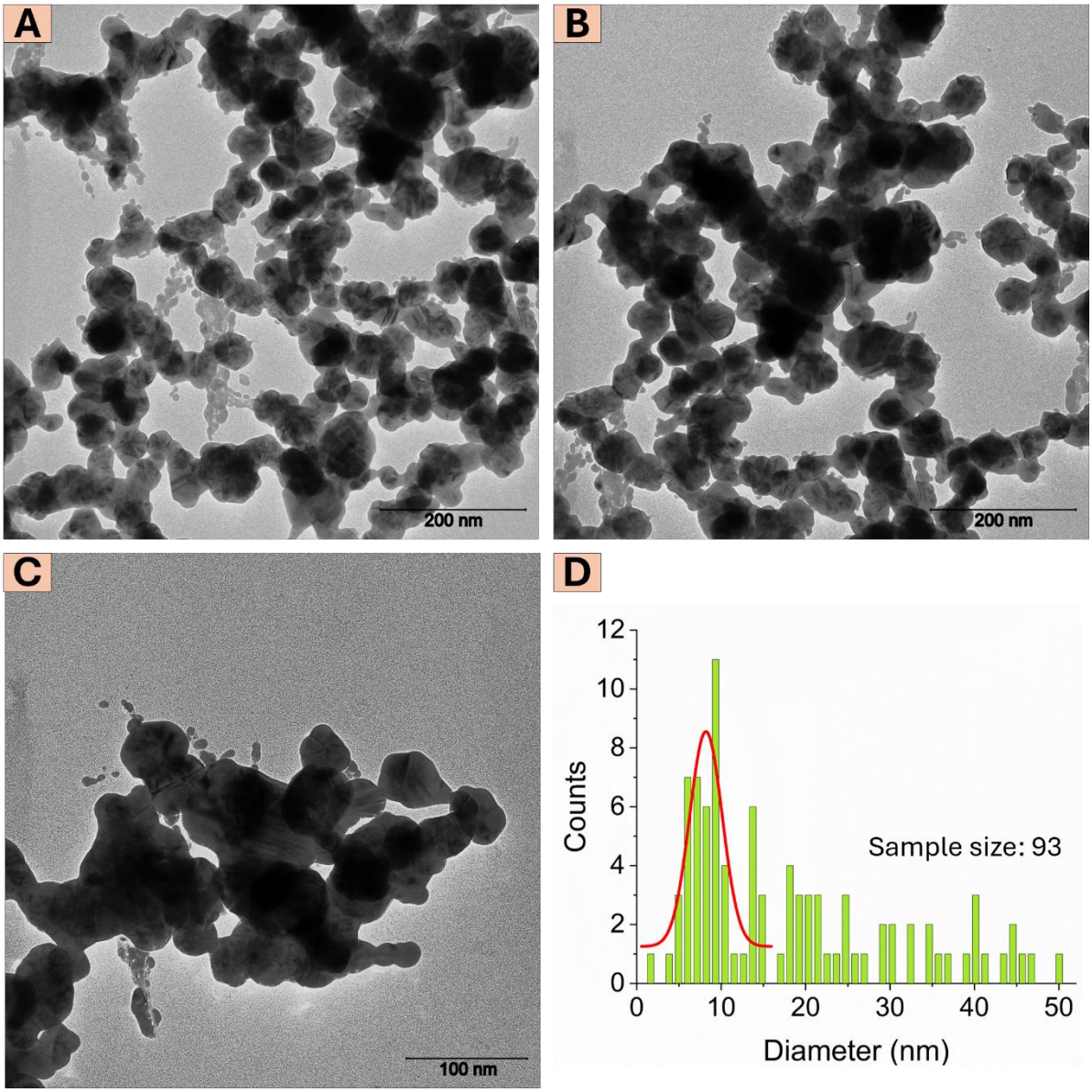

Figure 3.1 (A-C) TEM images of Ag nanoparticles, produced via cathodic corrosion parameters AG_1. **(D)** Particle size distribution analysis.

Size analysis across various images of sample AG_1 revealed an average particle size of 8.19 ± 0.49 nm, excluding larger features where individual features could not be defined due to overlapping features. The larger structures observed may result from nanoparticle

agglomeration during the drying process, as there are regions in the image where clustering is apparent, indicated by layered or overlapping features. These larger features may also be the result of oxidation of the Ag surface, as Ag NPs will oxidise when stored under ambient conditions for even a day.[15] A way to overcome the latter effect will have been to perform the imaging on the day of synthesis, but due to synthesis times and instrument limitations this was not possible.

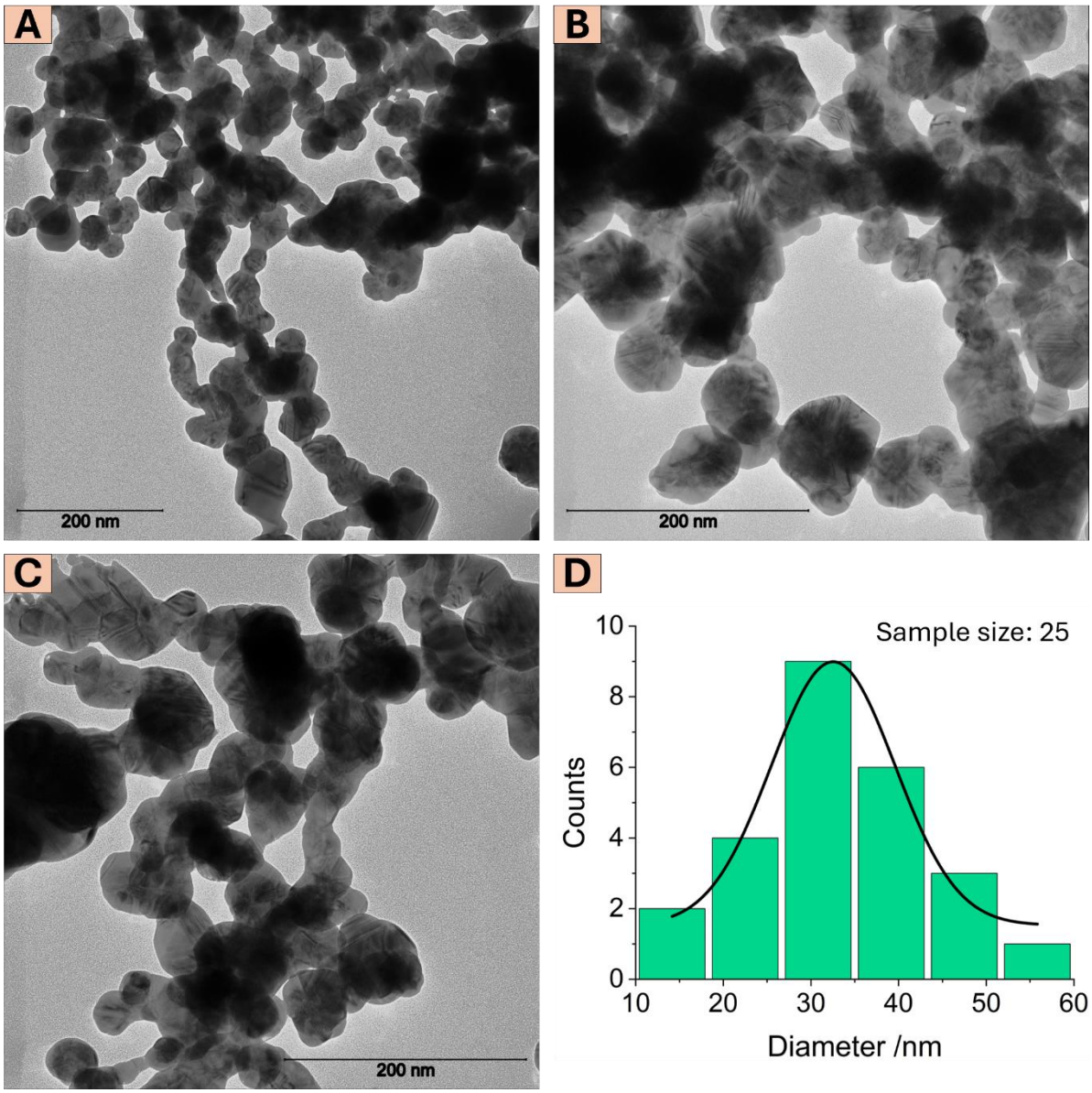

Figure 3.2 (A-C) TEM images of Ag nanoparticles, produced via cathodic corrosion parameters AG_2. **(D)** Particle size distribution analysis.

TEM imaging of the AG_2 sample (Figure 3.2) reveals larger features, and size distribution analysis gives an average diameter of 32.5 ± 7.1 nm. In contrast to sample AG_1, smaller nanoparticles are not observed in between or surrounding larger features. The larger features predominantly exhibit a round shape, although it should again be noted that the boundaries of these larger structures seem to comprise more than one particle. This observation suggests that an increase in amplitude from ±5 V to ±5.5 V, altering the applied potential range from 10 V to 11 V peak-to-peak amplitude, yields a noticeable difference in the size of the particles produced. This observation was consistent across two other samples when taken for TEM imaging, where it was seen that particles produced using the AG_2 parameters were larger.

The impact of varying the applied potential on the size of Ag NPs synthesised via cathodic corrosion has not been reported in literature. An increase in the applied potential leads to a higher current density at the WE during synthesis. This is likely the primary factor affecting particle size, as other parameters such as the electrolyte composition, concentration and frequency remain unchanged across the two synthesis experiments. This result for Ag particles is in line with work by Koper *et. al.,* which demonstrated that an increase of the current density of the WE resulted in larger platinum particles.[16]

For experiments involving the immobilisation of Ag NPs on Au and Pt substrates, particles synthesised using the parameter set AG_1 were chosen for their smaller nanoparticle size and efficient synthesis. Before their use in modifying metal surfaces, the particles were thiolated with 1-hexanethiol and cleaned via centrifugation.

3.2 Modification of Gold Substrates

This subchapter reports the characterisation of Au substrates modified with Ag nanoparticles (NPs) via overnight immersion in a solution of thiolated Ag NPs, as described in 2.3.4 Modification of Metal Substrates with Nanoparticles. The modified Au substrate was characterised using STM imaging to determine the dimensions of the Ag NPs once immobilised on the Au surface. This provided insights into the stability of the Ag NPs—if thiol redistribution occurred as expected, the dimensions of the Ag features on the substrate could reveal whether decomposition of the Ag NP cores occurred and to what extent.

XPS was used to identify the preferential binding sites of thiols in the system, adding further detail to the understanding of thiol redistribution and exposure of Ag cores.

Cyclic voltammetry was used to evaluate the electrochemical behaviour of the modified surface. Initial measurements were performed in 0.1 M NaOH, followed by an investigation of glycerol electrooxidation on the modified substrate in 0.1 M glycerol (with 0.1 M NaOH as a supporting electrolyte). If the CVs showed only an Au electrochemical response, this indicated that the Ag NPs either retained their ligand shell or were not electrochemically active upon immobilisation and interaction with the Au substrate. Observation of both Au and Ag electrochemical features would indicate thiol redistribution, resulting in electrochemically active Ag features on the substrate, which were similar in electroactivity to bulk Ag. If the CVs exhibited features that could not be attributed to either Au or Ag electrochemistry, one potential reason could be the formation of an alloy.

3.2.1 STM of Ag NPs on Au (111)

An Au (111) substrate modified with Ag NPs via overnight immersion was characterised via STM. The STM images of Ag NPs on Au (111) are presented in Figure 3.3 (A), and revealed both particle-like features and larger structures across the Au substrate. The diameter of the smaller features, presumed to be isolated particles rather than agglomerates, was measured across several images by averaging the diameter in perpendicular directions. The average diameter of the Ag features was 5 ± 1.2 nm. This value differs from the 8.19 ± 0.49 nm diameter obtained via TEM, though it is important to

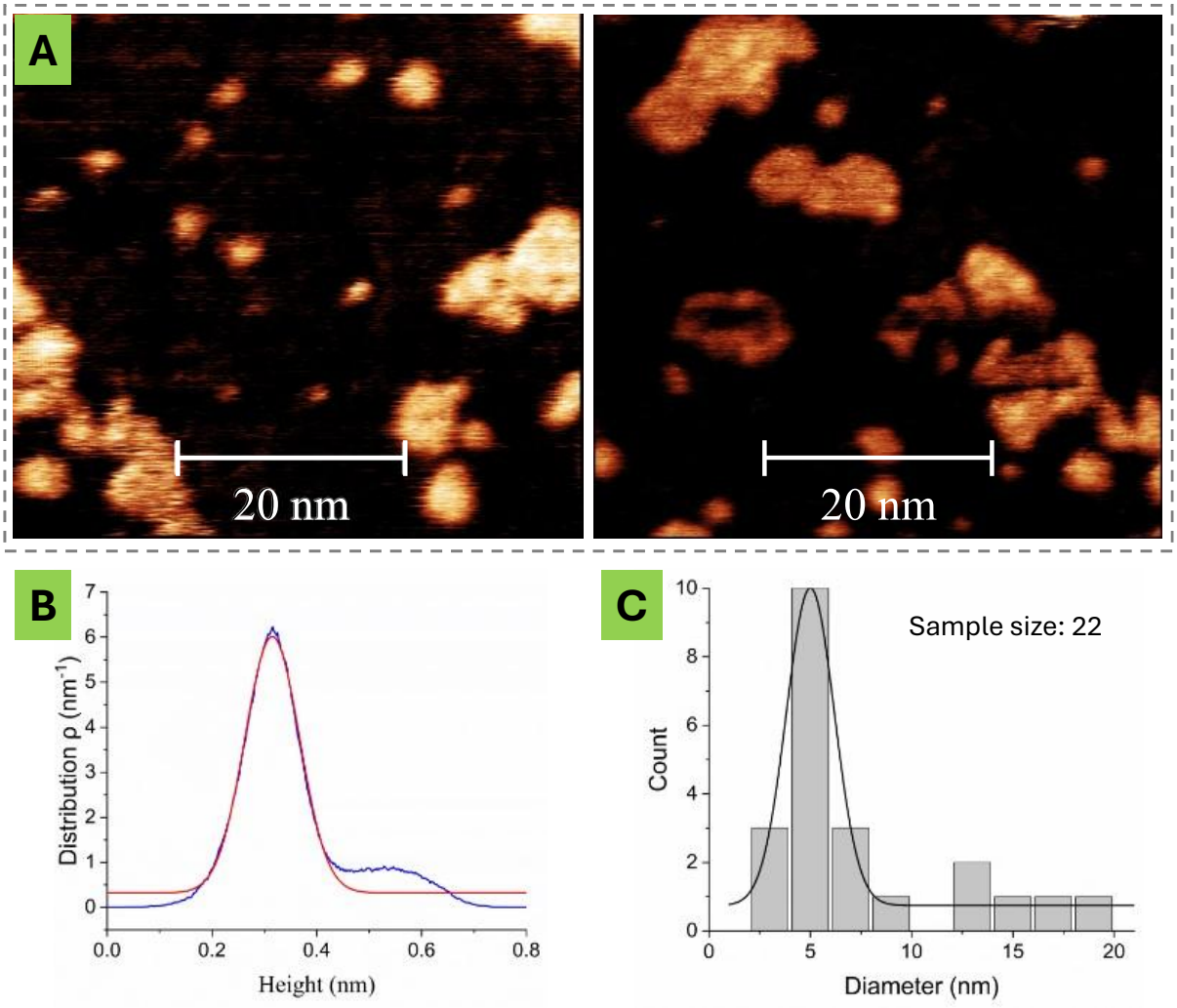

Figure 3.3 (A) STM images of Ag nanoparticles on an Au (111) disc, and the size distributions of the **(B)** height and **(C)** diameter (lateral) of the nanoparticles.

note that the particles imaged via STM were thiolated, while those measured via TEM were not, thereby hindering particle agglomeration effects.

The height of the Ag features was measured across multiple STM images, resulting in an average height of 0.315 ± 0.05 nm. This value was significantly smaller than the particle diameter measured via STM, indicating that these features are islands rather than intact nanoparticles. Given that the height of an Ag (111) monoatomic step is 0.236 nm, it is plausible that some of the observed features are monoatomic Ag islands on the Au substrate.[17] Additionally, the larger structures observed may be agglomerates of these island features.

These findings align with expectations, as the difference in M-S bond strengths, as well as entropic favourability, would likely drive a thiol redistribution process, leading to the exposure of an unstable Ag NP core. STM imaging has demonstrated that this core does not remain intact but decomposes into monoatomic island features.

To further evaluate this process, the preferential binding of thiols in the modified substrate was investigated using XPS.

3.2.2 XPS of Ag NPs on Au (111)

Ag nanoparticles were immobilised onto an Au (111) substrate, and XPS measurements were conducted following the procedure described in 2.6 X-Ray Photoelectron Spectroscopy. To characterise the binding energy (BE) values of the M-S interactions, several measurements were performed. Ag NPs were first deposited on HOPG to determine the BE of thiols bound to the Ag NP surface (S-Ag NP). Separately, 1-hexanethiol (HT) was deposited on Au (111) to obtain the S-Au BE. Finally, Ag NPs were immobilised onto Au (111) to evaluate whether thiols preferentially bound to the Au substrate or remained on the Ag NP surface. The resulting XPS spectra are displayed below, along with Table 3.2, which summarises the BE values obtained across the different measurements. The fitted peak positions were consistent across samples within ±0.1–0.2 eV, and the relative component areas were reproducible within ±5%, providing confidence in the reliability of the fits.

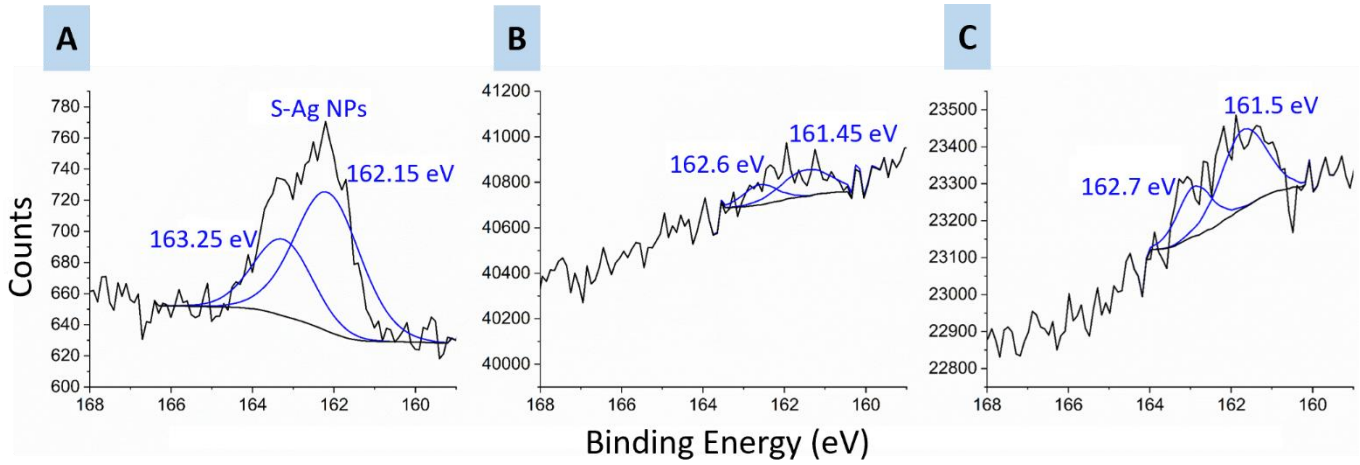

Figure 3.4 XPS of Ag NPs **(A)** drop-cast onto HOPG, and immobilised on an Au (111) substrate via **(B)** immersion and **(C)** drop-casting.

Experiment 1 in Table 3.2 presents the results for Ag nanoparticles deposited on HOPG. The XPS spectrum in Figure 3.4 revealed BE values of 163.25 eV and 162.15 eV. The peak at 163.25 eV has been attributed to the S atoms of free thiol groups, while the peak at 162.15 eV is in good agreement with the literature value of 162 eV for an S-Ag bond.[18,19]

Experiment 2 in Table 3.2 shows the results for Ag NPs immobilised onto an Au (111) substrate via immersion. The XPS data produced a weak signal, but peak fitting revealed signal positions at 161.45 eV and 162.6 eV. Literature suggests that a BE value of approximately 161 eV is typically attributed to sulfur in a sulfide chemical state.[20,21] The same peak positions were observed in Experiment 3, where the signal strength was enhanced by drop casting the Ag NPs onto the Au substrate instead of using an immersion protocol.

Both S2*p* signals obtained for the modified substrate (161.5 eV and 162.7 eV) exhibit a shift compared to the BE values measured for Ag NPs on HOPG. Additionally, the 162.7 eV signal does not correspond to literature or measured values for 1-hexanethiol binding with either of the pure metals (Experiments 1 and 4), with the only report being for thiolphenol molecules bound to a silver surface.[22]

As the BE value of 162.6/162.7 eV in the mixed Ag NP/Au system differs from the S-Ag NP and S-Au BEs measured and is also shifted to lower BE values relative to thiolated Ag NPs on HOPG, it suggests that the thiol binding on the modified substrate is different from pure metal-thiol binding observed on either Au or Ag.

While the S 2*p* region could in principle be fitted with a single doublet, a two-component fit was applied to account for the asymmetry of the envelope and the presence of distinct chemical environments. The additional component improved the overall fit quality,

particularly on the low-binding-energy side, and is consistent with previous reports where both chemisorbed thiolates and more weakly bound sulfur species contribute to the signal.

Table 3.2 Summary of the measured BE values via XPS studies on the Ag NP-Au substrate system.

Experiment		Signal		
		S2*p* (eV)		3*d* (eV)
1	Ag NPs on HOPG	162.15	163.25	368.4
2	Ag NPs on Au (111) via immersion	161.5	162.7	367.8
3	Ag NPs on Au (111) via drop casting	161.45	162.6	367.8
4	HT on Au (111)	162.2	163.4	

Further analysis was conducted on the Ag 3*d* region of the spectra (Experiments 1 to 3). For Ag NPs on HOPG, a peak was observed at 368.4 eV, characteristic of an elemental Ag peak.[22] However, when deposited onto Au (111) via both drop casting and immersion, the peak shifted to 367.8 eV, which has been attributed to silver oxide (Ag_2O).[23]

Taken together, the evidence suggests that sulfur binding in the Ag NP/Au system differs from its binding to the Ag NP surface and the Au (111) surface. STM results indicated that the Ag cores decompose into Ag islands, pointing to some disintegration of the thiol capping layer. XPS results further show that thiols remain bound to the metals in the system but at shifted BE values compared to the pure metals, which may suggest alloying between the bulk Au and the nanoscale Ag features. Additionally, the 3*d* spectral region suggests the formation of Ag oxide, a process that could further drive the decomposition of the Ag cores.

To further investigate, the electrochemical behaviour of the system was examined to gain additional insights into the structure of the surface.

3.2.3 Electrochemistry of Ag NPs on Au in 0.1 M NaOH

The electrochemistry of Ag NPs on a polycrystalline Au electrode was investigated in 0.1 M NaOH to examine any changes in the characteristic voltammetric response of the Au electrode. The voltammograms were analysed to determine whether the Ag NPs were electrochemically active and if their behaviour resembled that of bulk Ag. Electrochemical activity would suggest that the thiols redistributed to some extent, exposing Ag features. If the electrochemical behaviour did not match that of the Au electrode and a bulk Ag electrode, it would align with the XPS findings that indicated alloy and oxide formation.

After the cleaning of synthesised Ag NPs, an attempt was made to characterise the supernatant in order to determine whether excess thiol was still present. The sample was centrifuged, and the supernatant removed, after which an Au electrode was immersed in the solution overnight and the resulting CV measured. The voltammogram was not notably different to that of the unmodified, clean electrode CVs presented later in this chapter. However, it must be noted that if excess thiol is present, thiol–thiol interactions may prevent its uptake into the supernatant. Therefore, when interpreting the electrochemical results in this work, the potential contribution of excess thiols to the

observed effects must also be considered. Alternative interpretations on this basis will be highlighted where relevant.

Figure 3.5 displays the CV scans for both clean Au and Ag electrodes. The CV of the Au microelectrode exhibited characteristic features consistent with those reported in literature.[24,25] In the double layer region, between ca. 0.23 and 0.77 V_{RHE}, hydroxide anions adsorb onto the electrode surface, leading to the formation of an Au oxide layer, with an oxidation peak (peak A) observed in the anodic scan between 1.09 and 1.51 V_{RHE}. In the cathodic scan, the reduction of this oxide layer is observed with a peak at 0.92 V_{RHE} (peak, B).

The unmodified Ag CV exhibits a response typical of a polycrystalline Ag electrode in alkaline media.[26–28] In the anodic scan, two shoulder peaks are observed at 1.04 and 1.13 V_{RHE}, before a large oxidation peak at 1.21 V_{RHE} (peaks C'- C''', respectively). All three peaks are attributed to the formation of multilayers of silver oxide (Ag_2O).[26] The first shoulder peak is attributed to the formation of AgOH intermediate species, which undergo conversion to the more stable Ag_2O or dissolution as Ag (I) species, while the second shoulder is assigned to the growth of the Ag_2O layer as well as some dissolution of Ag species.

The large oxidation peak (peak C''') is also attributed to the further formation of Ag_2O. The peak at 0.9 V_{RHE} in the cathodic scan was attributed to the reduction of oxide layer (peak D).[27]

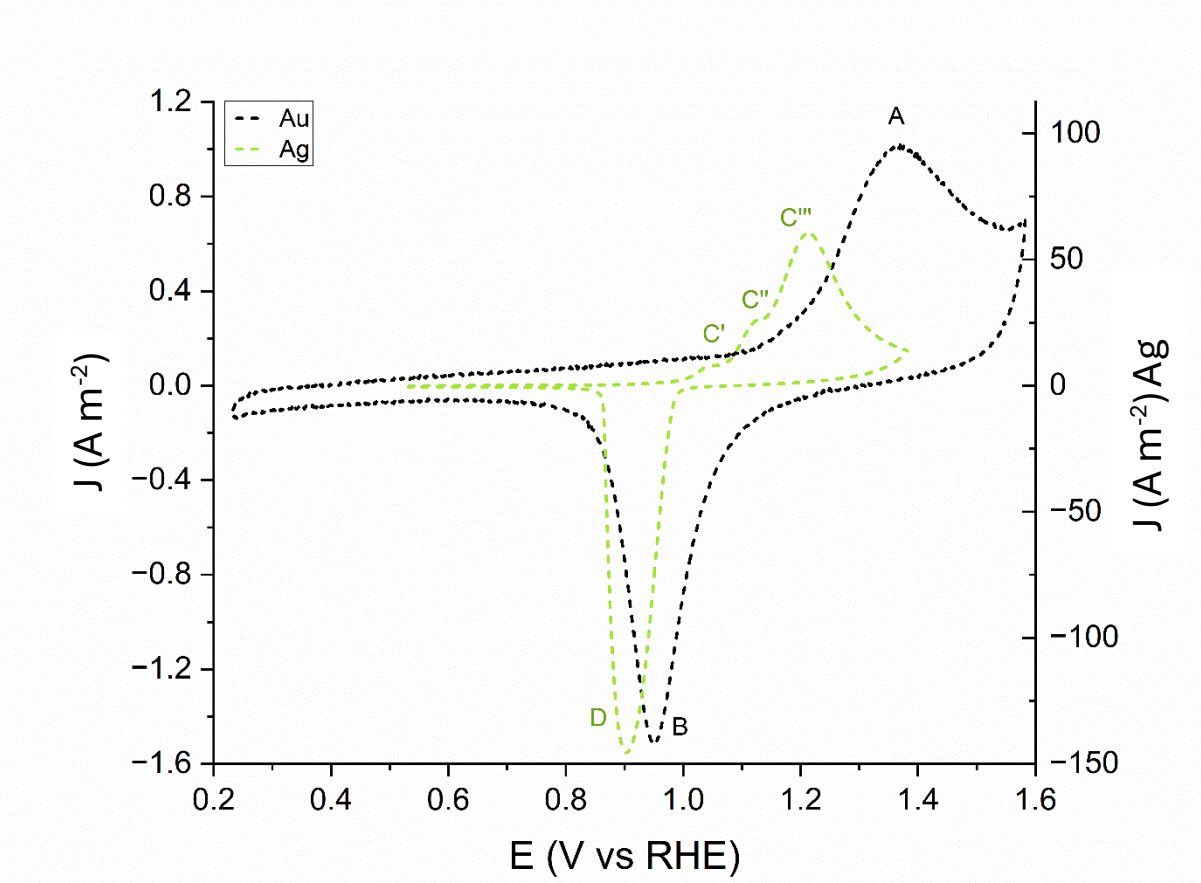

Figure 3.5 The CVs of an unmodified Au electrode (black, left scale), and an unmodified Ag electrode (green, right scale). CVs were recorded in 0.1 M NaOH, v = 50 mV s^{-1}. Au ⌀ = 25 µm, Ag ⌀ = 2 mm.

The first and final CV scans of the Ag NP-modified Au electrode are presented in Figure 3.6 (A). In comparison to the clean Au voltammogram, the modified system CVs showed a significant decrease in current density. The currents of these scans were observed to fit within those of the double layer region of the Au electrode.

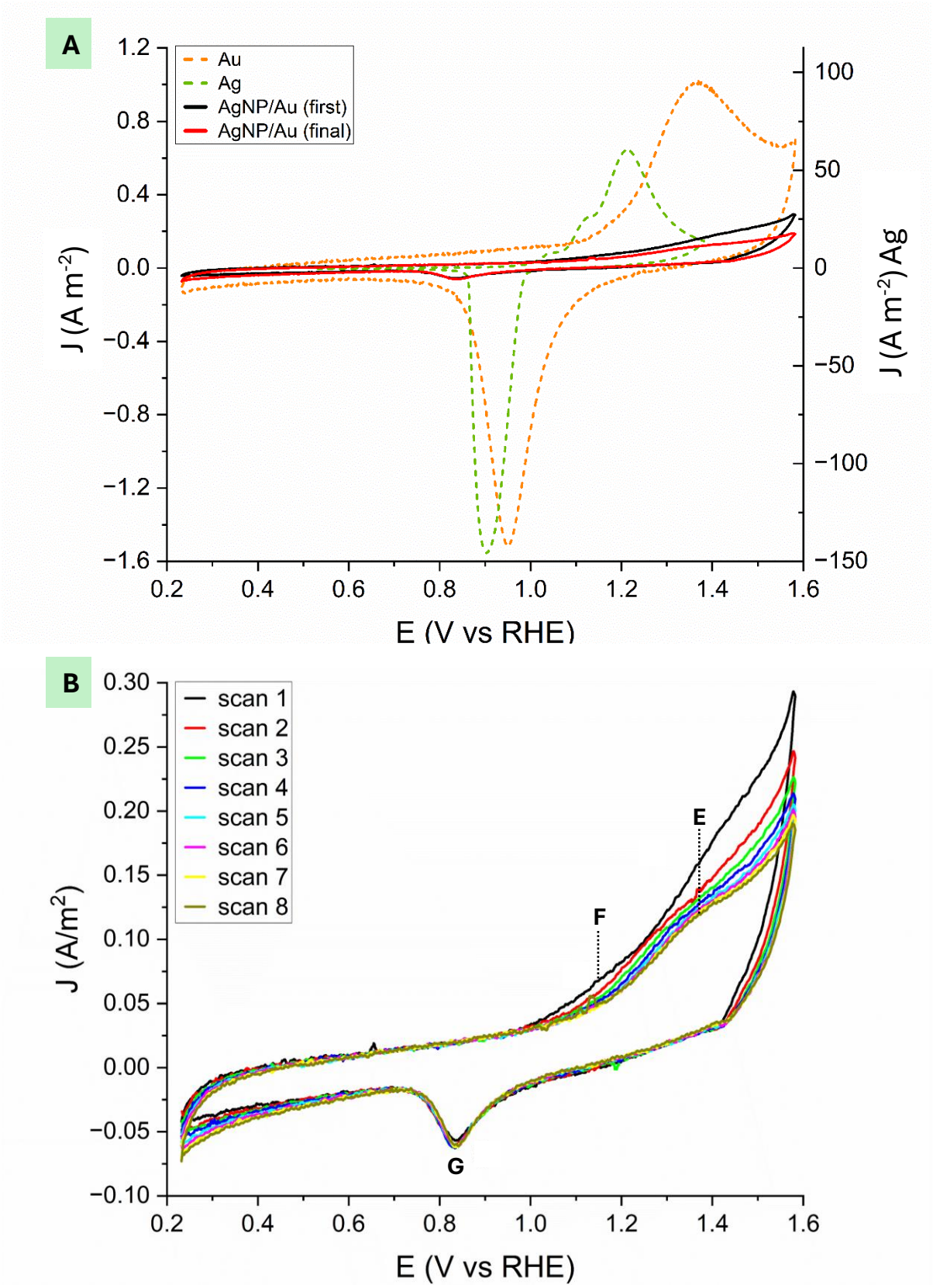

Figure 3.6 (A) CVs of an Au electrode (yellow), Ag electrode (green), and the first (black) and last (red) scans of the Au electrode modified with Ag NPs, **(B)** All CVs measured over the course of an experiment of the Ag NP-modified Au electrode. CVs were recorded in 0.1 M NaOH, v = 50 mV s^{-1}. Au ⌀ = 25 µm, Ag ⌀ = 2 mm.

To better discern the observed voltammetric features, only the scans of the modified electrode are plotted in Figure 3.6 (B). In the first scan, during the anodic sweep, a peak is observed at approx. 1.4 V_{RHE} (peak E), which then shifts to 1.36 V_{RHE} within subsequent scans. This may be attributed to Au oxide formation, as the oxidation peak for this process was observed across this potential in Fig. 3.5. We also observe a shoulder in scan 1 at approx. 1.16 V_{RHE} (peak F), though this disappears over subsequent scans. This peak does not align directly with values for either Au or Ag oxide formation, though may be more closely linked with Ag activity, as it occurs at a potential between the potentials of the second and third Ag anodic oxidation peaks (peaks C'' and C'''). In the cathodic scan, a reduction peak is observed at 0.84 V_{RHE} (peak G). This peak is shifted to more negative potentials than either the Ag oxide or Au oxide reduction peaks, though only by 60 and 80 mV, respectively.

3.2.3.1 Expanded Potential Window

The modified electrode was then measured with a potential window extended to more negative potentials to reach the region where thiol desorption occurs. In literature, hexanethiol is reported to desorb from an Au (111) electrode in 0.1 M NaOH at approximately 0.11 V_{RHE}.[29] The resultant CVs are presented in Fig. 3.7. In the first scan, a significant decrease in current magnitude was observed, in line with the measurements presented in Figs 3.5 and 3.6. Upon cycling within this potential window, the characteristic Au CV was largely recovered, due to thiol desorption, with the oxide formation and reduction features becoming more pronounced and resembling the unmodified Au CV. However, this recovery was not a complete one, as the current densities in the final scan were still suppressed in comparison to the clean Au electrode,

the oxidation peak exhibited a different voltammetric shape, and the reduction peak was negatively shifted.

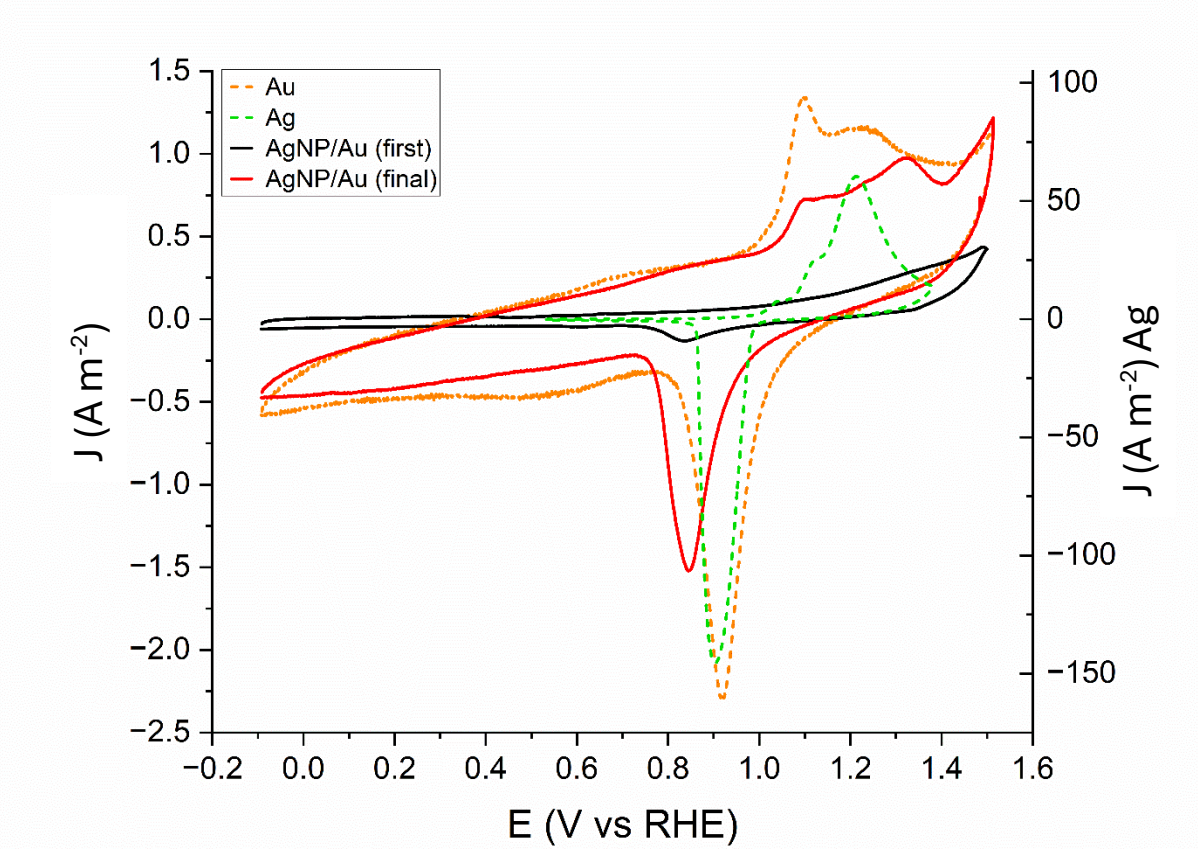

Figure 3.7 The CVs of an unmodified Au electrode (yellow), unmodified Ag electrode (green), and the first (black) and last (red) scans of the Au electrode modified with Ag NPs. CVs were recorded in 0.1 M NaOH, v = 50 mV s^{-1}. Au ⌀ = 25 µm, Ag ⌀ = 2 mm. Total number of scans = 17.

All scans measured in this experiment are presented in Figure 3.8, highlighting that the first few scans differ significantly from the final scan. Notably, the voltammetric shape remains largely unchanged from the fourth scan onwards.

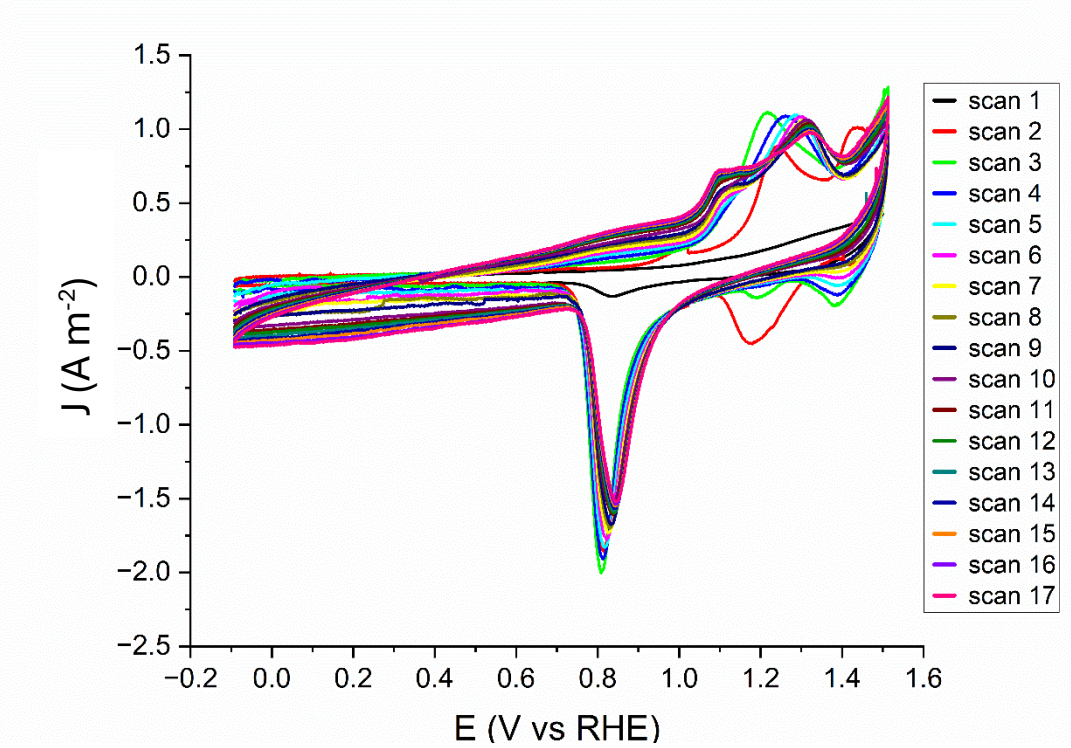

Figure 3.8 All CVs measured over the course of an experiment of the Ag NP-modified Au electrode in 0.1 M NaOH, v = 50 mV s^{-1}. Au ⌀ = 25 µm.

This is more clearly illustrated in Figure 3.9, which displays only the first three scans of the modified electrode. Scan 1, as previously discussed, shows minimal voltammetric features, likely due to the passivation of the electrode by thiols. In Scan 2, peaks are observed in the anodic scan at 1.24 and 1.43 V_{RHE} (peaks i, ii) that do not directly correspond to those seen for Au oxide formation but fall within the potential region associated with the oxide formation of both Au and Ag.

Additionally, two reduction peaks not observed in the unmodified electrode CV are observed in the cathodic scan at more positive potentials of 1.17 and 1.43 V_{RHE} (peaks iii, iv). This suggests a redox process takes place at these potentials, which decreases upon cycling of the potential.

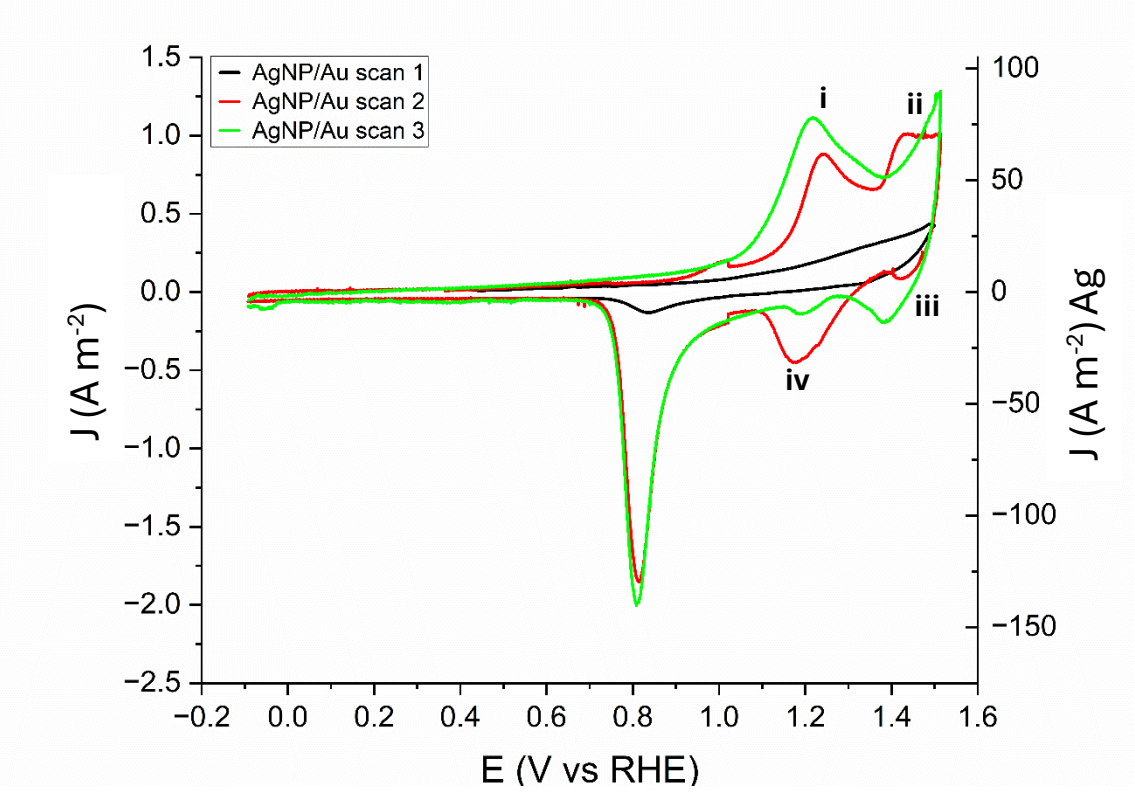

Figure 3.9 Plot of the first three CVs of the Ag NP-modified Au electrode in 0.1 M NaOH, v = 50 mV s^{-1}. Au ⌀ = 25 µm, Ag ⌀ = 2 mm.

These redox peaks are not due to the oxidative re-adsorption of thiols at positive potentials, as this occurs at more negative potentials for hexanethiol on an Au (111) electrode in 0.1 M NaOH.[29] It has been noted that when the positive potential limit exceeds 1.4 V_{RHE} for a polycrystalline Ag electrode in 0.1 M NaOH, a silver oxide reduction peak appears at approximately 1.3 V_{RHE}.[30,31] However, this does not correspond directly with the potentials of peaks iii and iv. As the potential is continually cycled into these high potentials, surface roughening and dissolution of the Ag likely cause the decrease in contribution of these peaks in both the anodic and cathodic scan directions.

Additionally, the large Au oxide reduction peak in the cathodic scan is shifted from 0.92 V_{RHE} to 0.8 V_{RHE}. This negative shift may be attributed to the increased complexity of the oxide layers formed during the anodic scan, potentially comprising both Au and Ag

oxides. This shift could also indicate potential alloying between Au and Ag metals, as it does not align directly to either Au or Ag reduction peak potentials, or alternatively, structural changes as a result of the adsorption of excess thiols.

The cyclic voltammograms in 0.1 M NaOH, measured over an expanded potential window, reveal the emergence of Ag features contributing to the overall voltammogram. As the potential is cycled, these Ag features diminish, but the CV of the Au electrode does not fully recover, indicating that some Ag remains on the surface. To differentiate the oxide formation and reduction peaks between the two metals in the system, the electrochemistry was subsequently measured in the presence of glycerol.

3.2.4 Electrochemistry of Ag NPs on Au in 0.1 M NaOH and 0.1 M Glycerol

The electrooxidation of glycerol by the three metals of interest (Au, Ag, and Pt) results in voltammetric responses and features distinct from each other, with minimal overlap. Thus, the introduction of glycerol aimed to more clearly reveal any new voltammetric features arising from the surface modification.

The CV for a polycrystalline Ag electrode in 0.1 M NaOH, with and without the addition of 0.1 M glycerol (GlyOH), is presented in Figure 3.10. No significant differences are observed in the voltammetric profile upon the addition of glycerol.

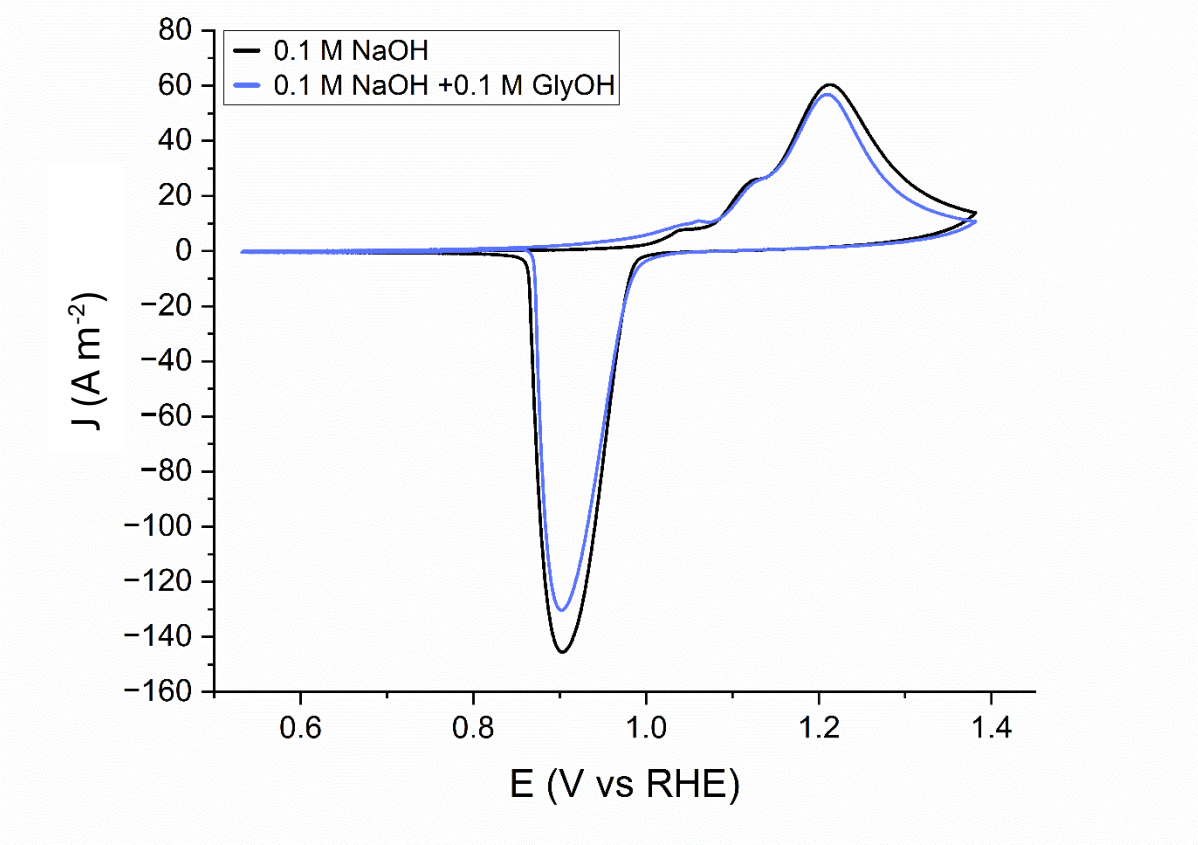

Figure 3.10 The CVs of an Ag electrode in 0.1 M NaOH (black) and in 0.1 M NaOH and 0.1 M GlyOH (blue). v = 50 mV s^{-1}. Ag ⌀ = 2 mm.

In the anodic scan, two anodic oxidation shoulders and a main peak were observed at potentials of 1.06, 1.13 and 1.21 V_{RHE}, respectively, along with a reduction peak at 0.9 V_{RHE}.

As previously mentioned, the peaks in the anodic scan of Ag are attributed to the formation of Ag_2O multilayers. The electrooxidation of glycerol relies on the presence of hydroxyl groups adsorbed at the electrode surface.[30] Within the potential window used, AgOH intermediate species are formed during the first oxidation shoulder peak at 1.04 V_{RHE}. This accounts for the slight increase and change in shape of the first shoulder peak in the presence of glycerol. As the AgOH intermediate converts to form Ag_2O layers, the oxidation of glycerol is hindered due to the lack of available adsorption sites or adsorbed OH species. Consequently, significant glycerol electrooxidation is not observed within the chosen potential window.

Figure 3.11 displays the CVs for clean Au and Ag electrodes, along with the first and final scans for the Au electrode modified with Ag NPs, within a shorter potential window selected for Ag stability. The response of the Au electrode in the presence of 0.1 M glycerol is in agreement with literature, exhibiting a primary oxidation peak in the anodic scan direction and a secondary oxidation peak in the cathodic scan.[32] As the potential increases in the anodic scan, hydroxide ions begin to adsorb until a specific coverage is achieved, corresponding to the charge specific to glycerol adsorption, after which the primary oxidation peak is observed at 1.1 V_{RHE}.

The formation of the Au oxide monolayer prevents further oxidation of glycerol at more positive potentials due to a lack of available adsorption sites. In the cathodic scan, the reduction of the Au oxide monolayer reactivates the Au surface as active sites become available for the adsorption of glycerol near the electrode surface, resulting in the secondary oxidation peak at 0.99 V_{RHE}.

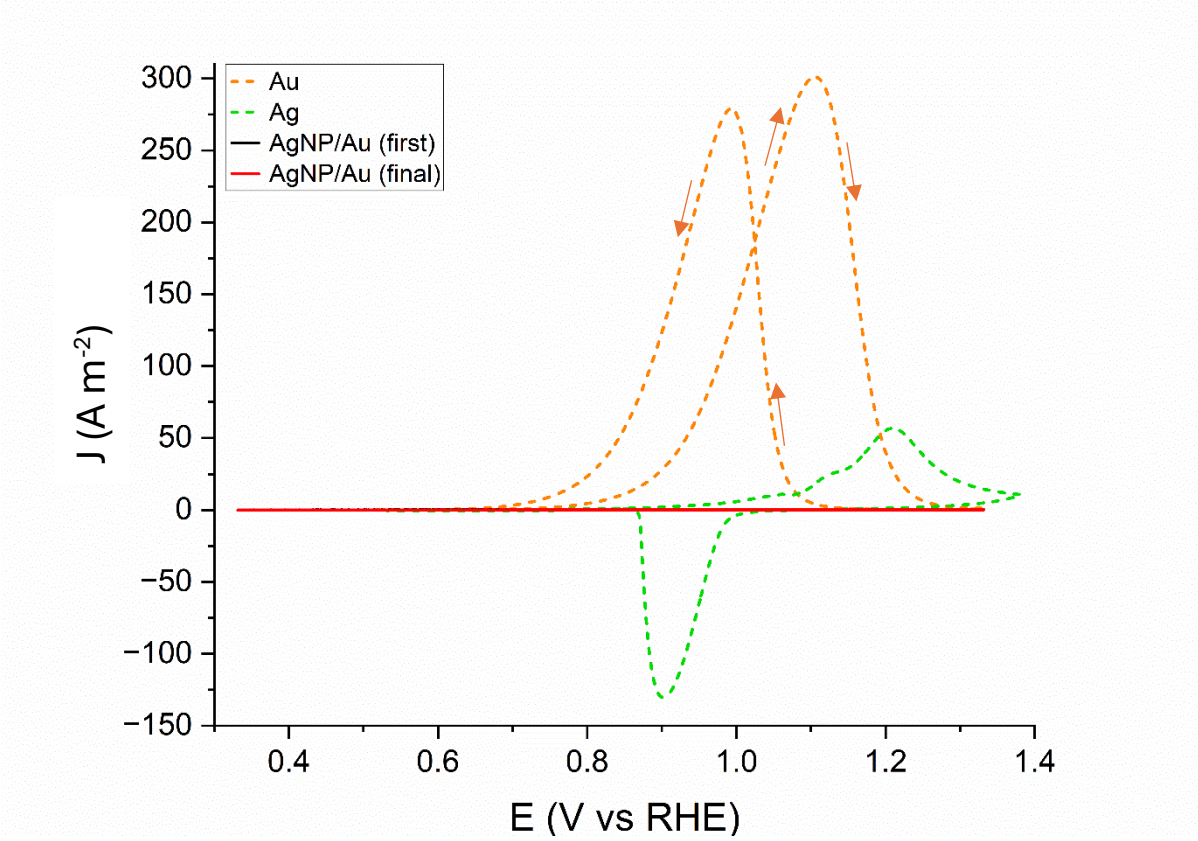

Figure 3.11 The CVs of the unmodified Au (yellow) and Ag (green) electrodes, and the first (black) and last (red) scans of the Au electrode modified with Ag NPs. CVs were recorded in 0.1 M NaOH + 0.1 M GlyOH, v = 50 mV s^{-1}. Au ⌀ = 25 µm, Ag ⌀ = 2 mm. Total number of scans = 13.

The voltammograms for the Ag modified Au electrode show a significant reduction in current density compared to the clean CVs of both Au and Ag. All measured scans for the modified electrode are plotted separately in Figure 3.12. In the first scan, a peak in the anodic direction is observed at 1.23 V_{RHE} (peak A), which may be attributed to the

formation of Ag_2O, as previous results indicate that occurs at 1.21 V_{RHE}. This peak cannot easily be linked to the electrocatalysis of glycerol on Au, which occurs at 1.1 V_{RHE} in the anodic scan direction. Additionally, in the anodic sweep, a feature emerges at 0.93 V_{RHE} as the potential is cycled (peak B). This feature cannot be attributed directly to either Au or Ag activity, as the potential does not correspond to any of the peaks observed in the CVs of either Au or Ag electrodes.

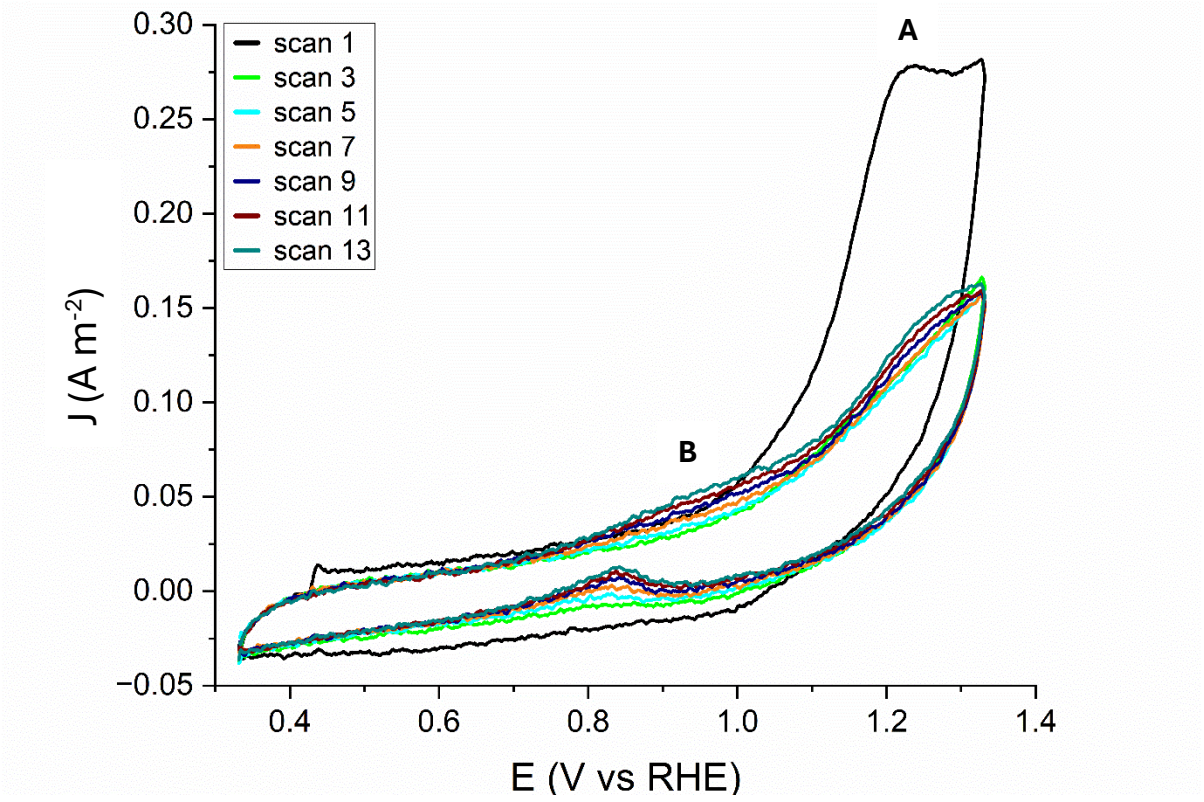

Figure 3.12 Some scans of the Ag NP-modified Au electrode in 0.1 M NaOH + 0.1 M GlyOH, v = 50 mV s^{-1}. Au ⌀ = 25 µm.

In the cathodic scan, a peak at 0.84 V_{RHE} was observed, which appears to be an oxidation peak. This may indicate the adsorption of glycerol molecules on the electrode surface, although it does not match the previously measured value at 0.99 V_{RHE} for this process on Au. It is interesting to note here that this feature in the cathodic scan occurs at the same

potential as the feature observed in the cathodic scan for the same electrode system in the absence of glycerol, where a reduction peak was noted at 0.84 V_{RHE}. However, without being able to accurately ascribe a specific process to the peaks, it is not possible to conclusively link the two observations.

3.2.4.1 Expanded Potential Window

Figure 3.13 displays the first and final scans for the same system, with measurements performed in the expanded potential window. In this new measurement window, the Ag electrode exhibits two oxidation peaks in the cathodic scan, at 1.43 and 1.28 V_{RHE}. The assignment of these peaks is made difficult as literature on the electrooxidation of glycerol using Ag typically restricts the potential window to below 1.4 V_{RHE}.

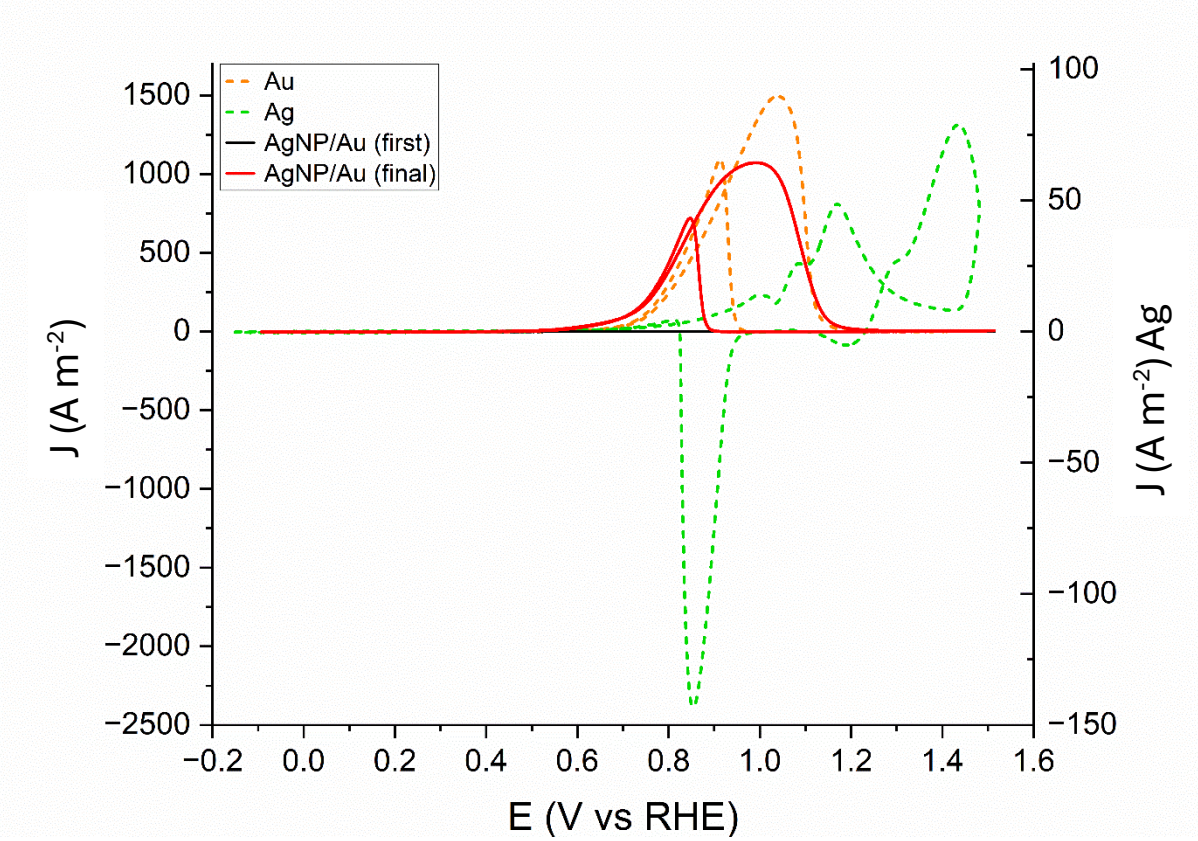

Figure 3.13 The CVs of the unmodified Au (yellow) and Ag (green) electrodes, and the first (black) and last (red) scans of the Au electrode modified with Ag NPs. CVs were recorded in 0.1 M NaOH + 0.1 M GlyOH, v = 50 mV s^{-1}. Au ⌀ = 25 µm, Ag ⌀ = 2 mm.

There is also a reduction peak at 1.2 V_{RHE}, which likely corresponds with the reduction of Ag oxides formed during the anodic scan.

The first scan of the Au electrode modified with Ag NPs still shows a significantly decreased current density when compared to the CV for a clean Au electrode. However, the final scan displays only the voltammetric features characteristic of bulk Au, indicating that the Au surface is mostly recovered upon potential cycling and removal of thiols at more negative potentials. Notably, though no Ag voltammetric features are observed in the final scan, the current density is not recovered to the values of a clean Au electrode.

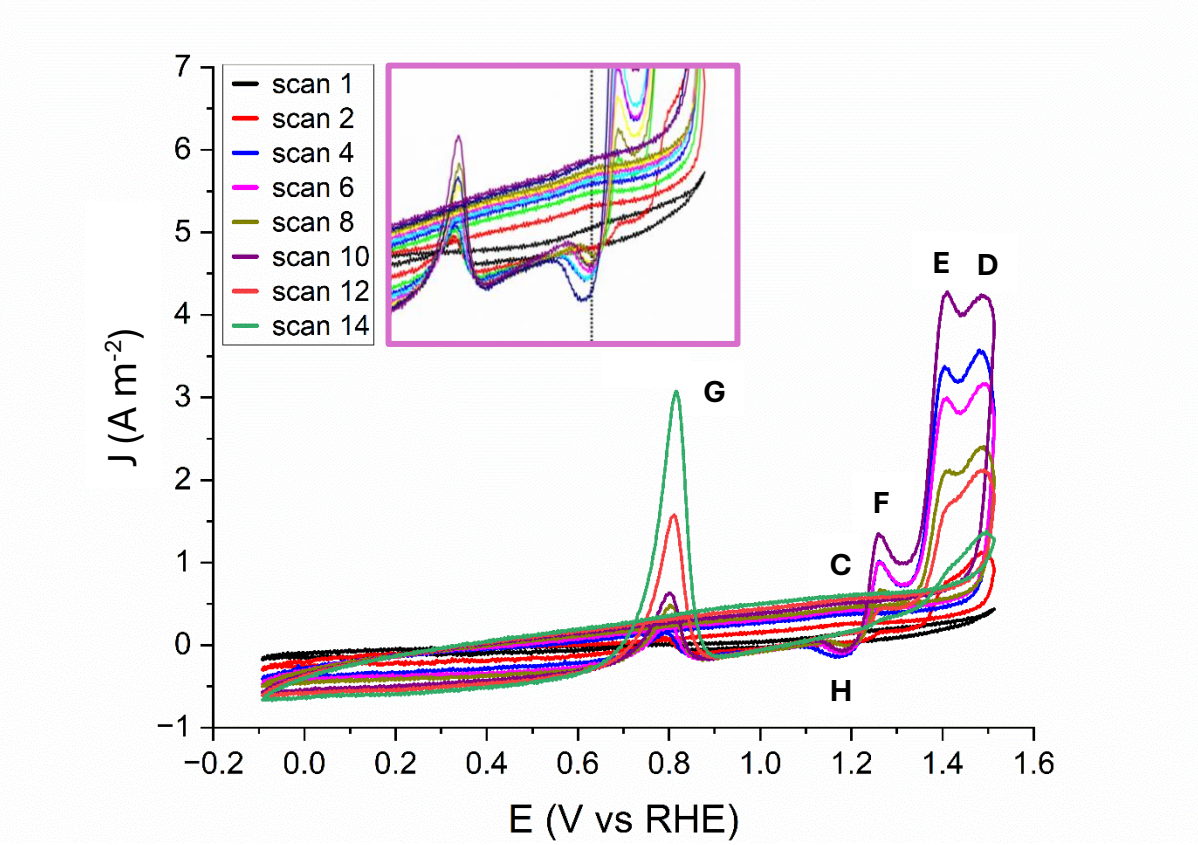

Figure 3.14 The first ten CVs measured of the Ag NP-modified Au electrode in 0.1 M NaOH + 0.1 M GlyOH, v = 50 mV s^{-1}. Inset: Enlarged region of peak 'c'. Au ⌀ = 25 µm.

Upon further examination of the initial scans, presented in Figure 3.14, one can see that there are additional voltammetric features that are not observed in either the unmodified Au CV or the final scans when the Au surface has been recovered.

In the anodic scan, there is a broad feature at 1.2 V_{RHE} (peak C), while the cathodic scan shows oxidation peaks at 1.5, 1.4, 1.26 and 0.8 V_{RHE} (peaks D - G), and a reduction peak (H) at 1.17 V_{RHE}.

Peak C occurs at the same potential as the Ag oxide formation peaks on pure Ag, as well as the potential at which glycerol undergoes primary oxidation on Au. Peaks D, E and F occur at across the potentials at which cathodic oxidation peaks were observed for pure Ag in the extended potential window, though it must be noted that they occur as two peaks, where only one peak is observed for pure Ag, indicating a difference in the observed electrochemistry versus bulk Ag. The cathodic reduction peak, H, also aligns in position with the reduction peak observed for pure Ag. It was observed that initially, as the potential is scanned, peaks C, D, E, F, G and H all increase in current density, showing an increase in Au and Ag electrochemistry as the thiols are removed from the electrode surface. The peaks assigned only to Ag electrochemistry (D, E, and F) begin to decrease in current density, eventually disappearing and becoming masked by the growth of peaks C and G, which are the peaks observed as the primary and secondary oxidation peaks in the final scan.

This shows us that a mixed system is observed initially, with peaks being assigned to pure Au, pure Ag, and peak E which differs from both pure metals. We note that these features were observed to initially increase in current density as the electrode potential is cycled.

However, the Ag activity decreases and is eventually masked by Au activity, while the Au electrode voltammogram is largely recovered.

3.2.5 Discussion

STM imaging of Ag NPs deposited onto Au (111) revealed the presence of monoatomic islands instead of intact Ag nanoparticles. This observation suggests that the thiol capping layer migrates sufficiently to expose the unstable particle core, resulting in its decomposition.

XPS measurements of the modified Au substrate revealed signals in the 3d region corresponding to silver oxide, as well as S2p BE values at 161.45 eV and 162.6 eV (see Table 3.2). The latter could not be attributed to either S-Ag NP or S-Au bonds, as it does not align with the BE values obtained for those systems. While the value of 162.6 eV may correspond to some form of thiol interaction with either Au or Ag, the shift in the BE value suggests that this interaction is distinct from thiol binding with the bulk metals and may indicate alloying behaviour between the two metals. The difficulty in assigning this BE value for the modified substrate prevents a definitive conclusion about whether thiols migrate from the Ag surface. However, the decomposition of the Ag cores and the formation of islands observed in STM imaging provide evidence that some level of thiol migration must occur.

When measuring the CVs of Ag NPs on an Au electrode within a limited potential window, the current densities of the modified electrode were significantly lower than those of the unmodified Ag and Au electrodes across all measured scans. This reduction in current

density is attributed to the passivation of the modified electrode by thiols, either as a result of the migration process or due to the potential presence of excess thiols.

Expanding the potential window into the region where the reductive desorption of hexanethiol from Au is known to occur revealed the emergence of features unrelated to typical Au electrochemistry. In 0.1 M NaOH, anodic peaks were observed in the potential region corresponding to both silver oxide and gold oxide formation. Additionally, peaks appeared in the cathodic scan that could not be definitively assigned to either Au or Ag-specific electrochemistry but may be related to Ag activity, as they occurred at similar potentials to silver oxide reduction when a silver electrode is pushed to higher potentials. The current density of these additional peaks decreased upon continued potential cycling. The gold oxide reduction peak exhibited a shift to more negative potentials, and notably, the gold surface was not fully recovered. The oxidation peak displayed features that could not be attributed to either Ag or Au individually.

In the presence of glycerol, voltammetric features corresponding to both Ag and Au were observed, along with a feature that could not be assigned to either pure metal. This further supports the alloying behaviour suggested by the XPS data. Over time, the peaks associated with Au-specific activity increased and eventually began to dominate those attributed to Ag, likely due to the oxidative removal of Ag.

In the electrochemical measurements, both Au and Ag voltammetric contributions were observed, along with the emergence of features not specifically attributable to the electrochemistry of either metal. Two scenarios may be considered when interpreting these results. If we take the view that excess thiol is present in the system, then in the CVs - whether in the expanded potential window or otherwise - the observed current

suppression could be explained simply as the electrode surface being saturated with excess thiols. The emergence of features that cannot be attributed to either Ag or Au electrochemistry may then be the result of structural changes induced due to the free thiols present. The emergence of Ag-specific electrochemical features upon potential cycling indicates that the progressive removal of thiols exposes the underlying Ag. This must also be considered alongside the STM results, which revealed the formation of Ag islands. For such islands to be observed, the thiol shell must have undergone some degree of disintegration. However, the STM measurements did not involve potential cycling for thiol desorption, and so while excess thiols may contribute to the observed effects of current suppression, the expected thiol migration process – based on metal-thiol energetics we have explored - cannot be ruled out as also being at play. This is further supported by the XPS data, in which the measured binding energies did not align with those for 1-hexanethiol bound to either the Au substrate or the Ag particle surface, indicating that the modified surface cannot simply be explained by saturation with excess thiols. It may then be that free thiols present play a role in the attachment and degradation of the Ag NPs, though this is something that must be explored in greater detail.

In the view that the NP cleaning procedure effectively removes free thiols, we then have the following interpretation: the new features may result from Au-Ag alloying, as Au and Ag are known to be miscible at both the bulk and nanoscale.[6–9] Studies of Au-Ag systems indicate that Ag tends to exhibit surface enrichment when combined with Au; however, those studies typically involve carbon-supported catalysts or bimetallic nanoparticles, whereas this system differs in that it involves the mixing of a bulk material and nanoparticles of the respective metals. [6,33] We propose that thiol migration leads to the

decomposition of Ag cores, in line with expectations. The stronger S-Au bond compared to the S-Ag bond, combined with the bulk Au substrate offering significantly more binding sites than the Ag nanoparticles, drives thiol redistribution. The energetics of the system also favour S-Au binding over S-Ag binding. Some thiols remain bound to the resulting Ag islands, and these islands exhibit varying behaviours: some undergo Au-Ag alloying, while others oxidise, resulting in BE values differing from those of their bulk metal counterparts. The features associated with alloy formation are reflected in the new electrochemical characteristics observed in the voltammograms.

3.3 Modification of Platinum Substrates

This section focuses on the characterisation of Pt substrates modified with Ag nanoparticles via overnight immersion in a solution of thiolated Ag NPs, as described in 2.3.4 Modification of Metal Substrates with Nanoparticles. The aim was to evaluate the stability of Ag NPs on Pt substrates by characterising the modified surface. Although no XPS or STM data were collected for this system, its characterisation was performed using cyclic voltammetry, first in 0.1 M NaOH and subsequently in the presence of 0.1 M glycerol.

As explained for the Ag–Au system (Section 3.2.5), it is necessary to consider the possibility of free thiol remaining in the sample, even after cleaning. Although characterisation of the supernatant suggested little to no electrochemical activity, thiol–thiol interactions may prevent full detection. In the present case, where no supporting XPS or STM data are available, the contribution of free thiols to the observed voltammetric behaviour cannot be entirely ruled out. This caveat should therefore be kept in mind when interpreting the electrochemical results discussed in this section.

3.3.1 Electrochemistry of Ag NPs on Ptin 0.1 M NaOH

A polycrystalline Pt electrode modified with Ag nanoparticles was characterised using cyclic voltammetry to evaluate changes in the characteristic voltammetric features of the Pt electrode.

Figure 3.15 displays the unmodified Pt and Ag electrode CVs, as well as the first and final scans for the Ag NP- modified Pt surface. The features of the Ag voltammogram are as described earlier in the chapter. For the Pt voltammogram: In the anodic direction, peaks

with maximum currents at potentials of 0.13 and 0.25 V_{RHE} are observed, corresponding to hydrogen desorption at Pt (110) and (100) sites. In the cathodic sweep, peaks appear at positions corresponding to those in the positive scan, with peaks at 0.23 and 0.11 V_{RHE}, attributed to hydrogen adsorption.[34] Extending the potential window more negatively would enter the region of hydrogen gas evolution. As the potential is made more positive in the anodic sweep, a peak with an onset of 0.41 V_{RHE} is observed, attributed to oxide formation on the Pt surface. In the cathodic sweep, a peak at 0.57 V_{RHE} is seen, corresponding to the reduction of these oxides.[35]

The first scan is markedly different from the final scan, featuring a large anodic peak with an onset at approximately 0.9 V_{RHE} (peak A).

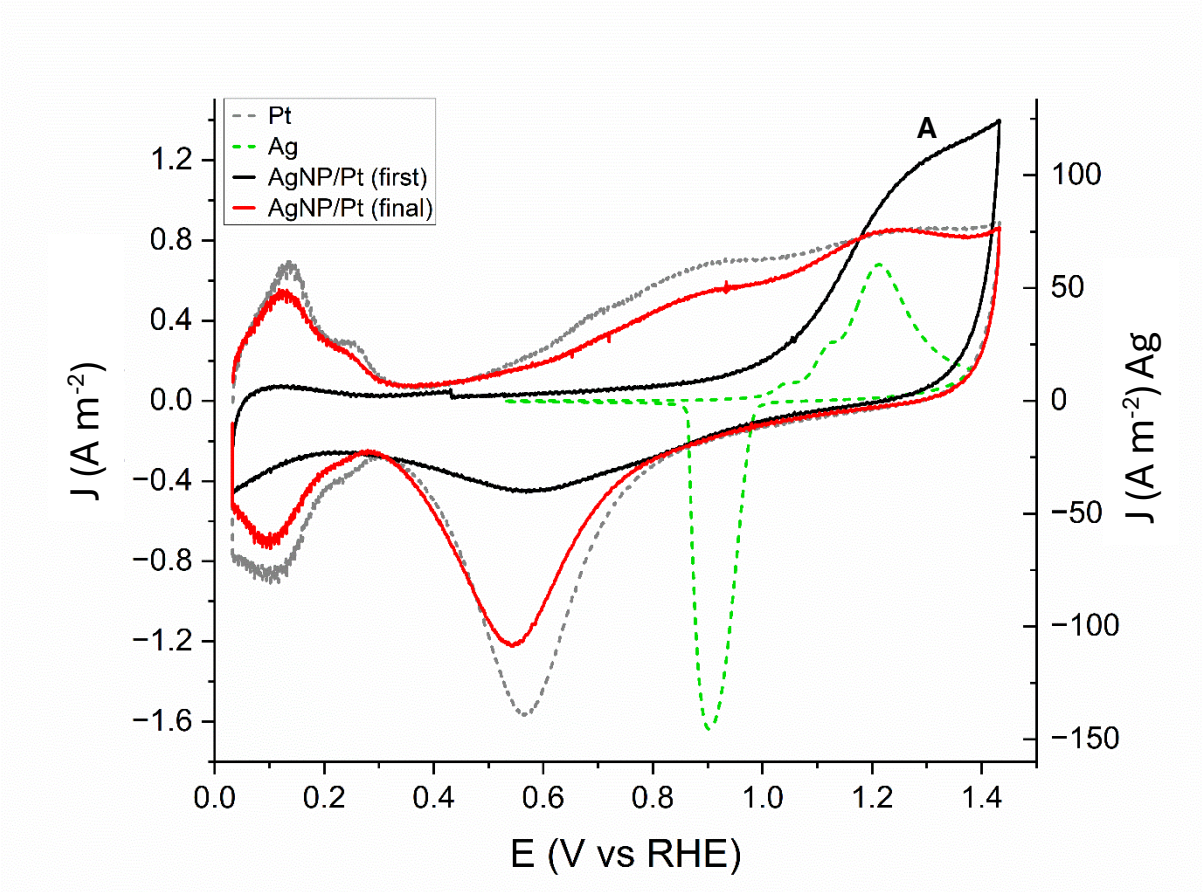

Figure 3.15 The CVs of unmodified Pt (grey) and Ag (green) electrodes, and the first (black) and last (red) scans of the Pt electrode modified with Ag NPs via incubation. CVs were recorded in 0.1 M NaOH, v = 50 mV s^{-1}. Pt ⌀ = 25 µm, Ag ⌀ = 2 mm. Total number of scans = 8.

This onset, delayed in comparison to that observed for the unmodified Pt electrode, could potentially be due to the influence of Ag, as the Ag oxidation peaks occur at more positive potentials than those of Pt, in the potential region where peak A is observed. In the cathodic sweep, a reduction peak at 0.57 V_{RHE} aligns with the reduction of Pt oxides observed in the unmodified Pt CV. The final scan indicates that cycling the potential of the electrode within these potentials leads to the recovery of Pt features, albeit with a more pronounced feature in the region of peak A.

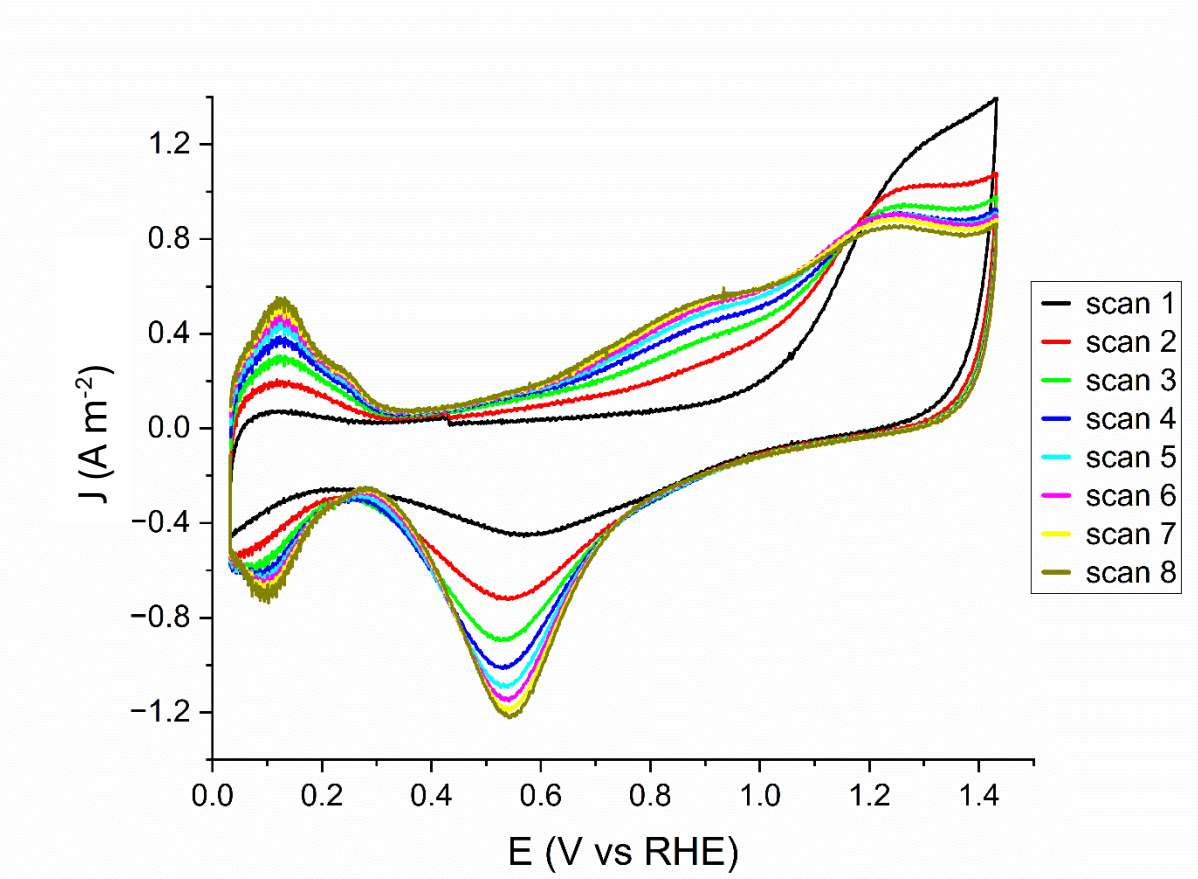

Figure 3.16 All CVs measured over the course of an experiment of the Ag NP-modified Pt electrode in 0.1 M NaOH, v = 50 mV s^{-1}. Pt ⌀ = 25 µm.

Figure 3.16 displays all the measured scans for this electrode. As the applied potential is cycled, platinum characteristics such as hydrogen adsorption and desorption are regained, and the Pt-oxide formation and reduction peaks increase in current density to

more closely resemble the unmodified Pt CV. This recovery of the hydrogen region and the increasing reduction of the oxide layer from the Pt are likely due to the removal of thiols from the electrode surface.

As mentioned, as the potential is cycled, peak A, assigned to Ag electrochemistry, becomes less apparent but does not disappear entirely. To remove the difficulty in decoupling this peak from that of Pt oxide formation, the electrochemical response of the modified surface was measured in the presence of glycerol.

3.3.2 Electrochemistry of Ag NPs on Pt in 0.1 M NaOH and 0.1 M GlyOH

In the presence of glycerol, Pt and Ag electrodes exhibit voltammetric features at distinct potentials, making it straightforward to assign features to each metal due to the lack of overlap. The first and last CVs of the Ag-modified Pt electrode in the presence of glycerol, along with the CVs for unmodified Pt and Ag electrodes, are presented in Figure 3.17. As discussed earlier, Ag does not significantly contribute to the electrooxidation of glycerol within this potential window, whereas Pt does exhibit glycerol electrooxidation. The CV features of the Pt electrode align with those reported in the literature, with a primary oxidation peak in the anodic scan at 0.68 V_{RHE} and a secondary oxidation peak in the cathodic scan at 0.5 V_{RHE}.[36]

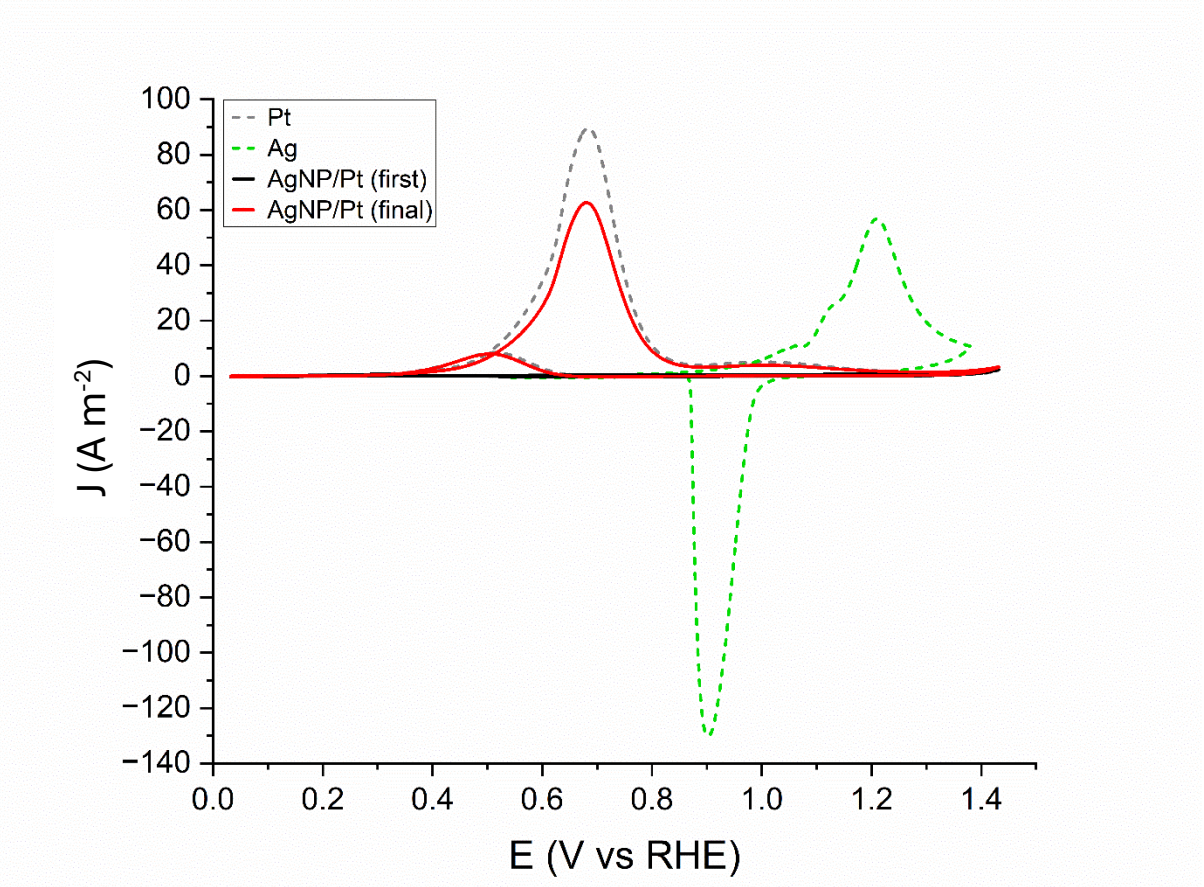

Figure 3.17 The CVs of unmodified Pt (grey) and Ag (green) electrodes, and the first (black) and last (red) scans of the Pt electrode modified with Ag NPs. CVs were recorded in 0.1 M NaOH + 0.1 M GlyOH, v = 50 mV s^{-1}. Pt ⌀ = 25 µm, Ag ⌀ = 2 mm. Total number of scans = 18.

The first scan exhibits a significantly decreased current density compared to the unmodified CVs, likely due to the passivation of the electrode by thiol species. The final scan shows a voltammogram resembling that of a clean Pt electrode, indicating a recovery of the Pt surface. However, the current densities do not fully match those recorded for the clean Pt electrode, suggesting the presence of a species on the Pt surface that blocks active sites and is not electrochemically active.

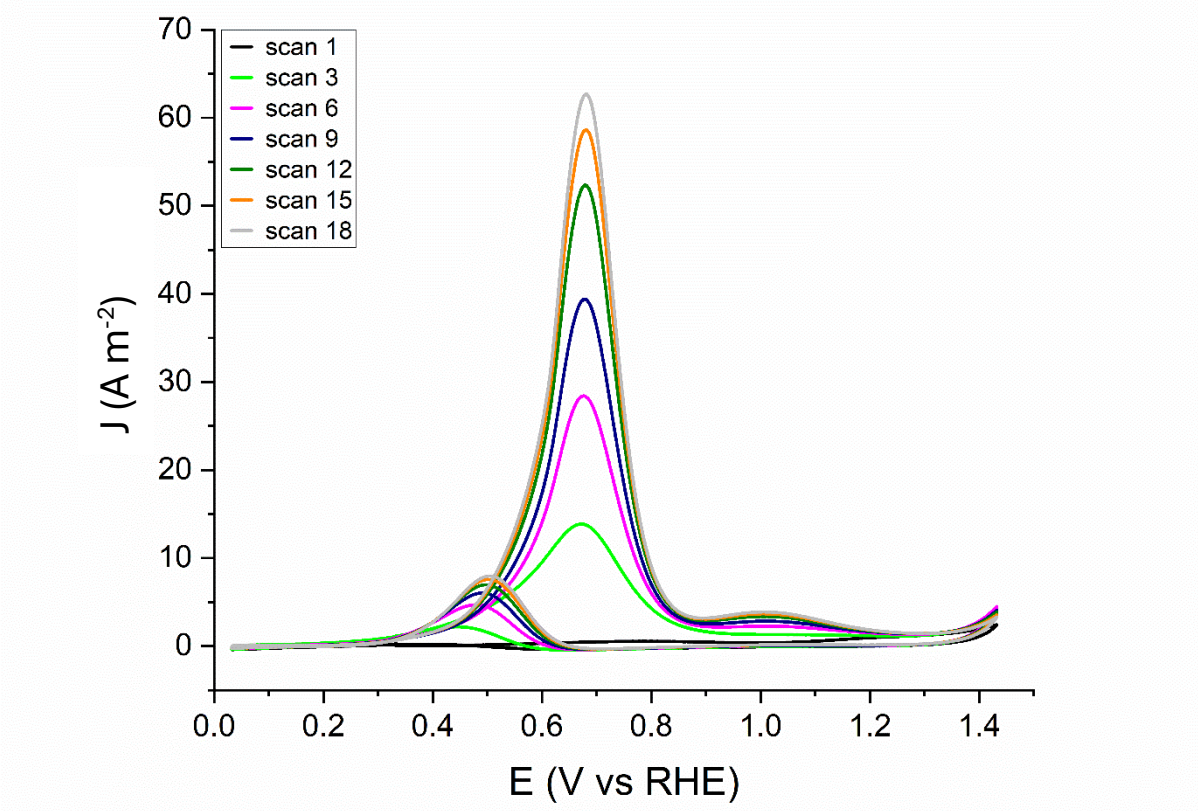

Figure 3.18 Some scans of the Ag NP-modified Pt electrode in 0.1 M NaOH + 0.1 M GlyOH, v = 50 mV s^{-1}. Pt ⌀ = 25 µm.

Selected scans of the modified electrode are shown in Figure 3.18, where it is evident that no Ag-specific electrochemistry contributes to the voltammogram, even in the early scans. The same recovery of Pt features in the presence of glycerol was observed as in the NaOH system, consistent with the hypothesis that silver and thiol species are

partially removed upon continuous potential cycling, leaving a CV dominated by Pt features, but not being an exact match to the CV of the unmodified electrode.

3.3.3 Discussion

Without additional insights, such as those provided by XPS or STM for this system, there is no direct evidence confirming the deposition of Ag NPs onto the Pt electrode. While it is assumed that the same immersion protocol used to modify the Au substrate was equally effective here, the success of the deposition cannot be definitively confirmed. This uncertainty must be taken into consideration when interpreting the electrochemical data for the system.

Electrochemical measurements in 0.1 M NaOH revealed a suppression of current density in the voltammogram compared to the unmodified Pt electrode, along with a pronounced feature in the Pt oxide formation peak occurring at potentials where Ag oxide formation is typically observed in the same electrolyte. This peak diminished in intensity with continued cycling as Pt voltammogram features were recovered, though it remained evident even in the final scan of the modified electrode. In the presence of 0.1 M glycerol, no definitive contribution from Ag-specific electrochemistry was observed. The primary observation was a suppression of current densities in the voltammogram, which did not fully recover to the levels seen for a clean, unmodified Pt electrode. However, the voltammetric features exclusively reflected Pt-specific electrochemistry, with current density increasing progressively with continued potential cycling.

In considering the electrochemical behaviour of Ag NPs on Pt, two scenarios must be acknowledged, as discussed previously for the Ag–Au system. If free thiols remain in the sample, they may contribute to the suppression of current density observed in the initial

scans. However, unlike on Au substrates, the suppression is less pronounced, which could reflect the weaker affinity of Pt–S binding compared to Au–S, or simply differences in the extent of thiol adsorption. Regardless, Pt-specific features emerge as the potential is cycled, suggesting partial recovery of the electrode surface. The only feature that could be linked to Ag is the delayed onset of the oxidation peak in the first scan of the modified Pt electrode in 0.1 M NaOH (Figure 3.15, 3.16), which remains more pronounced than that of a clean Pt electrode. This effect could indicate the presence of Ag on the surface, but it could equally arise from the influence of free thiols, and distinguishing between the two requires further investigation. In the presence of glycerol, the same behaviour is observed: suppressed current densities followed by recovery upon cycling. In this case, however, no Ag-specific electrochemical features were detected. Without complementary STM or XPS data, we cannot confirm the successful immobilisation of Ag NPs, nor can we determine whether the observed voltammetric changes are attributable to Ag itself or to residual thiols. This uncertainty makes it difficult to draw firm conclusions regarding entropic and enthalpic driving forces in this system. In both NaOH and glycerol electrolytes, the voltammograms suggest that a species remains on the Pt surface, as the current densities do not fully recover to those of a clean electrode. This could reflect Ag that is not fully removed by potential cycling and dissolution, or another contaminant such as excess thiol.

With the view that Ag NP are present on the Pt electrode, electrochemical characterisation of Pt-Ag alloys by Xu *et al*. demonstrated a similar behaviour, where the initial CV scan exhibited a pronounced anodic peak attributed to the formation of Pt and Ag oxides, consistent with our observations in the first scan of the modified Pt electrode in 0.1 M NaOH.[37] Xu *et al*. also reported that this feature diminished upon potential

cycling, with the voltammogram recovering more Pt-like features. However, in our system, Ag-specific electrochemistry remains evident even in the final scan.

Assuming the deposition of the Ag NPs was successful, thiol redistribution from Ag to Pt could account for the lower current responses observed for the modified electrode. Given that the Pt-S bond is stronger than the Ag-S bond, enthalpic considerations suggest that thiol redistribution onto the Pt surface should occur, leaving the exposed Ag cores unprotected on the Pt substrate.[1,2] Evidence of this is seen in the emergence of a new voltammetric feature in 0.1 M NaOH, but not in the presence of glycerol. This suggests that while some electrochemically active Ag may be present on the surface, the surface coverage is too low to produce more pronounced differences than those observed. Furthermore, the fact that Ag-specific electrochemistry in 0.1 M NaOH occurs in the same potential region as expected for a clean Ag electrode indicates that the Ag NPs behave similarly to bulk Ag on the Pt surface.

These observations align with the known miscibility gap between bulk Pt and Ag.[14] While Pt-Ag alloys can be synthesised at the nanoscale, their stability is highly dependent on factors such as the metal ratio and the size of the bimetallic particles.[11] In the present system, where one metal exists in bulk and the other at the nanoscale, there is no evidence of alloying between the two metals. The observed voltammetric features can be independently assigned to Pt and Ag, suggesting that the two metals retain their distinct electrochemical behaviours.

3.4 Conclusion

The aim of this chapter was to evaluate the stability and structural evolution of Ag nanoparticles on Au and Pt substrates.

For Ag NPs on Au, it was shown that their immobilisation leads to the formation of Ag islands on the substrate. These islands consisted of monoatomic features corresponding to individual particles, as well as regions where islands appear to have agglomerated. XPS analysis revealed that thiol binding on the modified substrate was distinct from that observed on either the Au substrate or the Ag particles, indicating a difference in the system compared to the metals individually. Additionally, the formation of silver oxide was confirmed, potentially further driving the migration of thiols. The shift in thiol binding energies suggested that the metals were not in the same chemical state as before deposition, and given the known alloying behaviour of Au and Ag, the possibility of alloy formation was considered.

Electrochemical investigations in alkaline media and in the presence of glycerol showed that the electrode was initially passivated by thiols, exhibiting very low current densities. Expanding the potential window into more negative regions uncovered features attributed to both Au and Ag individually, as well as features not corresponding to the electrochemical behaviour of clean electrodes of either metal. This provided further evidence of interactions between Au and Ag, influencing the electrochemical properties of the modified substrate. The emergence of Ag features in the voltammetry also confirmed the disintegration of the Ag NP thiol shell, consistent with initial expectations. Both entropic and enthalpic factors favoured thiol migration, due to the stronger Au-S

bond and the greater number of binding sites on the Au substrate, leaving the Ag core exposed and resulting in its decomposition, as observed in STM images.

Interestingly, the evidence of alloying behaviour implies that the miscibility of Au and Ag, observed when both metals are at bulk or nanoscale, persists even when the two are in different size regimes. Future work could employ in situ high resolution STM imaging to monitor NP core evolution over time, as well as shedding light on the thiol domains that result from the disintegration of the particles. Additionally, increasing the surface coverage of Ag NPs could help determine whether higher Ag content leads to more pronounced alloy effects in the surface properties.

For Pt surface modification with Ag NPs, the electrochemical data indicated that Ag remains electrochemically active after deposition, as evidenced by the influence on the voltammograms in alkaline media, in regions where Ag-specific features are expected. This aligns with initial expectations, as the stronger Pt-S bond and the larger Pt surface area favour thiol migration onto Pt. The modified surface's electrochemistry reflected that Pt and Ag retained properties similar to their bulk counterparts, with no alloy behaviour or metal mixing observed. This was again consistent with expectations, given the large miscibility gap between Pt and Ag, which typically prevents alloying.

Further characterisation using high-resolution STM and XPS would provide direct evidence of the successful immobilisation of Ag NPs on the surface and offer valuable insights into the resultant structures of the Ag cores upon exposure. Additionally, these techniques could confirm the preferential binding of thiols to Pt and more thoroughly reveal the structural and chemical transformations occurring in this system.

It must also be acknowledged that the electrochemical behaviour observed in both systems may be influenced by the presence of excess thiols in the nanoparticle solutions. Although initial attempts were made to characterise the supernatant after nanoparticle cleaning, thiol–thiol interactions may have limited detection, and therefore the possible contribution of free thiols cannot be fully excluded. This introduces an alternative interpretation of the suppressed current densities and voltammetric features observed, which may arise not only from thiol migration and nanoparticle decomposition but also from thiol adsorption from solution. To resolve this ambiguity, future work should include direct characterisation of the nanoparticle solutions, as well as electrochemical measurements on electrodes modified with thiols alone to decouple the effects of free thiols from those of nanoparticles. In addition, detailed STM and XPS studies, particularly for the Ag–Pt system where these data are currently lacking, would provide crucial confirmation of nanoparticle deposition and enable a more comprehensive understanding of the structural and chemical transformations occurring on these surfaces.

3.5 References

1 D. Y. Petrovykh, H. Kimura-Suda, A. Opdahl, L. J. Richter, M. J. Tarlov and L. J. Whitman, *Langmuir*, 2006, **22**, 2578–2587.

2 D. R. Lide, *CRC Handbook of Chemistry and Physics, 85th Edition*, Taylor & Francis, 2004.

3 E. Pensa and T. Albrecht, *J. Phys. Chem. Lett.*, 2018, **9**, 57–62.

4 P. Carro, E. Pensa, T. Albrecht and R. C. Salvarezza, *J. Phys. Chem. C*, 2020, **124**, 5452–5459.

5 P. Carro, L. M. Azofra, T. Albrecht, R. C. Salvarezza and E. Pensa, *Chem. Mater.*, 2021, **33**, 3428–3435.

6 G. Guisbiers, R. Mendoza-Cruz, L. Bazán-Díaz, J. J. Velázquez-Salazar, R. Mendoza-Perez, J. A. Robledo-Torres, J.-L. Rodriguez-Lopez, J. M. Montejano-Carrizales, R. L. Whetten and M. José-Yacamán, *ACS Nano*, 2016, **10**, 188–198.

7 J.-M. Song, W.-T. Chen, K.-H. Hsieh, T.-H. Kao, I.-G. Chen, S.-J. Chiu and H.-Y. Lee, *Nanoscale Res. Lett.*, 2014, **9**, 438.

8 V. Grasmik, C. Rurainsky, K. Loza, M. V Evers, O. Prymak, M. Heggen, K. Tschulik and M. Epple, *Chem. – A Eur. J.*, 2018, **24**, 9051–9060.

9 A. G. Garcia, P. P. Lopes, J. F. Gomes, C. Pires, E. B. Ferreira, R. G. M. Lucena, L. H. S. Gasparotto and G. Tremiliosi-Filho, *New J. Chem.*, 2014, **38**, 2865–2873.

10 Z. Peng and H. Yang, *J. Solid State Chem.*, 2008, **181**, 1546–1551.

11 J. Wisniewska, H. Guesmi, M. Ziolek and F. Tielens, *J. Alloys Compd.*, 2019, **770**, 934–941.

12 K. Mariandry, R. Kokate, S. V Somerville, L. Gloag, S. Cheong, L. R. Carroll, P. V Kumar, J. J. Gooding and R. D. Tilley, *Chem. Mater.*, 2023, **35**, 8636–8644.

13 T. Hu, Y. Fan, Y. Ye, Y. Cai, J. Liu, Y. Ma, P. Li and C. Liang, *Catalysts*, 2023, 13.

14 K. A. Kane, A. C. Reber, S. N. Khanna and M. F. Bertino, *Prog. Nat. Sci. Mater. Int.*, 2018, **28**, 456–463.

15 A. Andrieux-Ledier, B. Tremblay and A. Courty, *Langmuir*, 2013, **29**, 13140–13145.

16 A. I. Yanson, P. V Antonov, Y. I. Yanson and M. T. M. Koper, *Electrochim. Acta*, 2013, **110**, 796–800.

17 A. Resta, T. Leoni, C. Barth, A. Ranguis, C. Becker, T. Bruhn, P. Vogt and G. Le Lay, *Sci. Rep.*, 2013, **3**, 2399.

18 T. Laiho, J. A. Leiro, M. H. Heinonen, S. S. Mattila and J. Lukkari, *J. Electron Spectros. Relat. Phenomena*, 2005, **142**, 105–112.

19 C. Battocchio, I. Fratoddi, L. Fontana, E. Bodo, F. Porcaro, C. Meneghini, I. Pis, S.

Nappini, S. Mobilio, M. V Russo and G. Polzonetti, *Phys. Chem. Chem. Phys.*, 2014, **16**, 11719–11728.

20 J. V Maya Girón, E. Zelaya, A. Rubert, G. Benítez, P. Carro, R. C. Salvarezza and M. E. Vela, *J. Phys. Chem. C*, 2013, **117**, 24967–24974.

21 C. Battocchio, C. Meneghini, I. Fratoddi, I. Venditti, M. V. Russo, G. Aquilanti, C. Maurizio, F. Bondino, R. Matassa, M. Rossi, S. Mobilio and G. Polzonetti, *J. Phys. Chem. C*, 2012, **116**, 19571–19578.

22 G. Xue, M. Ma, J. Zhang, Y. Lu and K. T. Carron, *J. Colloid Interface Sci.*, 1992, **150**, 1–6.

23 S. W. Gaarenstroom and N. Winograd, *J. Chem. Phys.*, 1977, **67**, 3500–3506.

24 L. D. Burke and P. F. Nugent, *Gold Bull.*, 1997, **30**, 43–53.

25 S. Hebié, T. W. Napporn, C. Morais and K. B. Kokoh, *ChemPhysChem*, 2016, **17**, 1454–1462.

26 S. Chen, B. Wu and C. Cha, *J. Electroanal. Chem.*, 1996, **416**, 53–59.

27 M. López Teijelo, J. R. Vilche and A. J. Arvia, *J. Appl. Electrochem.*, 1988, **18**, 691–698.

28 T. P. Dirkse and D. B. De Vries, *J. Phys. Chem.*, 1959, **63**, 107–110.

29 M. J. Esplandiú, H. Hagenström and D. M. Kolb, *Langmuir*, 2001, **17**, 828–838.

30 N. Y. Suzuki, P. V. B. Santiago, T. S. Galhardo, W. A. Carvalho, J. Souza-Garcia and C. A. Angelucci, *J. Electroanal. Chem.*, 2016, **780**, 391–395.

31 J. Kunze, H.-H. Strehblow and G. Staikov, *Electrochem. commun.*, 2004, **6**, 132–137.

32 J. F. Gomes and G. Tremiliosi-Filho, *Electrocatalysis*, 2011, **2**, 96–105.

33 J. F. Gomes, A. C. Garcia, L. H. S. Gasparotto, N. E. de Souza, E. B. Ferreira, C. Pires and G. Tremiliosi-Filho, *Electrochim. Acta*, 2014, **144**, 361–368.

34 D. Zhan, J. Velmurugan and M. V Mirkin, *J. Am. Chem. Soc.*, 2009, **131**, 14756–14760.

35 P. Daubinger, J. Kieninger, T. Unmüssig and G. A. Urban, *Phys. Chem. Chem. Phys.*, 2014, **16**, 8392–8399.

36 Y. Kwon, Y. Birdja, I. Spanos, P. Rodriguez and M. T. M. Koper, *ACS Catal.*, 2012, **2**, 759–764.

37 J. B. Xu, T. S. Zhao and Z. X. Liang, *J. Phys. Chem. C*, 2008, **112**, 17362–17367.

4. Modification of Gold and Silver Substrates with Platinum Nanoparticles

Chapter Contents

This chapter focuses on the immobilisation of Pt nanoparticles (NPs) onto Au and Ag substrates. Pt NPs immobilised on Au substrates have been shown to exhibit Pt-specific electrochemistry as well as Au electrochemistry, indicating that the Pt particles remain unprotected when immobilised onto Au. This behaviour aligns with expectations, as the Au-S bond is stronger than the Pt-S bond, and the entropic driving force also favours thiol migration.[1,2] The disintegration of the thiol capping layer is therefore anticipated, leaving exposed Pt features. For Pt NPs on Ag substrates, the enthalpic considerations suggest that the Pt-S bond, being stronger than the Ag-S bond, would prevent thiol redistribution, leaving the Pt features protected.[2,3] However, the entropic driving force favours the removal of the thiol capping layer. This study seeks to determine which factor dominates by examining the electrochemical properties of the modified surfaces.

In both systems, the modified substrates are not expected to exhibit evidence of Pt alloying with either Au or Ag. Pt and Au exhibit a miscibility gap at the bulk scale, as do Pt and Ag, though bimetallic particles of Pt with either metal can be synthesised.[4–8] However, it remains unclear how the interactions will differ when one metal is in the bulk state and Pt is at the nanoscale. Differences in surface energy will also influence particle morphology and wetting. Pt has a substantially higher surface energy than both Au and Ag, so Pt is not expected to wet Au or Ag surfaces.[9]

The chapter begins with a discussion of the synthesis of Pt NPs via cathodic corrosion, followed by their immobilisation onto Au and Ag substrates. The modified substrates were then characterised using STM, XPS, and cyclic voltammetry in 0.1 M NaOH and in the presence of 0.1 M glycerol.

4.1 Nanoparticle Synthesis and Characterisation

The synthesis of Pt nanoparticles for Au and Ag surface modifications was conducted using the cathodic corrosion technique outlined in 2. Materials and Methods. The particles discussed in this subchapter were synthesised using setup B (GAMRY potentiostat, GAMRY VFP software) and their size distributions were characterised via TEM imaging.

Various synthesis parameters were tested to produce Pt particle dispersions, and two sample sets were characterised via TEM. The particles were cleaned and deposited onto TEM grids for imaging immediately after synthesis and before the thiol addition step.

Table 4.1 Synthesis parameters for platinum nanoparticles.

Parameter Set	Electrolyte	Amp. (V)	Offset (V)	Freq. (Hz)	CE	Observations
Pt_1	0.5 M NaOH	±2	-2	100	Pt	Grey/black suspension of particles. Etch times consistently approx. 7 mins.
Pt_2	0.5 M NaOH	±3	-3	100	Pt	Substantial amount of gas evolution observed at the WE, accompanied by a black/grey suspension of particles. Etch times fluctuated between cycles within the same experiment, ranging from 1.5 to 5 minutes.

Both the Pt_1 and Pt_2 synthesis parameters produced a suspension of Pt particles; however, the time required for Pt corrosion using the Pt_2 parameters varied across different synthesis cycles within the same experiment. This inconsistency was observed across several samples produced under this parameter set, suggesting that the current passing through the wire was not consistent across synthesis cycles. As demonstrated

by Koper *et al.*, the current density across the wire is directly related to the size of the Pt nanoparticles produced.[10] Therefore, the fluctuating etch times across multiple cycles suggest a possible cycle-to-cycle variation in the size of the particles produced using this set of parameters. In contrast, the synthesis parameters for sample Pt_1 consistently yielded the same approximate etch time for each synthesis cycle across multiple samples. This consistency suggested that these parameters were more reliable and are likely to produce a narrower size distribution than Pt_2.

The TEM images of Pt particles produced using parameter set Pt_1 are presented in Figure 4.1. The images, taken at various magnifications, reveal large clusters of Pt, though individual particles are visible at the edges of these clusters. Where individual NPs were discernible, their diameters were measured, with the particle size distribution revealing an average diameter of 3.02 ± 0.34 nm. The presence of smaller particle structures around the larger clusters suggests that individual Pt particles tend to agglomerate into larger structures. This agglomeration is likely due to solvent evaporation during the drying of the TEM grid, and the absence of a capping agent.

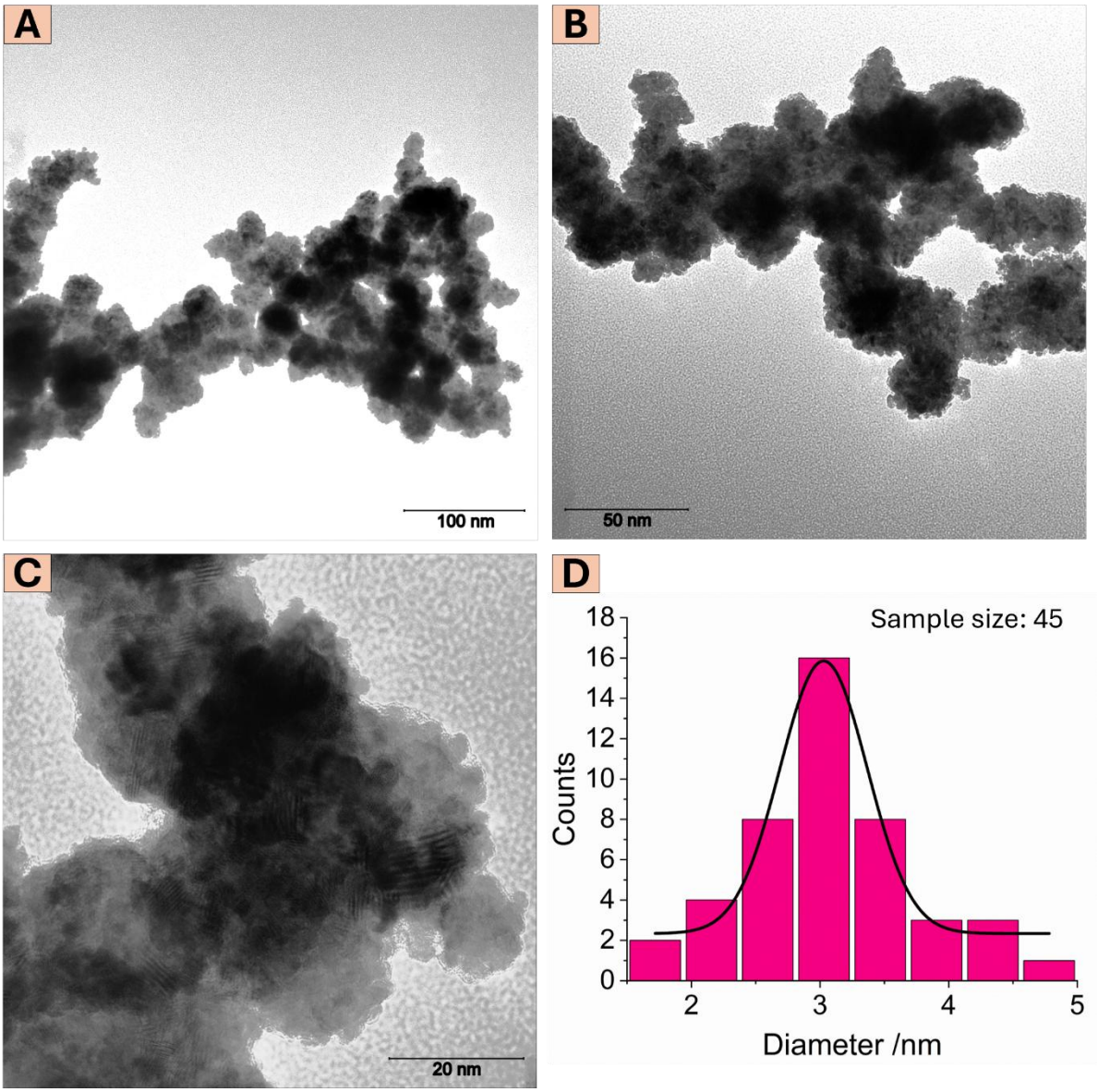

Figure 4.1 TEM images of Pt_1 nanoparticles at accelerating voltages of (A) 100 kV, (B) 200 kV and (C) 600 kV. (D) Particle size distribution analysis.

Figure 4.2 shows the particles produced using parameter set Pt_2. Similar to the particles in Fig. 4.1, there are large areas of particle agglomeration. Individual particles are visible at the edges of these structures as well as in some regions between the larger clusters (Figure 4.2 (B, C)).

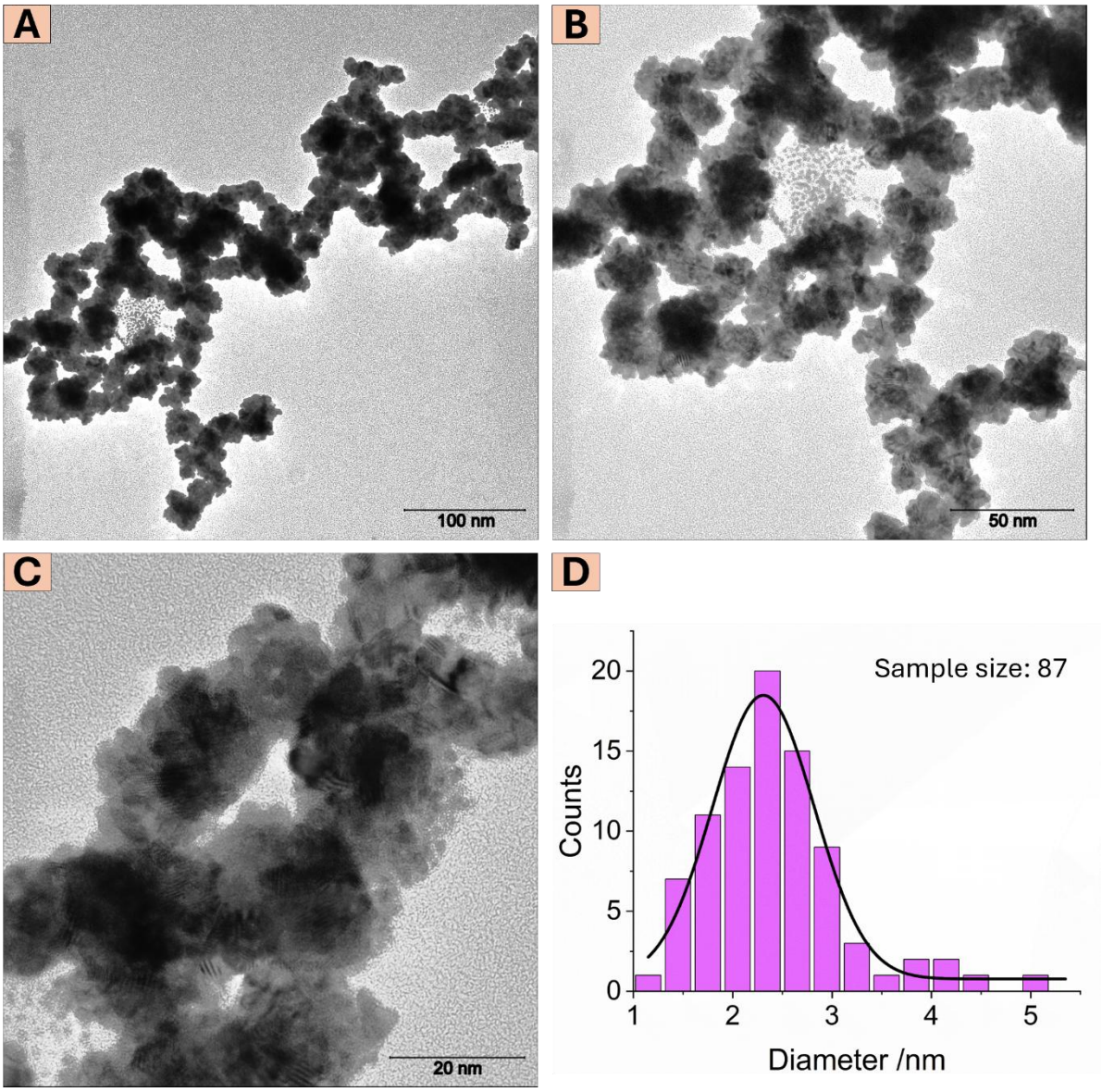

Figure 4.2 TEM images of Pt_2 nanoparticles at accelerating voltages of (A) 100 kV, (B) 200 kV and (C) 600 kV. (D) Particle size distribution analysis.

Size distribution analysis of the Pt_2 particles revealed a mean diameter of 2.31 ± 0.51 nm. Koper *et al*. demonstrated that an increase in current density results in larger Pt nanoparticle sizes, although their measurements were conducted at significantly higher electrolyte concentrations (5 M vs 0.5 M).[10] In this study, however, it was observed that particles synthesised using the Pt_2 parameter set were smaller in average diameter than

those made using Pt_1, despite the larger amplitude and consequently higher current density in the Pt_2 system.

This discrepancy can be explained by the greater variation in the size of the Pt_2 particles, which is likely due to differences in etch times across synthesis cycles. It is possible that cycles in the Pt_2 parameter set with etch times similar to or longer than those of Pt_1 produce smaller nanoparticles, while shorter etch times result in larger particles. This aligns with the expectation that increasing the applied amplitude—and therefore the current density and etch time—leads to the formation of larger particles, a trend also observed in the synthesis of Ag particles (see chapter 3. Modification of Gold and Platinum Substrates with Silver Nanoparticles).

To eliminate this uncertainty around reliable etch times within the same synthesis experiment, it was decided that the Pt NPs used for surface modifications would be those produced using the Pt_1 parameters. This ensured that the particles used were reproducible and that the TEM characterisation was representative of the sample.

As with previous chapters, excess thiol in the nanoparticle solution cannot be definitively ruled out. As such, the possible presence of unbound thiols should be considered when interpreting the electrochemical data presented later in this chapter.

4.2 Modification of Gold Substrates

This subchapter focuses on the characterisation of Au (111) substrates modified with Pt NPs via overnight immersion in a solution of thiolated Pt NPs, as described in 2.3.4 Modification of Metal Substrates with Nanoparticles. As was the protocol with Ag NPs in Chapter 3, the characterisation of the modified substrates was conducted using STM, XPS, and cyclic voltammetry, with the goal being to evaluate the stability of the Pt nanoparticles on the Au substrate via characterisation of the modified surface.

4.2.1 STM of Pt NPs on Au (111)

Pt NPs were immobilised onto an Au (111) substrate via overnight immersion and characterised via STM, with the aim to gain insight into the topography of any features that may form on the substrate as a result of the Pt-Au interaction. An STM image, as well as height and diameter distributions are presented in Figure 4.3.

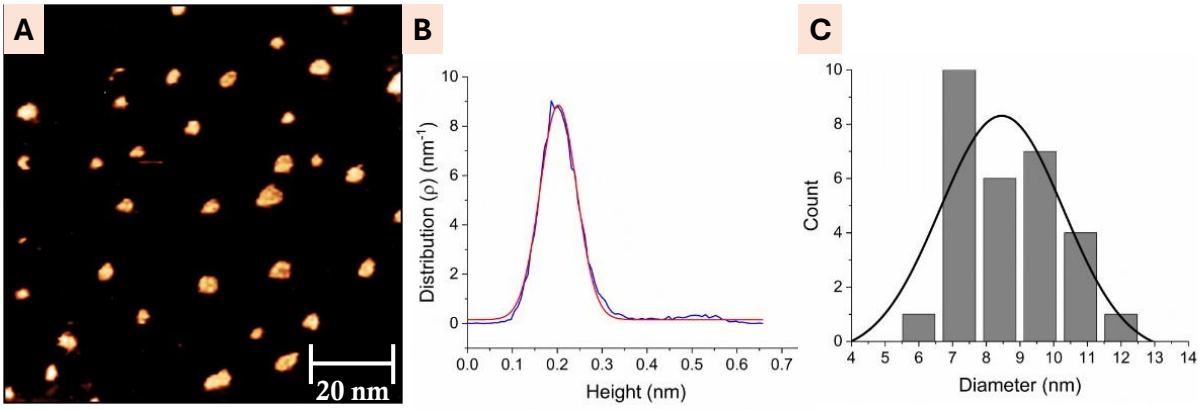

Figure 4.3 (A) STM image of Pt nanoparticles on an Au (111) substrate, and the size distributions of the (B) diameter (width) and (C) height of the nanoparticles.

Figure 4.3 (A) presents an STM image of the Pt NP-Au (111) substrate, where a non-uniform distribution of features is observed. The features had an average height of 0.203

± 0.004 nm. Given that the height of monoatomic Pt (111) steps is typically 0.238 nm, it is reasonable to conclude that we are observing monoatomic Pt islands across the Au substrate.[11] This is in line with the lateral spread of the features, as the average diameter is calculated as 8.46 ± 1.8 nm, which is significantly larger than the diameter of individual particles measured via TEM imaging.

As previously discussed, if the NPs undergo a thiol redistribution effect, one would expect the unstable Pt cores to disintegrate, resulting in both a lateral spread and a height close to that of a monoatomic step, in the cases of full disintegration. Although it is challenging to determine precisely how many Pt NPs contribute to the formation of a single island feature, the observed data of both the average height and diameter values allow us to infer that we are indeed observing the disintegration of Pt NPs upon their immobilisation onto an Au substrate, despite the higher cohesive and surface energies of Pt.

Further characterisation was necessary to confirm whether the observed effect occurs in relation to a thiol redistribution. To investigate this, XPS characterisation was employed to determine the ratio of thiols bound to the nanoparticles versus the substrate. By analysing the extent of thiol redistribution—whether it involved full or partial migration of thiols onto the Au substrate—XPS provided valuable insight into the composition of the modified surface.

4.2.2 XPS of Pt NPs on Au (111)

XPS elemental analysis was performed on an Au (111) substrate modified with Pt NPs. To accurately determine the binding energy (BE) values of the metal-thiol interactions, some control measurements were conducted. Firstly, 1-hexanethiol (HT) was deposited on a clean Pt (111) substrate to establish the S-Pt BE, and separately on a clean Au (111) substrate to identify the S-Au BE. Next, Pt NPs were deposited on HOPG to determine the S-Pt NP binding energy. Finally, Pt NPs were deposited on an Au substrate to investigate whether the sulfur preferentially binds to the Pt NPs or redistributes to the Au substrate. These comparisons are essential for understanding how the thiol capping layer interacts with the underlying metallic surfaces and whether it favours binding to the nanoparticles or the substrate.

The XPS spectra for the Au (111) substrate modified with Pt NPs are presented in Figure 4.4. The BE values extracted from these spectra, along with the corresponding relative contributions (RC) of each BE to the overall XPS spectrum, are summarised in Table 4.2.

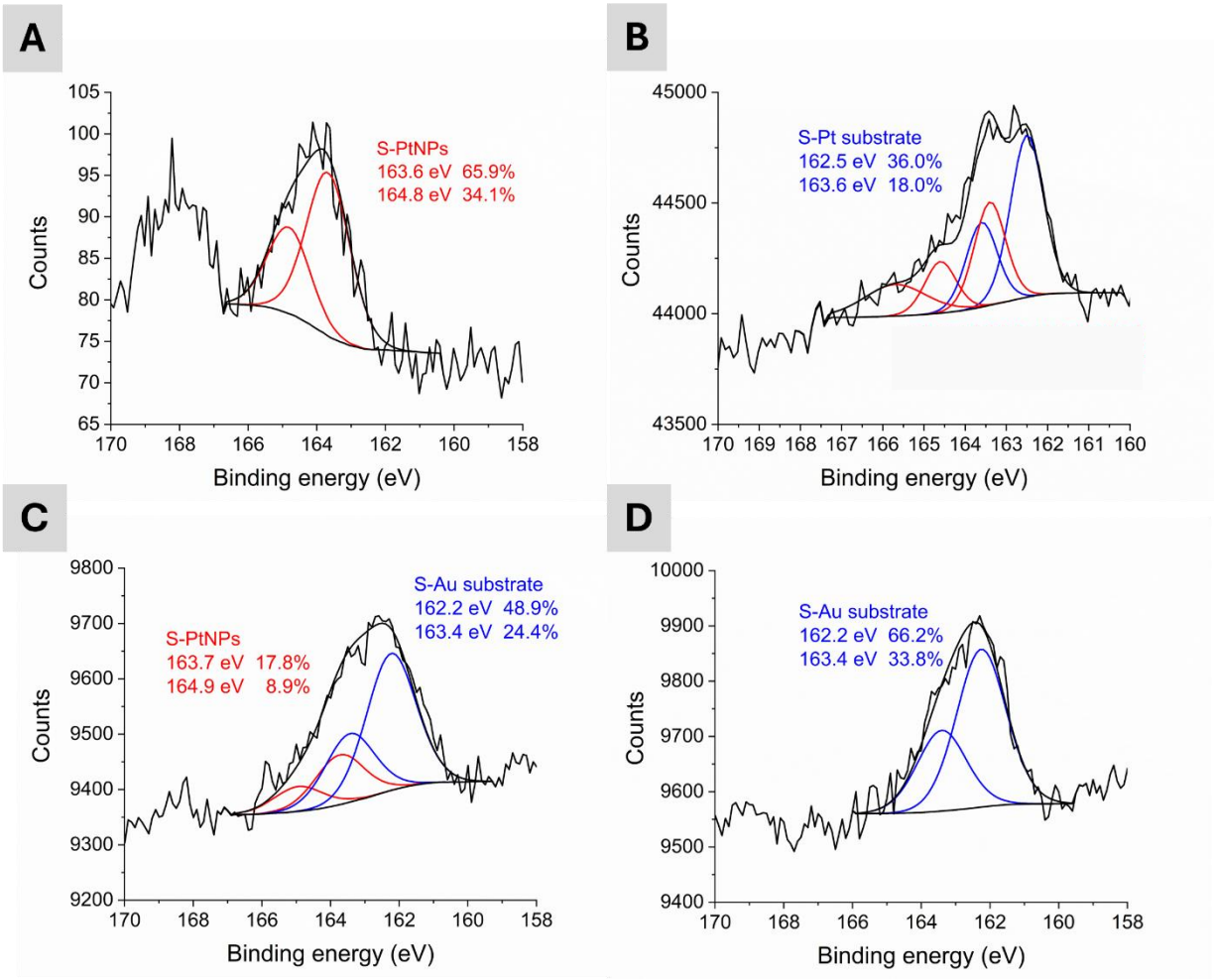

Figure 4.4 XPS of (A) Pt NPs NPs drop-cast onto HOPG, (B) a 1-hexanethiol SAM on a Pt (111) substrate, (C) Pt NPs immobilised onto an Au (111) substrate via immersion and (D) a SAM of 1-hexanethiol on Au (111).

In Table 4.2, experiment 1 corresponds to HT adsorbed on a Pt (111) surface, with BE values of 162.5 eV and 163.6 eV contributing 36% and 18%, respectively, to the overall XPS spectrum. These results are consistent with literature values of 162.6 and 163.6 eV, which attributed the lower BE component to sulfur bound directly to the Pt surface, whereas the higher BE component has been linked to unbound thiols trapped or physi-sorbed in the monolayer.[2,12] This signal could originate from either surface-bound thiols or residual free thiol in the system. However, the simultaneous observation of Pt island formation via STM suggests that particle attachment still occurs in the presence of thiol

species. The role of any excess thiol in facilitating this attachment remains unclear and warrants further investigation.

Table 4.2 Summary of the measured BE values and their relative contributions (RC) in XPS spectra of measurements on the Pt NPs-Au substrate system. Surface modification via immersion was used for all experiments.

Experiment		S2*p* Signal			
		BE (eV)	RC	BE (eV)	RC
1	HT on Pt (111)	162.5	36%	163.6	18%
2	HT on Au (111)	162.2	66.2%	163.4	33.8%
3	Pt NPs on HOPG	163.6	65.9%	164.8	34.1%
4	Pt NPs on Au (111)	163.7	17.8%	164.9	8.9%
		162.2	48.9%	163.4	24.4%

Experiment 2 measured 1-hexanethiol on an Au (111) surface, resulting in BE values of 162.2 eV (66.2%) and 163.4 eV (33.8%). These are again consistent with literature values, where BE values around 162 eV are assigned to the Au-thiol bond, and values between 163-164 eV correspond to unbound thiol species.[2,13]

Experiment 3, Pt NPs on HOPG, yielded BE values of 163.6 eV (65.9%) and 164.8 eV (34.1%). The lower BE value was assigned to the physisorption of thiol, while the higher BE value was attributed to the S-Pt NP interaction, consistent with observed values for binding between sulfur and Pt nanoparticles.[14]

In Experiment 4, the Au (111) surface modified by immersion in Pt NPs showed similar values of 163.7 eV and 164.9 eV, contributing 26.7% to the overall spectrum, indicating that S-Pt NP binding is present in the modified system. The other measured BEs in experiment 4 gave values of 162.2 eV and 163.4 eV, which correspond to S-Au binding – as seen in experiment 2 - with a total contribution of 73.3%, confirming sulfur is also bound to the Au substrate.

These results indicate that the majority of the thiol has redistributed from the Pt NPs to the Au substrate, as evidenced by the 73.3% contribution of the S-Au binding energies. This observation is in agreement with the STM imaging results, which provides evidence for the formation of monoatomic Pt islands with an average height of 0.203 ± 0.004 nm on the surface. The exposure of the Pt suggests that the NP cores became unstable, likely triggering the formation of these island features. It is possible that some thiols remain attached to the island structures, and may not have been captured with the STM resolution.

The combined XPS and STM results suggest that the thiols partially redistribute from the Pt NPs onto the Au substrate, leading to disintegration of the Pt cores into monoatomic islands. Next, electrochemical studies were performed on the modified Au electrode in alkaline media to determine the electrochemical features of the modified surface and assess whether the exposed Pt islands would contribute Pt-specific electrochemical behaviour to the system.

4.2.3 Electrochemistry of Pt NPs on Au in 0.1 M NaOH

At this stage, the XPS results confirmed that thiols partially redistribute from the Pt NPs onto the Au substrate, indicating that the Pt sits exposed atop the Au surface, though some thiol-Pt NP binding remains. To investigate whether the exposed Pt contributes to the electrochemical properties of the modified surface, cyclic voltammetry was performed in 0.1 M NaOH. The resulting voltammogram was analysed to determine whether it displayed characteristic features of Au, both Au and Pt, or neither metal. If only Au features were observed, it would suggest that the exposed Pt is not electrochemically active. Conversely, if both Au and Pt features appeared, *i.e.,* voltammetric features similar to those of bulk Au and Pt electrodes, it would indicate that both metals are electrochemically active. However, if the voltammogram showed features distinct from either metal, as seen previously in the Ag-Au system (see chapter 3.2), it would suggest an interaction between the metals, resulting in a new electrochemical behaviour unique to the modified surface.

Figure 4.5 shows the voltammograms of a clean Au electrode, a clean Pt electrode, and the modified Au electrode with Pt NPs (via overnight immersion) in 0.1 M NaOH, comparing the first and final scans. The clean electrodes (Au and Pt) exhibit their characteristic cyclic voltammograms (CVs). For the Au electrode, Au oxide formation is indicated by an oxidation peak (peak A) between 1.09 and 1.51 V_{RHE}, while the reduction of the oxide layer is marked by a peak at 0.92 V_{RHE} (peak B) in the cathodic scan.[15,16] The Pt electrode displays typical features reported in literature. In the anodic sweep, hydrogen desorption occurs at 0.13 and 0.25 V_{RHE}, corresponding to Pt (110) and (100) sites, respectively (peaks C, C'). During the cathodic sweep, hydrogen adsorption is seen

at 0.23 and 0.11 V_{RHE} (peaks D,D').[17] Extending the potential further negative would result in hydrogen gas evolution. Oxide formation on Pt starts around 0.41 V_{RHE}, and the reduction of these oxides (peak E) is observed at 0.57 V_{RHE} during the reverse scan.[18]

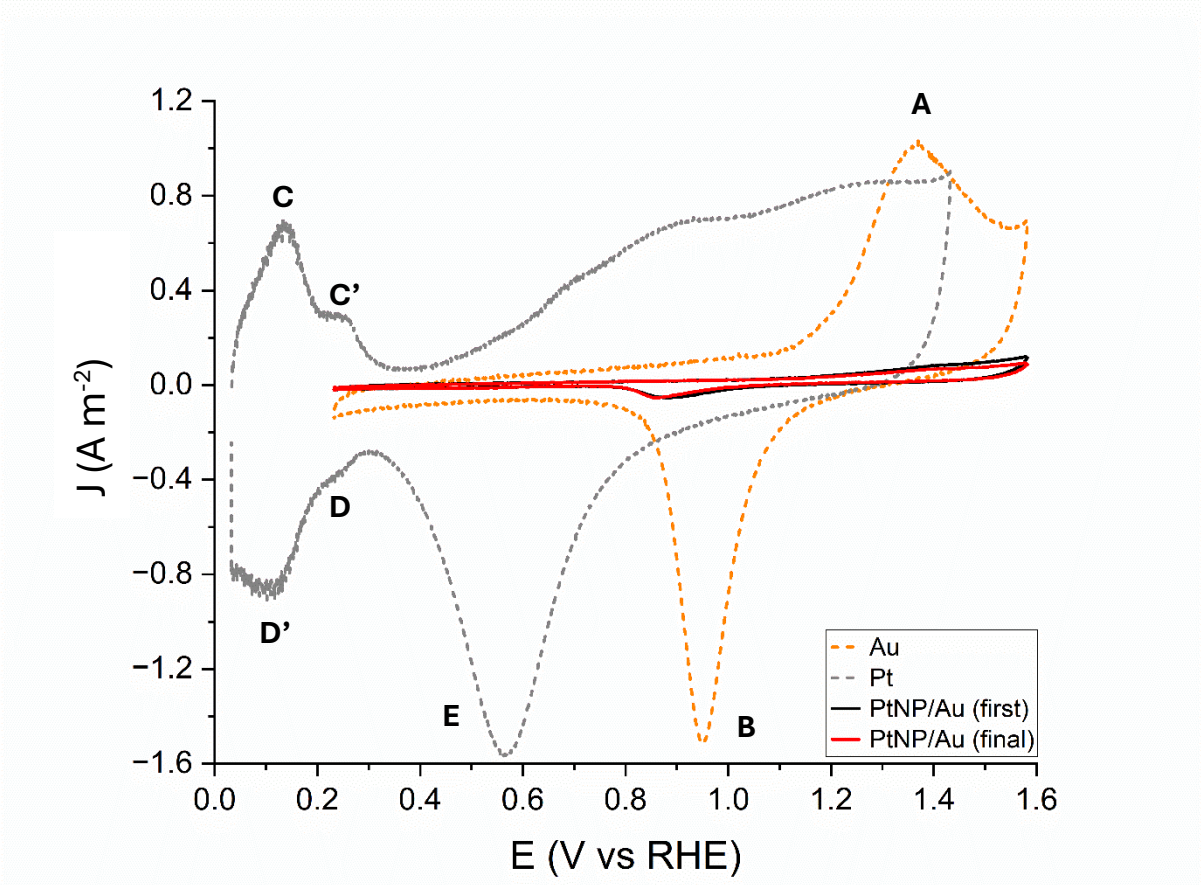

Figure 4.5 The CVs of an unmodified Au electrode (yellow), an unmodified Pt electrode (grey), and the first (black) and final (red) scans of the Au electrode modified with Pt NPs, CVs were recorded in 0.1 M NaOH, v = 50 mV s^{-1}. Au ⌀ = 25 µm, Pt ⌀ = 25 µm. Total number of scans = 7.

For the modified substrate, the first and final scans (Fig. 4.5) show the behaviour of the electrode over a total of seven scans. The primary difference between the voltammogram of the Pt NP-modified Au electrode and the clean Au electrode is the significantly lower current density observed for the modified surface. This decrease could be the result of

thiols on the substrate blocking the current flow, either as a result of the migration effect or due to the presence of excess thiol species in solution.

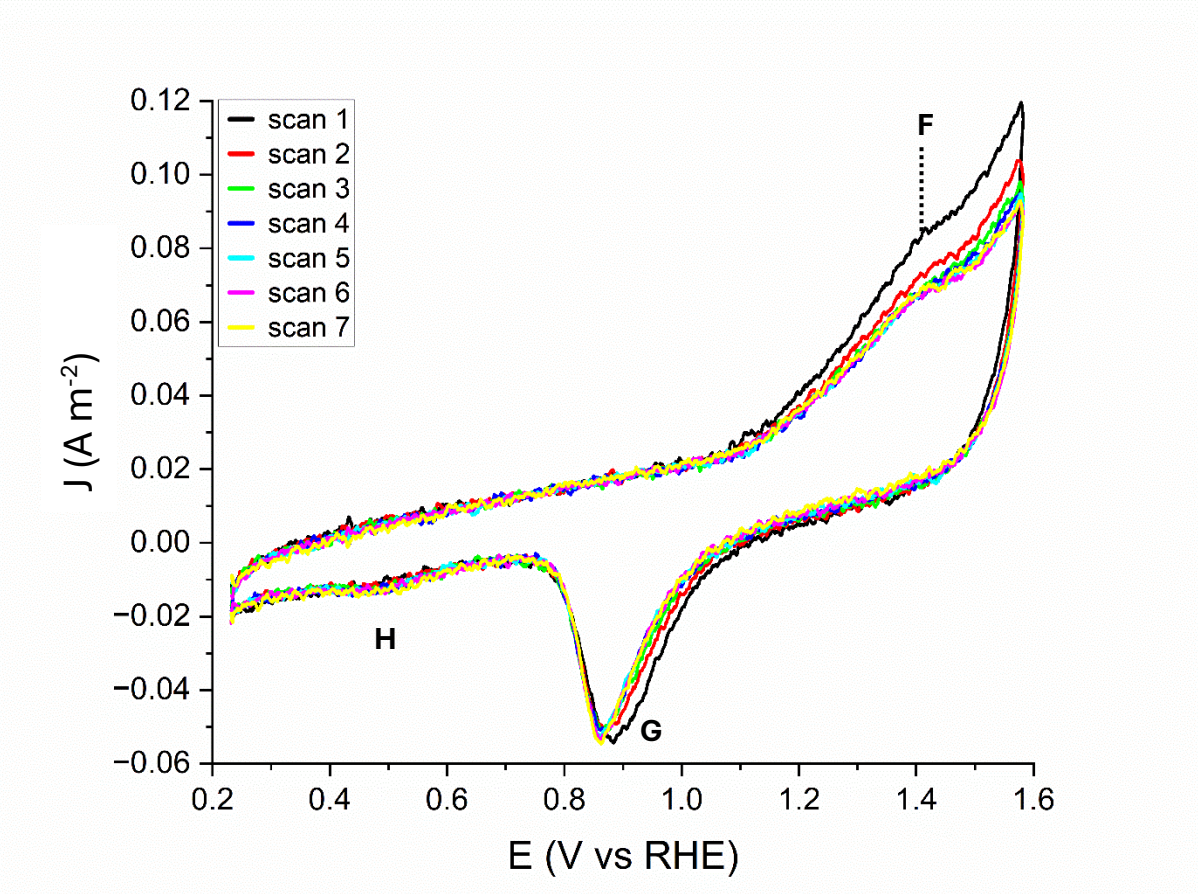

Figure 4.6 All seven CVs measured over the course of an experiment of the Pt-modified Au electrode. CVs were recorded in 0.1 M NaOH, v = 50 mV s^{-1}. Au ⌀ = 25 µm.

Figure 4.6 presents only the voltammograms of the modified electrode. It was observed that the CV remains relatively similar across all seven scans. In the anodic scan, a peak appears at approximately 1.4 V_{RHE} (peak F), while in the cathodic scan, two peaks are visible: one at 0.86 V_{RHE} (peak G) and a smaller one at 0.5 V_{RHE} (peak H). Peak F falls within the range typically associated with oxide formation on both Au and Pt electrodes. However, the peak G does not align with the expected positions for the reduction of these oxides. Instead, it is slightly negatively shifted compared to the oxide reduction peak on

Au and positively shifted relative to the oxide reduction peak on Pt. However, the shift relative to the Au oxide reduction peak is only 60 mV and is not considered significant. Peak H is likely associated with the reduction of oxides on Pt, as it appears within the same potential range as the typical Pt oxide reduction peak.[17,18]

Peak H may therefore indicate the presence of exposed, electrochemically active Pt on the modified surface. The overall CV profile is similar to that observed for an Au electrode modified with Ag NPs in the same potential region. For Ag NPs on Au, an anodic peak at 1.4 V_{RHE} was observed, which shifted slightly to 1.36 V_{RHE} as the potential was cycled, along with a reduction peak at 0.84 V_{RHE}. However, no features appeared between 0.4 and 0.5 V_{RHE}, unlike the reduction peak observed in Figure 4.6. This suggests that while the oxidation peak at 1.4 V_{RHE} and the reduction peak at 0.86 V_{RHE} are primarily due to Au electrochemistry, the oxide formation also includes contributions from Pt oxides, which are reduced at 0.5 V_{RHE}. That said, the current densities are very low, likely due to excess thiols on the electrode surface. To address this, the potential window was expanded to allow for the removal of these thiols via desorption, to see if any additional voltammetric features could be uncovered.

4.2.3.1 Expanded Potential Window

The results, shown in Figure 4.7, reveal a significant difference between the first and final scans of the modified electrode. The final scan indicates that the Au electrode surface is largely recovered, with the voltammogram closely resembling that of the clean Au electrode. Additionally, the reduction peak at 0.5 V_{RHE} in the reverse scan becomes more pronounced, suggesting that the exposed Pt sites are now more electrochemically active.

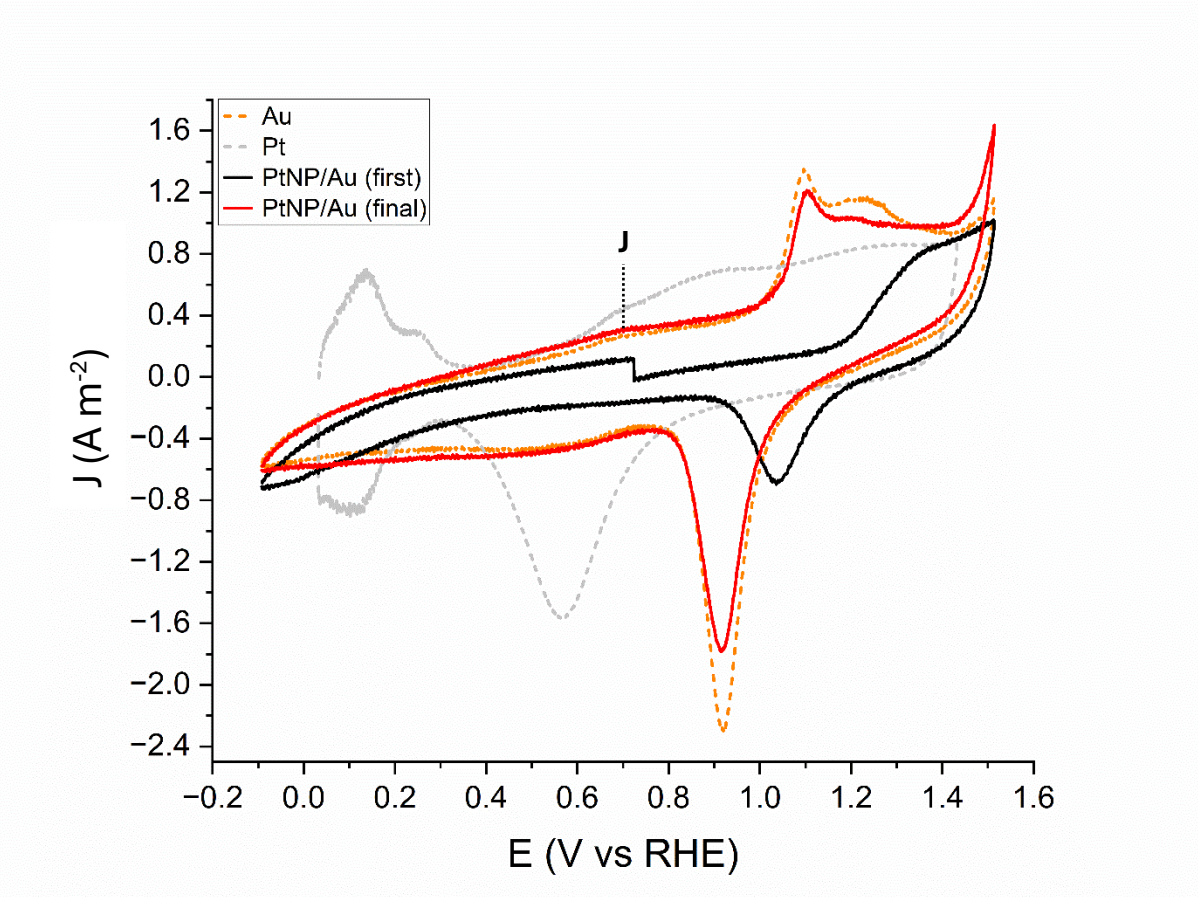

Figure 4.7 The CVs of an unmodified Au electrode (yellow), an unmodified Pt electrode (grey), and the first (black) and final (red) scans of the Au electrode modified with Pt NPs, for an expanded potential window. CVs were recorded in 0.1 M NaOH, v = 50 mV s^{-1}. Au ⌀ = 25 µm, Pt ⌀ = 25 µm. Total number of scans = 20.

After the second scan, the current densities across the voltammogram increase steadily, likely due to the electrode surface being progressively cleaned of thiols. Although no distinct desorption peak is visible, the recovery of the Au voltammetric profile indicates that the bulk Au surface is being gradually restored. As the electrode is cycled, four key features emerge. The oxidation and reduction peaks, with onsets at 1.0 and 1.1 V_{RHE} respectively, increase in current density to levels similar to those observed for a clean Au electrode. In addition, a new oxidation feature appears around 0.7 V_{RHE} (peak J), corresponding to the onset of oxide formation and reduction typically seen on a clean Pt electrode. It is important to consider that the observed initial current suppression could

be attributed to a surface saturated with excess thiols. In this scenario, the potential cycling may gradually remove these blocking species, exposing electrochemically active regions over time. However, this does not exclude the possibility of thiol migration from the Pt NPs to the Au surface, especially given the stronger Au–S bond and higher density of binding sites. The presence of features attributable to Pt emerging upon cycling suggests that the Pt surface is at least partially active, although the hydrogen adsorption and desorption effects typically observed with electrochemically active Pt are not observed.

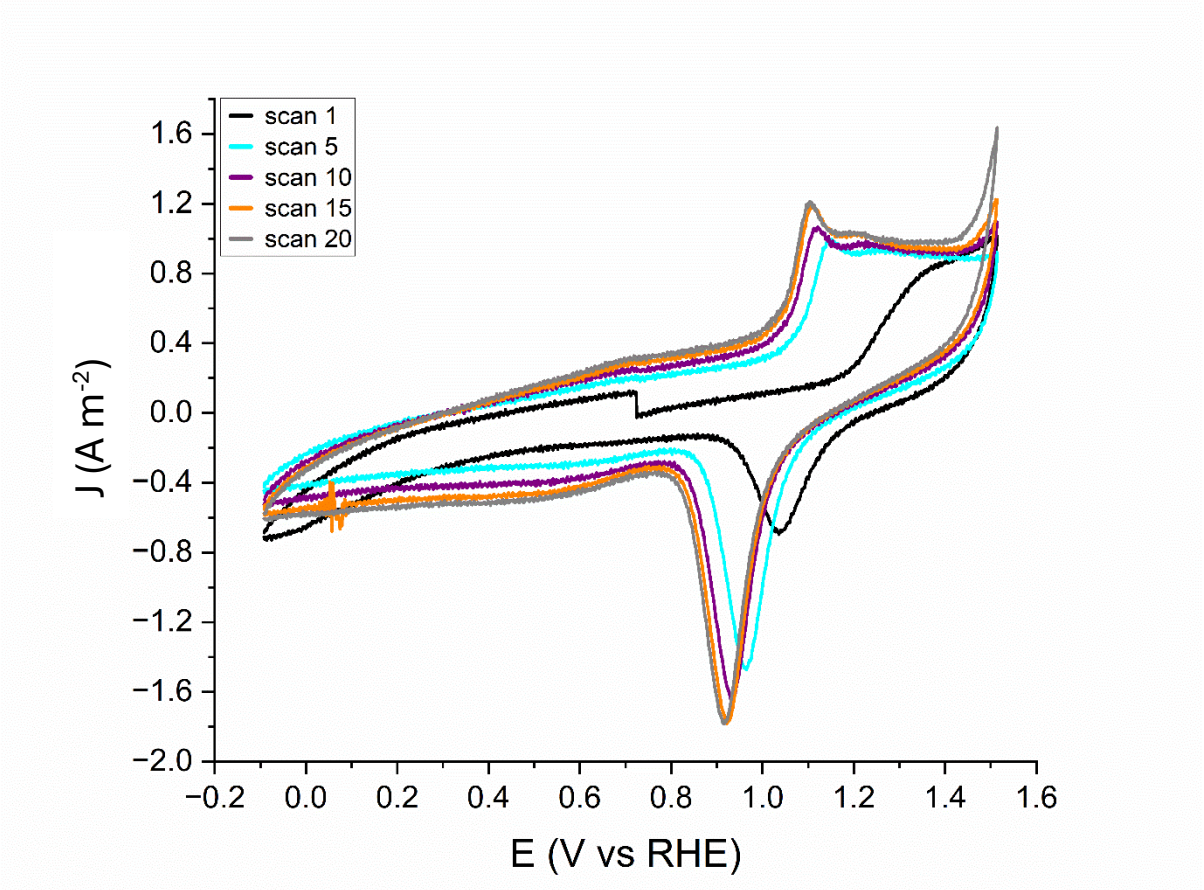

Figure 4.8 Some scans of the Pt-modified Au electrode, for an expanded potential window. CVs were recorded in 0.1 M NaOH, v = 50 mV s^{-1}. Au ⌀ = 25 µm.

One can therefore conclude that in 0.1 M NaOH, some Pt-specific features emerge as the potential is cycled. These features were initially masked, to an extent, in the narrow

potential window, due to the presence of thiols on the electrode surface. Although no distinct thiol desorption peak was observed, potential cycling in the expanded window resulted in a clear increase in current densities. Hence, as the Pt features on the modified surface were cleaned, the Pt became more electrochemically active, displaying oxidation and reduction features consistent with those of a clean Pt electrode. The next step was to investigate the system in the presence of glycerol, as Au and Pt exhibit distinct electrocatalytic peaks for glycerol at potential positions that do not overlap, making it a good probe to further distinguish between the emerging features.

4.2.4 Electrochemistry of Pt NPs on Au in 0.1 M NaOH and 0.1 M Glycerol

Figure 4.9 presents the voltammograms of both Au and Pt electrodes in the presence of 0.1 M glycerol (GlyOH), as well as the first and final scans of the Pt NP modified Au electrode. The clean Au electrode displays a primary oxidation peak at 1.1 V_{RHE} in the anodic scan (peak A) and a secondary oxidation peak at 0.99 V_{RHE} in the cathodic scan (peak B), consistent with values reported in literature.[19]

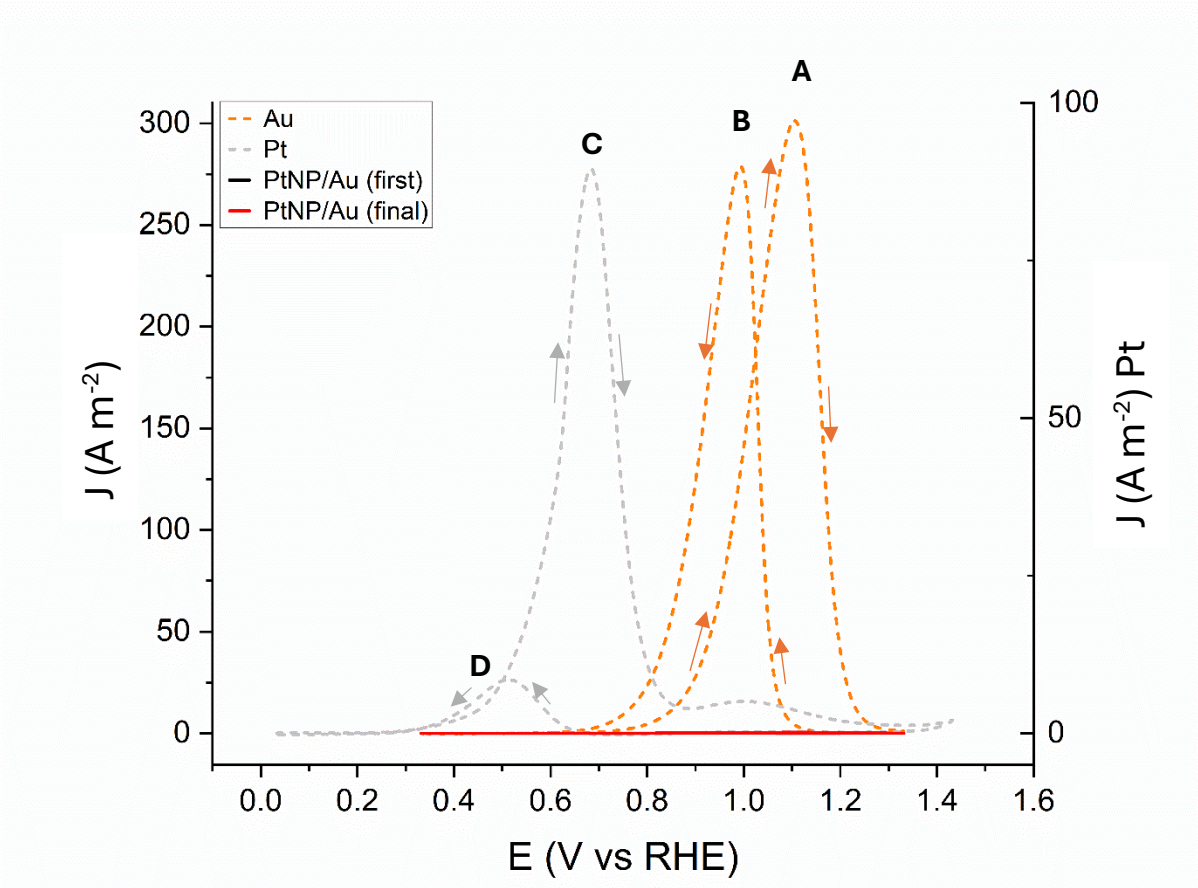

Figure 4.9 CVs of an Au electrode (yellow, left scale), Pt electrode (grey, right scale), and the first (black) and final (red) scans of the Au electrode modified with Pt NPs (left scale). CVs were recorded in 0.1 M NaOH and 0.1 M GlyOH, v = 50 mV s^{-1}. Au ⌀ = 25 µm, Pt ⌀ = 25 µm. Total number of scans = 12.

In comparison, the clean Pt electrode shows oxidation features at 0.68 V_{RHE} in the anodic scan and 0.5 V_{RHE} in the cathodic scan (peaks C and D, respectively), which align with the typical oxidation behaviour of glycerol as reported in literature.[20]

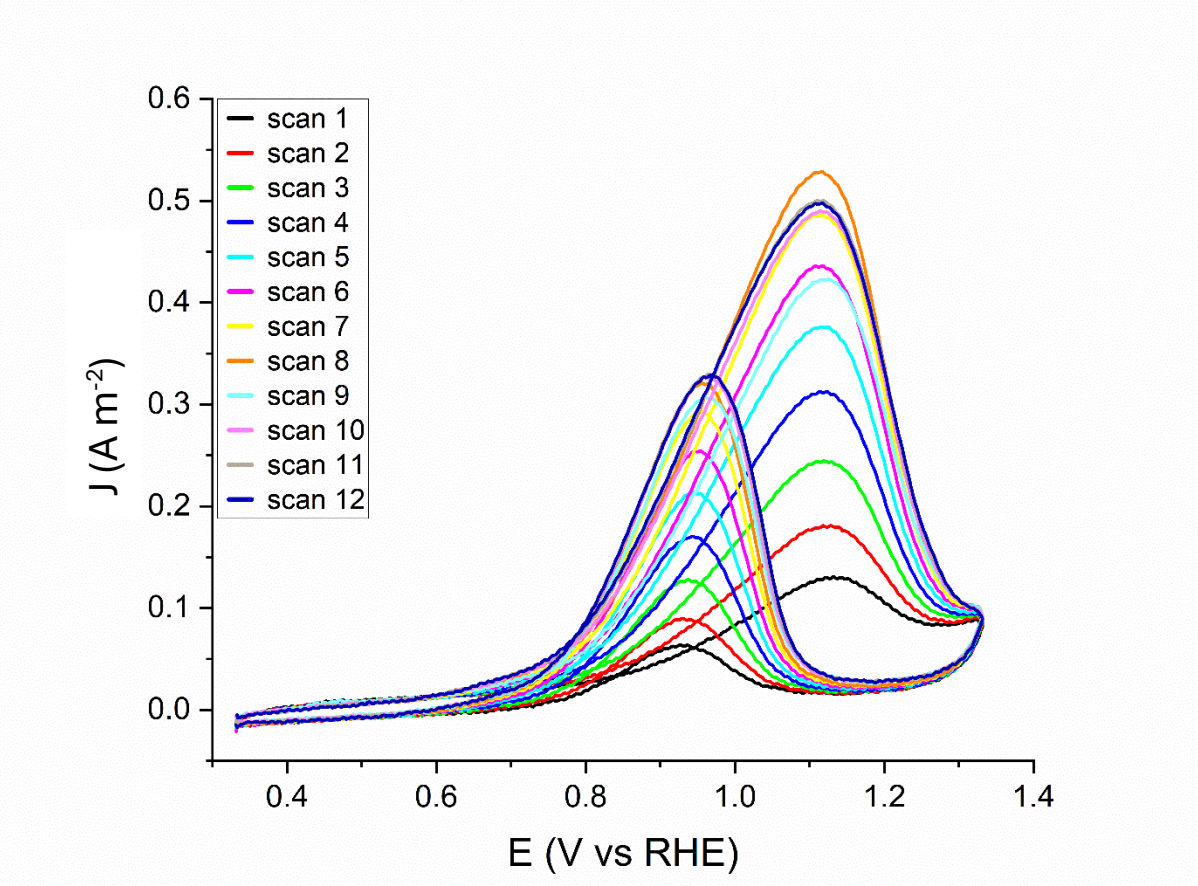

Figure 4.10 All CVs measured of the Pt-modified Au electrode in 0.1 M NaOH + 0.1 M GlyOH, v = 50 mV s^{-1}. Au ⌀ = 25 µm.

For the modified electrode surface, the observed currents are significantly smaller than those of the clean Au and Pt electrodes in the same electrolyte. Similar to the results seen in alkaline media, this suppression of electrochemical activity is likely due to the presence of thiols on the electrode surface. Nevertheless, the scans are shown in Figure 4.10 for comparison.

The modified electrode displays a primary oxidation peak at 1.1 V_{RHE} in the anodic scan and a secondary peak at 0.95 V_{RHE} in the cathodic scan. These values align with the peaks associated with Au electrocatalysis towards glycerol (peaks A and B in Figure 4.9, respectively). No distinct Pt features are observed, despite the fact that Pt was electrochemically active in alkaline media. This suggests that Pt should also be active here. The absence of Pt activity indicates that either an excess of thiol is still present on the surface, suppressing Pt electrochemistry, or the Pt response is being masked by the more dominant Au electrochemical activity. As shown in the following, it is the excess of thiol that is the dominant factor.

4.2.4.1 Expanded Potential Window

To investigate the apparent lack of Pt activity, the same approach was applied as before, where the potential window was widened to include the region where thiol desorption from Au occurs. The resultant voltammogram is presented in Figure 4.11. As the potential window is expanded, a clear difference between the first and final scans is observed. As expected, the first scan shows significantly lower current densities, while the final scan displays a current response much closer to that of the clean Au electrode, though not fully recovered. Additionally, a new peak emerges at 0.6 V_{RHE}, which was absent in the first scan. The position of this peak aligns with the primary oxidation peak for a Pt electrode in the same electrolyte (peak C, Figure 4.9), indicating the presence of electrochemically active Pt on the electrode surface.

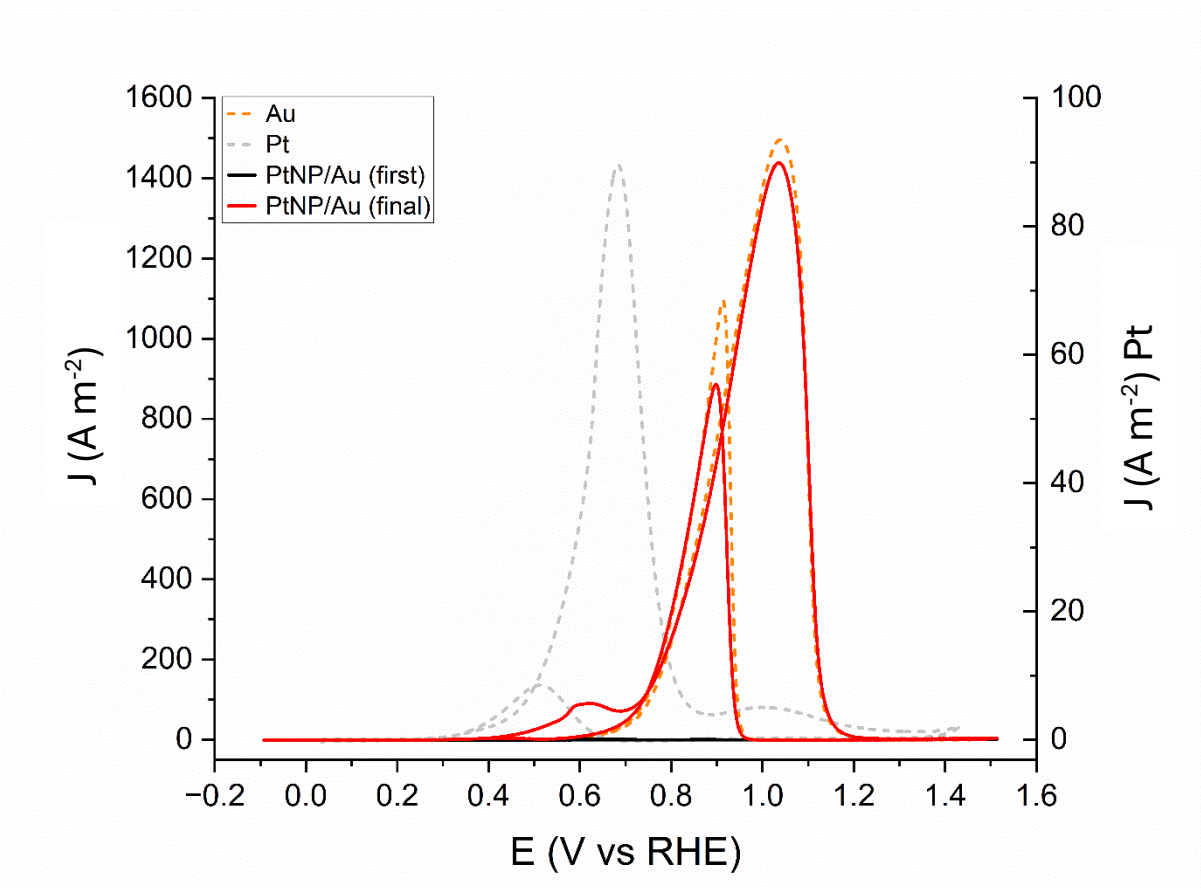

Figure 4.11 CVs of an Au electrode (yellow, left scale), Pt electrode (grey, right scale), and the first (black) and final (red) scans of the Au electrode modified with Pt NPs (left scale), for an expanded potential window. CVs were recorded in 0.1 M NaOH and 0.1 M GlyOH, v = 50 mV s^{-1}. Au ⌀ = 25 µm, Pt ⌀ = 25 µm. Total number of scans = 14.

All scans of the modified surface are presented in Figure 4.12. As the potential is cycled, the peak at 0.6 V_{RHE} grows, indicating an increase in Pt electrochemical activity. This suggests that repeated cycling of the potential within this expanded potential window facilitates the removal of thiol, thereby exposing more of the Pt surface and increasing its contribution to the electrocatalysis of glycerol, and further suggests that the Pt is actually accessible to the solution and exhibits the same electrochemistry as its bulk counterpart.

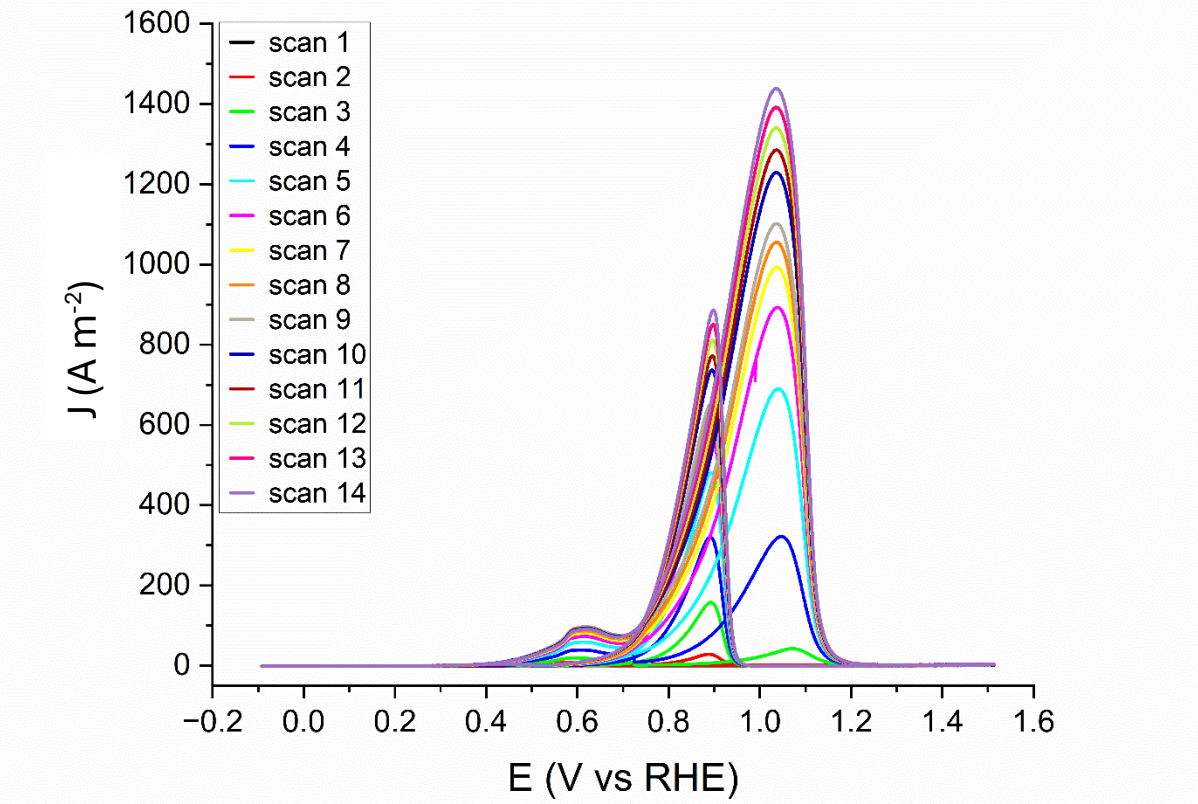

Figure 4.12 All CVs measured of the Pt-modified Au electrode, for an expanded potential window, in 0.1 M NaOH + 0.1 M GlyOH, v = 50 mV s^{-1}. Au ⌀ = 25 µm.

The emergence of distinct Pt features in glycerol supports the notion that the thiol shell undergoes rearrangement. Nonetheless, given the known complications with excess thiol, further experiments using thiol-only modified electrodes would be required to conclusively decouple the effects of free thiol versus nanoparticle-bound thiol.

4.2.5 Discussion

The aim of this study was to investigate the stability and structural evolution of thiolated Pt NPs on Au surfaces. By employing STM, XPS, and cyclic voltammetry, the redistribution of thiols, the exposure of Pt on the Au substrate, and the corresponding electrochemical activity were evaluated.

STM imaging revealed structural changes upon immobilisation of these thiolated Pt NPs onto Au (111) surfaces. The formation of monoatomic Pt features, as well as a lateral

spread of these features, suggests the presence of monoatomic Pt islands across the Au substrate. This suggests that the Pt NP cores became unstable after immobilisation on the Au surface. This instability is in part increased by the partial redistribution of thiols from the Pt NPs to the Au substrate, as supported by the XPS data. Given that Au-S bonds are stronger than Pt-S bonds,[2] it can be generalised that both enthalpic and entropic driving forces favour the redistribution of thiols from the Pt surface to the Au substrate. While STM imaging confirms the formation of Pt islands on the Au (111) substrate, it does not allow for conclusive characterisation of the surrounding thiol domains. Higher-resolution STM studies could provide further insights into whether thiol species remain bound to the Pt surface or are redistributed across the Au substrate.

XPS data confirmed that for the Au (111) substrate modified with Pt NPs, the majority of the signals in the S2*p* spectrum (73.3%) corresponded to Au-S bonds, while only 26.7% of the signal came from Pt-S bonds. This provides further evidence of the thiol redistribution to the Au surface. The partial redistribution leaves some thiols bound to the Pt NPs, while exposing Pt on the substrate, which likely leads to the formation of monoatomic islands observed in the STM images.

Cyclic voltammetry measurements of the modified Au surface initially showed reduced current densities in both alkaline media and in the presence of glycerol, indicating that the presence of thiols suppressed the electrochemical activity of Pt. In alkaline media, the CVs revealed a secondary reduction peak in the cathodic scan, which was assigned to the reduction of oxides on Pt. When the potential window was expanded, cycling the potential resulted in a more pronounced Pt-related reduction peak and a gradual recovery of the Au surface. This was attributed to the progressive removal of thiols from

the electrode surface as it was cycled into more negative potentials, though whether these thiols originate from the migration process or are free thiols as a result of the particle synthesis requires further investigation.

In the presence of glycerol, the initial CVs also showed suppressed current densities due to thiols on the surface. However, upon expanding the potential window, a new oxidation peak emerged that was not present on the clean Au electrode. The position of this peak aligned with the expected oxidation potential of a Pt electrode, indicating the exposure of electrochemically active Pt sites as the thiols were desorbed from the surface.

These findings suggest that, if we assume thiols remaining from the synthesis procedure are negligible, when Pt NPs are immobilised onto an Au substrate, they form monoatomic Pt islands that exhibit electrochemical behaviour similar to that of bulk Pt. The electrochemical responses matched those expected of a Pt electrode, which is consistent with the literature. Given that the Au–Pt bulk alloy exhibits a miscibility gap, it is unlikely that the two metals form an alloy in this system.[4] As a result, the distinct electrochemistry of both metals was observed without interference or blending of their features. This behaviour is expected, as Pt nanoparticles can exhibit electrochemical responses similar to bulk Pt when they are sufficiently large and not influenced by alloying or strong substrate interactions. Given the known miscibility gap between Au and Pt, alloying is unlikely, and the Au substrate is not expected to significantly alter the Pt electrochemistry.

4.3 Modification of Silver Substrates

This section reports on the electrochemical behaviour of Pt NPs immobilised onto an Ag electrode, to determine whether Pt would be exposed and electrochemically active when deposited on a different metal surface. In the absence of STM or XPS data for this system, electrochemistry was used as a proxy to infer surface interactions. While this provides valuable insight, the conclusions must remain tentative in the absence of corroborating structural evidence. Cyclic voltammetry measurements were conducted in both alkaline media (0.1 M NaOH) and in the presence of glycerol to evaluate the electrochemical activity of the modified surface. The same approach was followed, where the voltammogram of the modified surface was analysed to assess whether it exhibited characteristic features of only Ag, a contribution from both Ag and Pt, or a voltammogram with features distinct from either metal.

4.3.1 Electrochemistry of Pt NPs on Ag in 0.1 M NaOH

Pt nanoparticles were immobilised onto an Ag electrode via overnight immersion. Figure 4.13 presents the CVs for the clean Pt electrode, clean polycrystalline Ag electrode, and the Pt NP-modified Ag electrode, showing both the first and final scans of the modified surface. The final scan of the modified electrode is very similar to that of a clean Ag electrode, indicating that the Ag surface is largely recovered as the electrode is cycled. No distinct Pt-specific electrochemical features are observed in the final scan, suggesting that the Pt NPs are not exposed or electrochemically active in this system. Moreover, there is no clear evidence of Pt NPs on the surface, as the first scan of the modified electrode does not display the characteristic first two oxide formation peaks observed in the blank Ag electrode CV (peaks A and B). Additionally, the reduction peak

in the modified electrode's CV exhibits a slight shoulder (peak C), which may indicate some alteration of the surface but is insufficient to confirm the presence of Pt NPs.

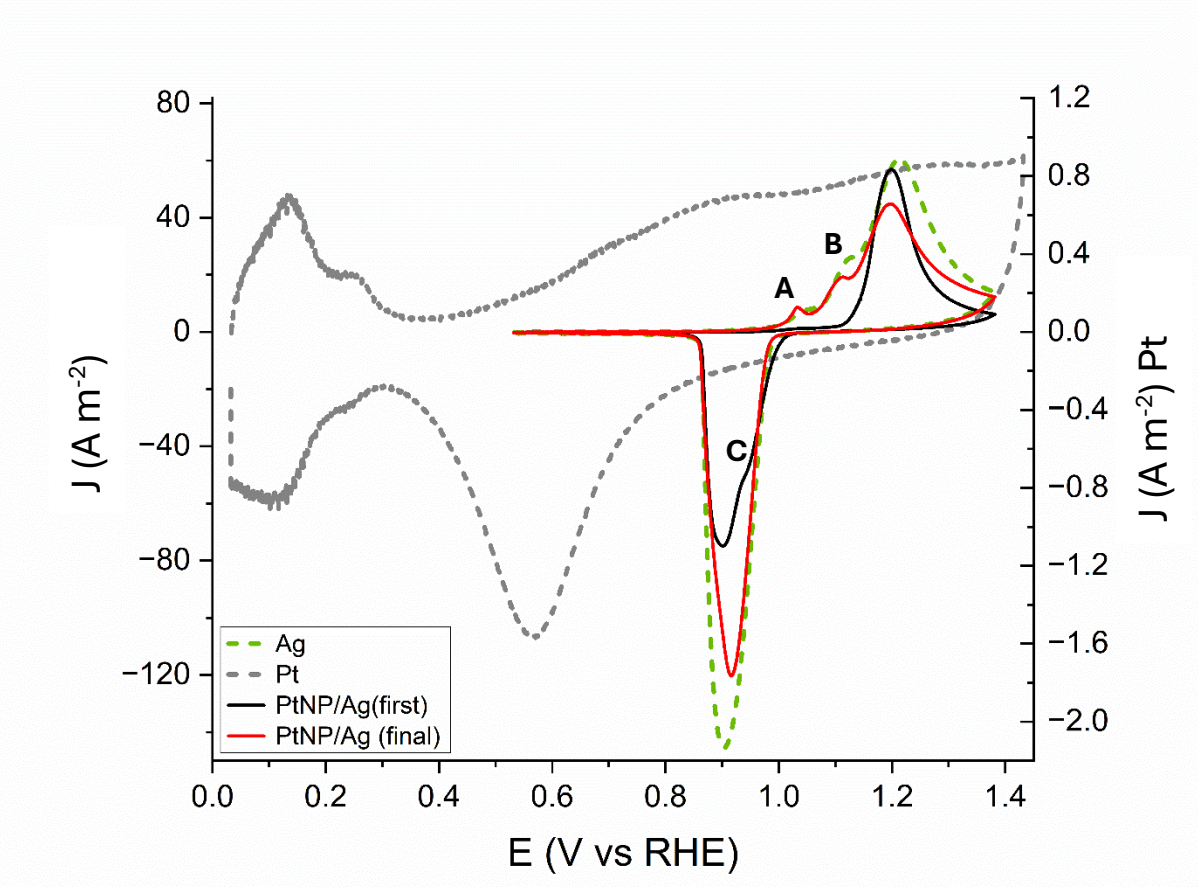

Figure 4.13 The CVs of clean Ag (green) and Pt (grey) electrodes, and the first (black) and final (red) scans of the Ag electrode modified with Pt NPs via incubation. CVs were recorded in 0.1 M NaOH, v = 50 mV s^{-1}. Ag ⌀ = 2 mm, Pt ⌀ = 25 µm. Total number of scans = 10.

All measured scans of the modified electrode are presented in Figure 4.14. Across all scans, the absence of Pt-specific voltammetric features further suggests that, if Pt NPs are present on the Ag surface, they do not result in observable Pt electrochemistry. As the potential is cycled, the Ag surface may be roughened, which likely aids in recovering the Ag electrode's original characteristics. During this process, any thiols present on the surface would likely be removed. Thus, if Pt is present, it is either removed along with the thiols as the surface is cleaned, or it remains on the surface but is not electrochemically active.

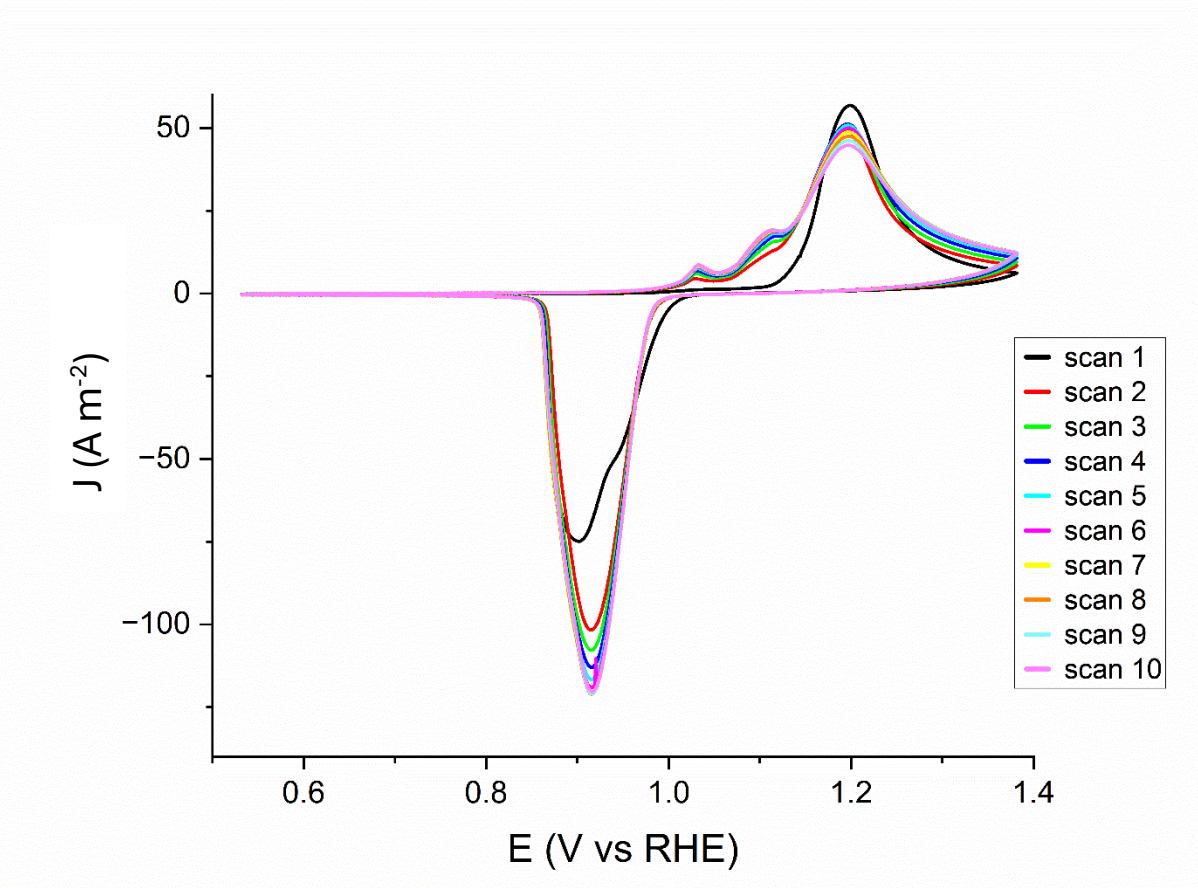

Figure 4.14 All ten CVs measured over the course of an experiment of the Pt-modified Ag electrode. CVs were recorded in 0.1 M NaOH, v = 50 mV s^{-1}. Ag ⌀ = 2 mm.

The cyclic voltammetry so far suggests that, if Pt NPs are present on the Ag surface, they do not contribute significantly to the electrochemical behaviour, with the Ag surface largely dominating the response. The absence of distinct Pt features implies that Pt is either not exposed or not electrochemically active. To further investigate the potential presence of Pt, the modified electrode was tested in the presence of glycerol, where both Pt and Ag exhibit distinct electrochemical responses.

4.3.2 Electrochemistry of Pt NPs on Ag in 0.1 M NaOH and 0.1 M Glycerol

The results of the Pt NPs on an Ag electrode in the presence of 0.1 M glycerol are presented in Figure 4.15, which includes the CVs for the clean Pt electrode, clean Ag electrode, and the Pt NP-modified Ag electrode. The Ag electrode exhibits its typical response in glycerol, showing no electrochemical activity towards the electrooxidation of glycerol, and its CV closely resembles that of Ag in 0.1 M NaOH. In contrast, the clean Pt electrode displays the characteristic response of Pt in 0.1 M glycerol, as reported in the literature (see chapter 3.2.4).

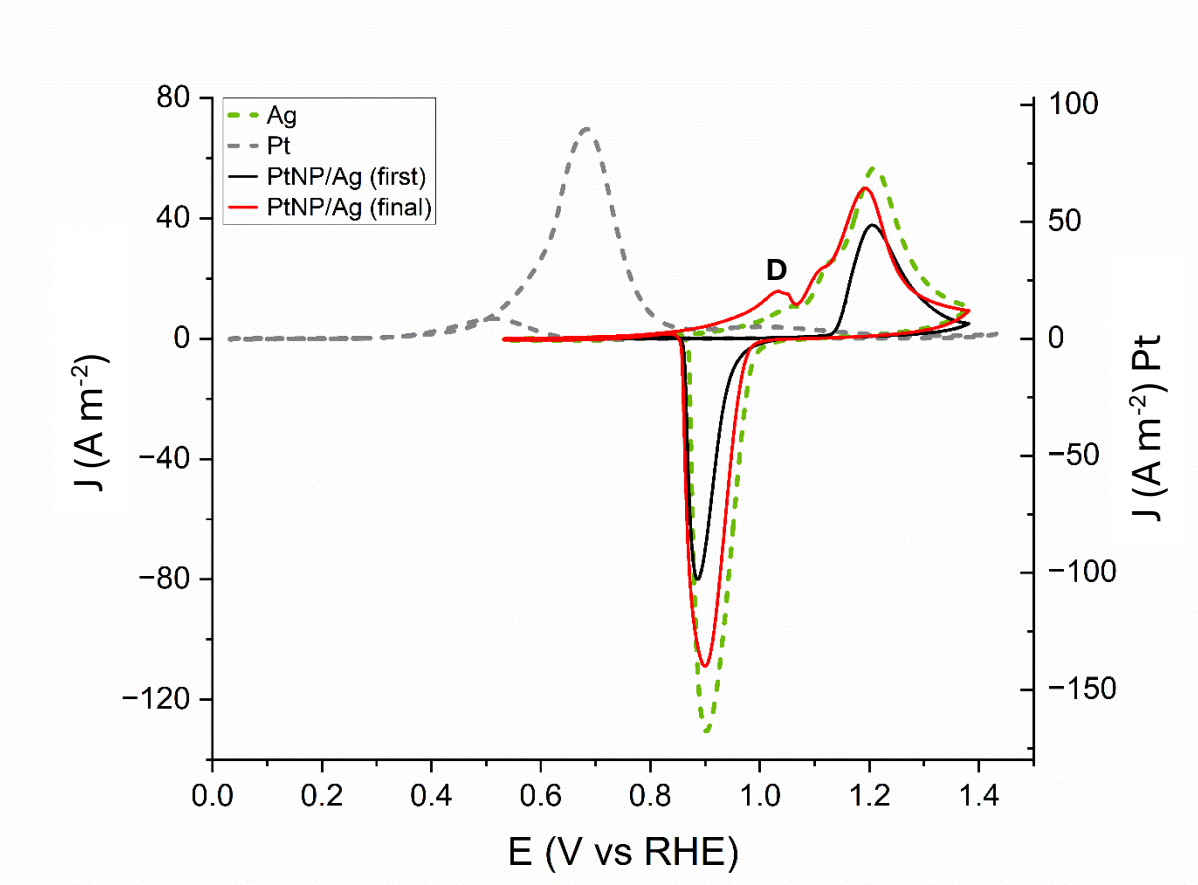

Figure 4.15 CVs of an Ag electrode (green, left scale), Pt electrode (grey, right scale), and the first (black) and final (red) scans of the Ag electrode modified with Pt NPs (left scale). CVs were recorded in 0.1 M NaOH and 0.1 M GlyOH, v = 50 mV s^{-1}. Ag ⌀ = 2 mm, Pt ⌀ = 25 µm. Total number of scans = 13.

For the modified electrode, the final scan shows minimal difference from that of the clean Ag electrode in the same electrolyte, namely the increase in current density and more pronounced appearance of the peak at approximately 1.0 V_{RHE} (peak D). On the Ag electrode, this peak is typically attributed to the formation of AgOH intermediate species, rather than any contribution from Pt-specific electrochemistry.[21,22]

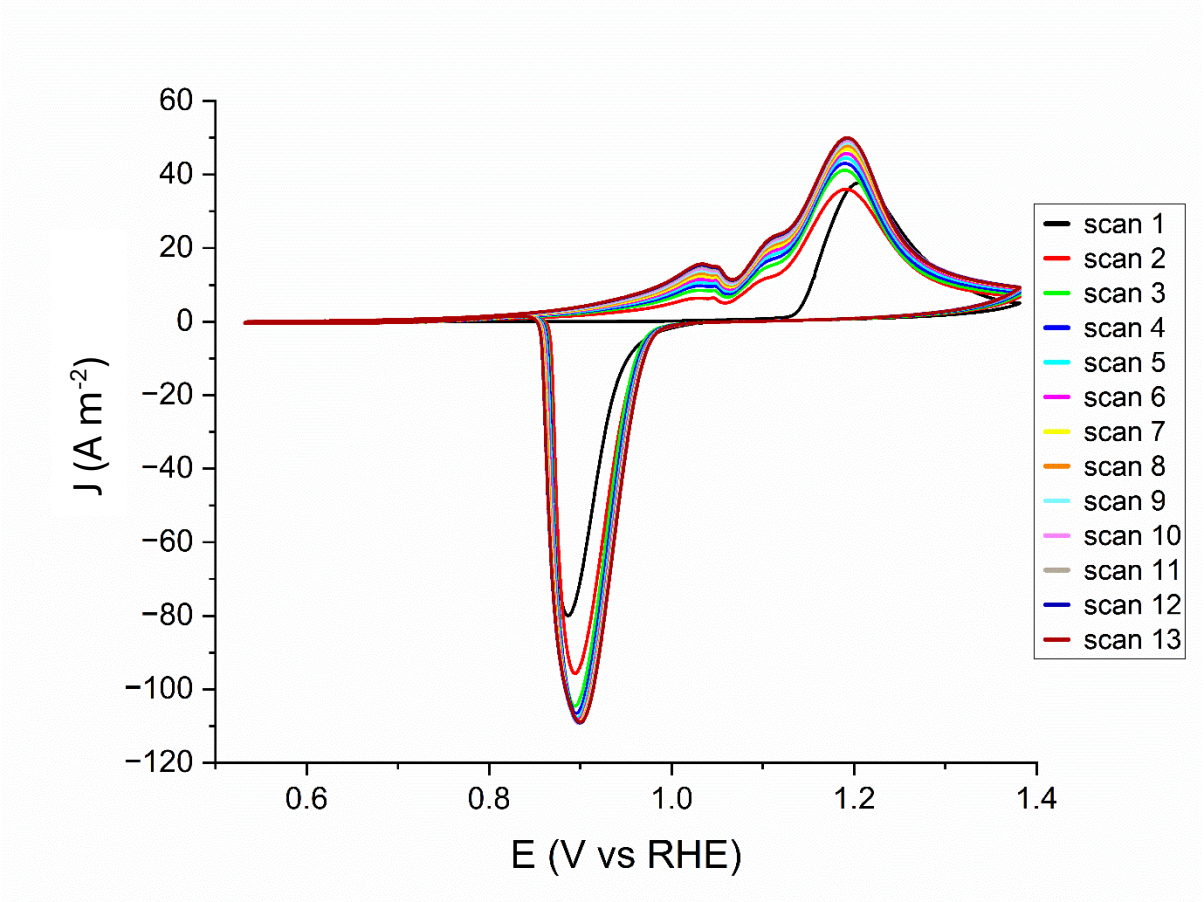

Figure 4.16 All CVs measured of the Pt-modified Ag electrode, in 0.1 M NaOH + 0.1 M GlyOH, v = 50 mV s^{-1}. Ag ⌀ = 2 mm.

All measured scans from the experiment are presented in Figure 4.16. It can be observed that the oxide formation peaks in the anodic scan increase in current as the potential is cycled. This behaviour is expected, as the roughness of the electrode increases with cycling. Similarly, the reduction peak in the cathodic scan also shows an increase in current density. However, for both the oxidation and reduction peaks, the CVs eventually

stabilise, with successive scans beginning to overlap, indicating that no further significant changes are occurring at the surface. Notably, despite these changes, no Pt-specific electrochemistry is observed throughout the cycling process.

4.3.3 Discussion

In Chapter 3, we investigated the behaviour of Ag NPs deposited onto a Pt electrode under the same experimental conditions. In that system, some Ag-specific electrochemistry was observed in the oxide formation region of Ag; however, no significant contribution to the CVs could be attributed to Ag in the presence of glycerol. In both electrolytes, the voltammograms primarily reflected the characteristics of the Pt bulk electrode, which recovered after an initial current depression upon cycling.

In the present chapter, Pt NPs were immobilised onto an Ag electrode. Due to the absence of STM or XPS data for the Pt/Ag system, interpretation of the electrochemical behaviour is limited. The possibility that excess thiols influence the surface behaviour cannot be ruled out, and without visual or spectroscopic evidence of nanoparticle attachment, any conclusions drawn must be considered tentative. Further characterisation is required to determine whether observed changes in the voltammograms arise from nanoparticle-related processes or simply from thiol-induced surface modification. It is important to note that the following discussion rests on the assumption that the Pt NPs were indeed deposited onto the Ag surface, without excess thiols in solution.

The Pt NP-modified Ag electrode showed no significant changes in electrochemical behaviour compared to the clean Ag electrode. The small changes in the oxidation peak observed in Figures 4.17 and 4.18, while slightly different from the clean Ag electrode, do

not show a shift in the potential at which this oxidation process occurs. This suggests that the observed peak is still an Ag-related process, specifically AgOH formation, and does not indicate a contribution from the Pt NPs. The shoulder in the oxide reduction peak of Ag in 0.1 M NaOH does not correspond to any potential associated with Pt oxide reduction activity. Furthermore, this same feature, along with differences in the oxidation peaks, is observed when Au NPs are immobilised on the Ag electrode. This evidences that the feature is not specific to the Pt particles (see chapter 5.2.1).

From literature reports, it is known that the Pt-thiol bond is stronger than the Ag-thiol bond.[2] Thus, in the case of Pt NPs on Ag, enthalpic considerations would not favour a redistribution of thiols from the Pt NPs to the Ag surface due to the stronger Pt-S interaction. While the entropic factor would favour a thiol migration process, this is not evidenced in this system, as no changes in the Ag electrochemistry can be attributed to Pt-specific features arising from exposed Pt on the Ag substrate. Though the Ag electrode is largely recovered, the current densities do not fully match those of an unmodified electrode. This suggests that some thiol-protected Pt may still remain on the surface.

It is unsurprising that no voltammetric features deviating from standard Ag electrode behaviour were observed. Assuming the immobilisation of the Pt NPs was successful, it is evident that, despite the entropic driving force, the difference in metal-thiol bond strengths is the determining factor in preventing the disintegration of the ligand shell.

Furthermore, there is no evidence of Pt interacting with Ag to form an electrochemically active alloy in alkaline media, consistent with their well-documented miscibility gap in bulk states.[23] The electrochemical responses observed in these experiments suggest that, if Pt is present, it remains passivated.

However, without direct evidence of Pt NPs on the surface, caution must be exercised when interpreting the electrochemical data. The absence of Pt-specific features could also result from unsuccessful NP deposition. Thus, while the conclusions drawn here are reasonable based on the electrochemical data, they remain speculative in the absence of surface characterisation to confirm the presence of Pt NPs.

4.4 Conclusion

The aim of this chapter was to investigate systems of Pt nanoparticles immobilised onto Au and Ag substrates, focusing on the structural stability of the particles and the corresponding effects on the electrochemical properties of the modified surfaces.

For Pt NPs on Au, XPS confirmed that thiol redistribution occurred from the Pt NP surface to the Au substrate. While some signal of Pt-S binding was detected, the majority of the signal originated from Au-S binding. This is consistent with the stronger Au-S bond and the significantly larger Au substrate, which provide both enthalpic and entropic driving forces for the thiol redistribution process. The migration of the Pt NP thiol capping layer left the Pt cores exposed, which subsequently decomposed into monoatomic Pt islands, as observed in STM imaging of the modified substrate. The electrochemical characterisation of the modified surface showed contributions from both metals. Specifically, distinct features in the voltammogram for the electrooxidation of glycerol could be attributed to Pt and Au individually. These observations were made in an expanded potential window that facilitated the removal of thiols from the surface. Importantly, no features deviated from conventional Au and Pt electrochemistry, aligning with the known bulk miscibility gap between Au and Pt. It is unsurprising that the two metals did not mix under these conditions, and our results suggest that this behaviour persists even when the two metals are in different size regimes. The modified surface, containing electrochemically active Au and Pt, may be desirable for functional applications in catalysis and sensing, as the two metals can contribute independently.

For Pt NPs immobilised onto an Ag substrate, XPS and STM data were unavailable to confirm the successful deposition of the particles. Assuming the particle deposition was

successful, the observed electrochemical behaviour aligns with expectations. No Pt-specific contributions were observed in the voltammograms, either in alkaline media or in the presence of glycerol. Furthermore, the Ag voltammogram did not fully recover in terms of current density compared to the unmodified Ag electrode. This suggests the presence of thiol-protected Pt particles that are not electrochemically active.

These results are consistent with the difference in Pt-S and Ag-S bond strengths, where the stronger Pt-S bond stabilises the Pt particles. However, this stability prevents the Pt particles from contributing to the electrochemistry of the modified surface. Future work on this system should include more detailed characterisation, such as in situ STM, to provide direct evidence of NP deposition and to explore any structural changes the Pt particles may undergo, despite remaining passivated on the Ag substrate.

4.5 References

1 N. Awais, P. Rodriguez and T. Albrecht, *ECS Trans*, 2020, **97**, 885.

2 D. Y. Petrovykh, H. Kimura-Suda, A. Opdahl, L. J. Richter, M. J. Tarlov and L. J. Whitman, *Langmuir*, 2006, **22**, 2578–2587.

3 D. R. Lide, *CRC Handbook of Chemistry and Physics, 85th Edition,* Taylor & Francis, 2004.

4 V. Ponec and G. C. Bond, *Catalysis by Metals and Alloys*, Elsevier, 1995, vol. 95.

5 Z. Peng and H. Yang, *J Solid State Chem*, 2008, **181**, 1546–1551.

6 J. Wisniewska, H. Guesmi, M. Ziolek and F. Tielens, *J Alloys Compd*, 2019, **770**, 934–941.

7 B. N. Wanjala, J. Luo, B. Fang, D. Mott and C.-J. Zhong, *J Mater Chem*, 2011, **21**, 4012–4020.

8 L. Deng, W. Hu, H. Deng and S. Xiao, *The Journal of Physical Chemistry C*, 2010, **114**, 11026–11032.

9 S. Swaminarayan, R. Najafabadi and D. J. Srolovitz, *Surf Sci*, 1994, **306**, 367–380.

10 A. I. Yanson, P. V Antonov, Y. I. Yanson and M. T. M. Koper, *Electrochim Acta*, 2013, **110**, 796–800.

11 K. Itaya, S. Sugawara, K. Sashikata and N. Furuya, *Journal of Vacuum Science & Technology A*, 1990, **8**, 515–519.

12 M. A. Floridia Addato, A. Rubert, G. Benítez, E. Zelaya, G. Cabello, A. Cuesta, J. E. Thomas, A. Visintín, R. C. Salvarezza and M. H. Fonticelli, *The Journal of Physical Chemistry C*, 2013, **117**, 7589–7597.

13 T. Ishida, N. Choi, W. Mizutani, H. Tokumoto, I. Kojima, H. Azehara, H. Hokari, U. Akiba and M. Fujihira, *Langmuir*, 1999, **15**, 6799–6806.

14 H. I. Lee, S. H. Joo, J. H. Kim, D. J. You, J. M. Kim, J.-N. Park, H. Chang and C. Pak, *J Mater Chem*, 2009, **19**, 5934–5939.

15 L. D. Burke and P. F. Nugent, *Gold Bull*, 1997, **30**, 43–53.

16 S. Hebié, T. W. Napporn, C. Morais and K. B. Kokoh, *ChemPhysChem*, 2016, **17**, 1454–1462.

17 D. Zhan, J. Velmurugan and M. V Mirkin, *J Am Chem Soc*, 2009, **131**, 14756–14760.

18 P. Daubinger, J. Kieninger, T. Unmüssig and G. A. Urban, *Physical Chemistry Chemical Physics*, 2014, **16**, 8392–8399.

19 J. F. Gomes and G. Tremiliosi-Filho, *Electrocatalysis*, 2011, **2**, 96.

20 Y. Kwon, Y. Birdja, I. Spanos, P. Rodriguez and M. T. M. Koper, *ACS Catal*, 2012, **2**, 759–764.

21 M. Lopez Teijelo, J. R. Vilche and A. J. Arvia, *J Appl Electrochem*, 1988, **18**, 691–698.

22 S. Chen, B. Wu and C. Cha, *Journal of Electroanalytical Chemistry*, 1996, **416**, 53–59.

23 K. A. Kane, A. C. Reber, S. N. Khanna and M. F. Bertino, *Progress in Natural Science: Materials International*, 2018, **28**, 456–463.

5. Modification of Silver and Platinum Substrates with Gold Nanoparticles

Chapter Contents

This chapter reports the modification of Pt and Ag substrates with Au nanoparticles (NPs). Au NPs on a Pt surface have previously been reported to remain intact, and similar behaviour is expected here, as the thiol migration process is countered by the stronger Au-S bond compared to the Pt-S bond.[1–3] As such, results are anticipated to reflect still-protected Au NPs on the Pt substrate. A similar outcome is expected for Au NPs on Ag, as the Au-S bond is also stronger than the Ag-S bond.[3] Thus, the Au NPs are predicted to remain stabilised by their ligand shell. However, in both systems, there exists an entropic driving force that could promote thiol migration onto the larger substrate surface relative to the NP surface.

This chapter first details the synthesis and characterisation of $Au_{144}(HT)_{60}$ NPs, followed by their immobilisation onto Pt and Ag substrates. The characterisation of these newly modified surfaces is presented using XPS and cyclic voltammetry.

5.1 Gold Nanoparticle Synthesis and Characterisation

The gold nanoparticles used to modify Pt and Ag surfaces were synthesised using a modified Brust-Schiffrin protocol, following the procedure reported by Qian *et al*.[4] This protocol produces thiolated nanoparticles of two sizes, $Au_{144}(HT)_{60}$ and $Au_{25}(HT)_{18}$, with $Au_{144}(HT)_{60}$ as the major product. The $Au_{144}(HT)_{60}$ particles were separated for use in subsequent experiments (detailed in 2. Materials and Methods).

TEM imaging was performed on the Au NPs to confirm their morphology. Unlike the Ag and Pt nanoparticles prepared by cathodic corrosion, where thiol capping is applied as a separate step after cleaning, the Brust-Schiffrin method incorporates thiol capping as part of the synthesis process itself. Consequently, the Au NPs were imaged with their thiol ligands already attached. The TEM image, shown in Figure 5.1, shows particles with an average diameter of 2.8 ± 1.0 nm, with the error determined rom the standard deviation of the histogram.

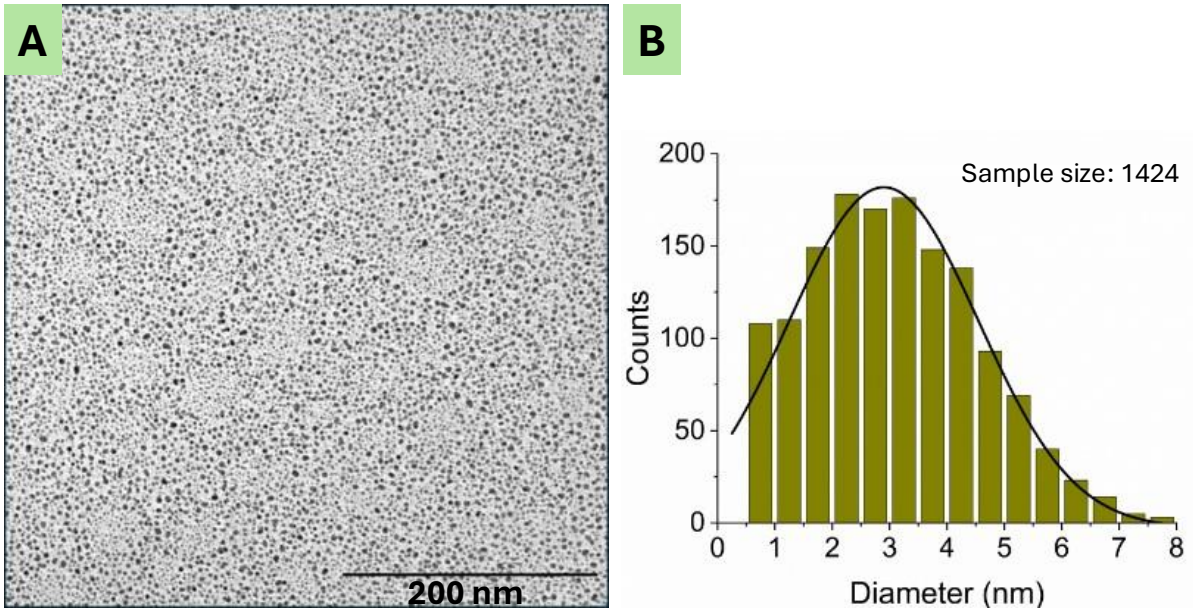

Figure 5.1 (A) TEM image of $Au_{144}(HT)_{60}$ nanoparticles, and **(B)** particle size distribution analysis.

After synthesis, the Au NPs were immobilised onto Ag and Pt substrates. XPS and electrochemical analyses were then performed to evaluate the stability and structural evolution of the nanoparticles on the modified surfaces.

5.2 Modification of Silver Substrates

This section examines the behaviour of $Au_{144}(HT)_{60}$ particles immobilised onto a polycrystalline Ag electrode via overnight immersion in a solution of thiolated Au NPs, as described in 2.3.4 Modification of Metal Substrates with Nanoparticles. No STM or XPS data have been obtained for this system; however, CV measurements were conducted to investigate the electrochemical characteristics of the modified substrate. These measurements were performed in 0.1 M NaOH initially, and then the electrochemical activity of the modified substrate towards the electrocatalysis of 0.1 M glycerol (with 0.1 M NaOH as a supporting electrolyte) was also evaluated.

By analysing the CV features, one can assess the behaviour of the immobilised Au NPs. If the voltammogram revealed only Ag-related activity, it would suggest that the Au NPs on the surface are either passivated by thiols, or that the surface coverage of Au is insufficient to produce an electrochemical signal. Conversely, if both Ag and Au characteristics are observed, this would indicate that Au is exposed and electrochemically active in the same manner as bulk Au. Should the CV exhibit features that cannot be ascribed to either Ag or Au alone, this may suggest alloy formation, introducing new electrochemical behaviour distinct from either pure metal. This behaviour was observed in for Ag NPs deposited onto an Au electrode (chapter 3.2). We therefore aim to ascertain whether such alloying will occur in the reverse system of Au NPs on an Ag substrate.

5.2.1 Electrochemistry of Au NPs on Ag in 0.1 M NaOH

This section examines the electrochemical behaviour of an Ag electrode modified with Au NPs in 0.1 M NaOH. Figure 5.2 presents the first and final scans of the modified electrode, alongside the CVs of the clean Au and Ag electrodes for comparison.

Both the clean Au and Ag electrodes exhibit their characteristic voltammograms. For the Au electrode, the CV was discussed in detail in chapter 3.2. Briefly, Au oxide formation is indicated by an oxidation peak (peak A) appearing between 1.09 and 1.51 V_{RHE}, while the reduction of this oxide layer is marked by a peak at 0.92 V_{RHE} (peak B) in the cathodic scan.[5,6]

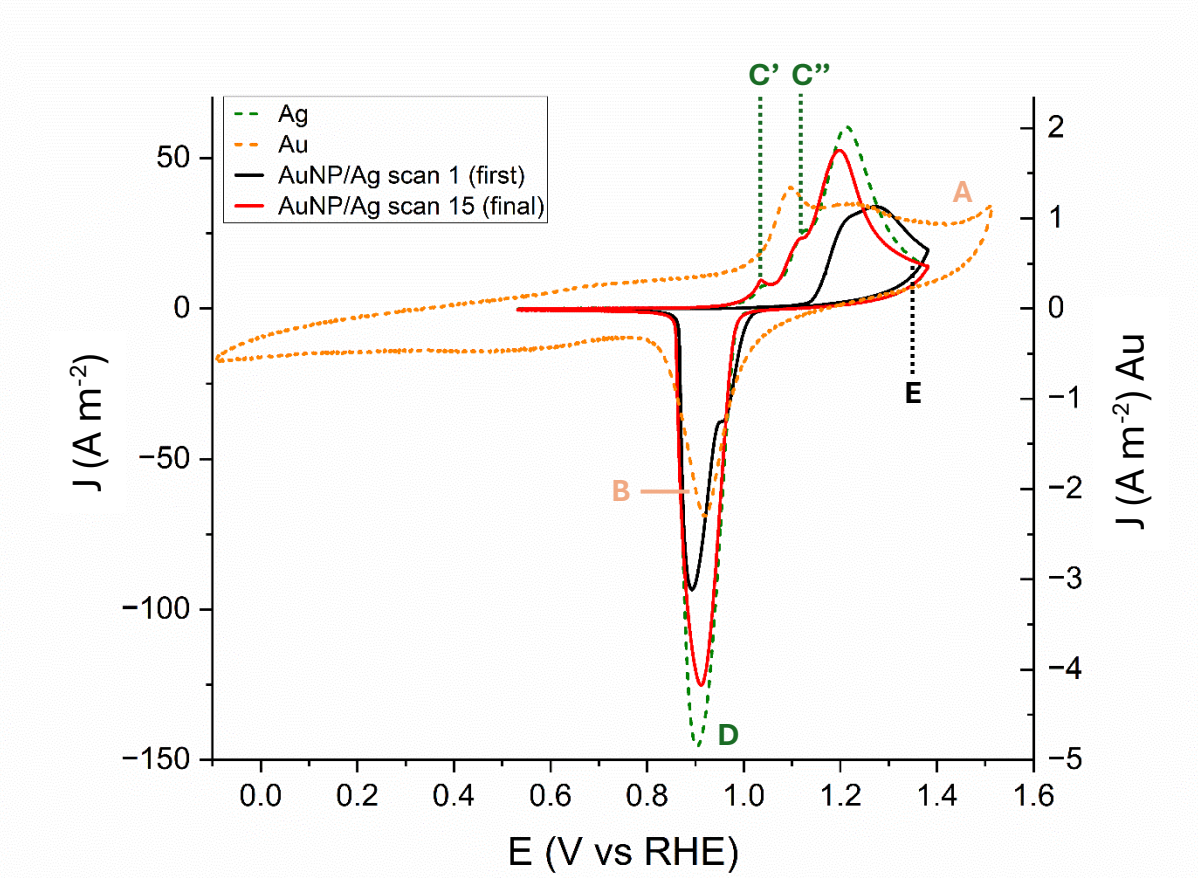

Figure 5.2 CVs of an Ag electrode, (green, left scale), Au electrode (yellow, right scale), and the first (black) and final (red) scans of the Ag electrode modified with Au NPs (left scale). CVs were recorded in 0.1 M NaOH, v = 50 mV s^{-1}. Au ⌀ = 25 µm, Ag ⌀ = 2 mm. Total number of scans = 15.

The CV of the blank Ag electrode was covered in detail chapter 3.2; it shows the typical response of a polycrystalline Ag electrode in alkaline media. In the anodic scan, two shoulder peaks are observed at 1.04 and 1.13 V_{RHE} (peaks C' and C'', respectively), followed by a large oxidation peak at 1.21 V_{RHE}. These three peaks correspond to the formation of multilayers of silver oxide (Ag_2O). In the cathodic scan, a peak appears at 0.9 V_{RHE}, attributed to the reduction of the oxide layer (peak D).[7–9]

The first scan of the Au NP-modified Ag electrode reveals notable differences compared to the clean Ag electrode. Unlike the pure Ag electrode, which exhibits three distinct oxide formation peaks in the anodic scan, the modified electrode shows only a single peak (peak E), within the same potential region characteristic of both Ag and Au oxide formation. Additionally, the reduction peak in the cathodic scan displays a shoulder at 0.96 V_{RHE}, a feature absent in the clean Ag CV. By the final scan, the CV of the modified electrode closely resembles that of the clean Ag electrode in terms of its voltammetric shape. However, the current density remains lower for the modified substrate, suggesting that the Ag surface is not fully recovered and that some material remains on the surface.

Figure 5.3 presents all measured scans for the modified electrode recorded during an experimental run. It is evident that the first scan differs from all subsequent scans, particularly with regards to the shoulder on the reduction peak. This shoulder likely results from silver-thiol interactions. As observed in chapter 4.3, when Pt NPs were deposited onto an Ag electrode in 0.1 M NaOH, the electrode showed a similar shoulder at 0.95 V_{RHE}. As this feature was observed for the modification of the Ag electrode by both

Pt and Au nanoparticles, it is likely attributable to the presence of the thiol species, which is common to both systems, rather than the NP material itself.

After the first scan, the second and all subsequent scans closely resemble the clean Ag CV. The voltammetric features remain largely unchanged between the second and final scans, with only the current density shifting towards values closer to the clean Ag electrode, though not reaching the capacitive currents measured for a clean Ag electrode entirely. This suggests that the Ag surface undergoes partial recovery during potential cycling but does not fully restore to its unmodified state, as noted earlier.

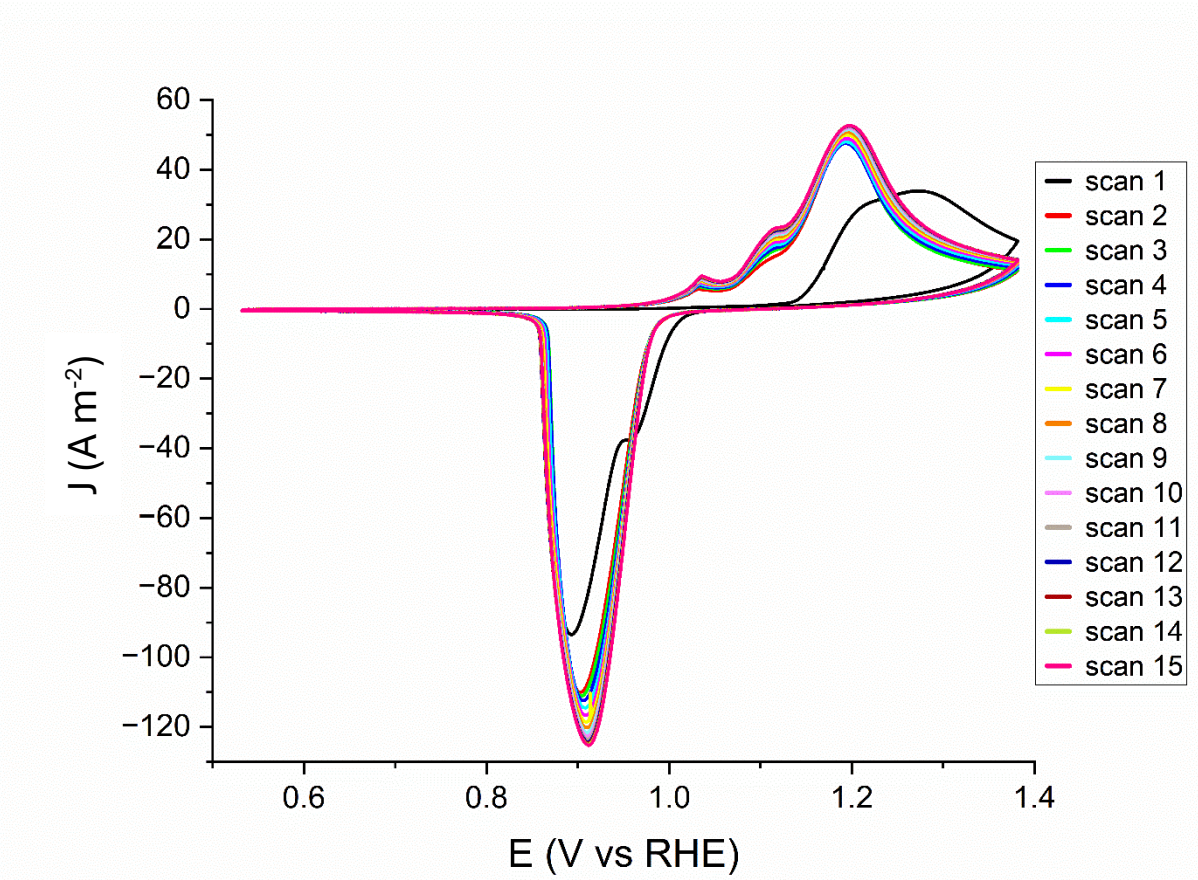

Figure 5.3 All CVs measured of the AuNP/Ag electrode in 0.1 M NaOH, v = 50 mV s^{-1}. Au ⌀ = 25 µm, Ag ⌀ = 2 mm.

To gain further insight into the presence and activity of Au on the Ag substrate, the electrochemistry of the modified electrode was next measured in the presence of glycerol.

5.2.2 Electrochemistry of Au NPs on Ag in 0.1 M NaOH and 0.1 M GlyOH

Here we report the electrochemistry of the Ag electrode modified with Au NPs in the presence of glycerol (GlyOH). As Ag is not electrocatalytically active towards the oxidation of glycerol, any observable electrocatalytic activity in this system could be attributed to the presence of electrochemically active Au features on the Ag substrate.

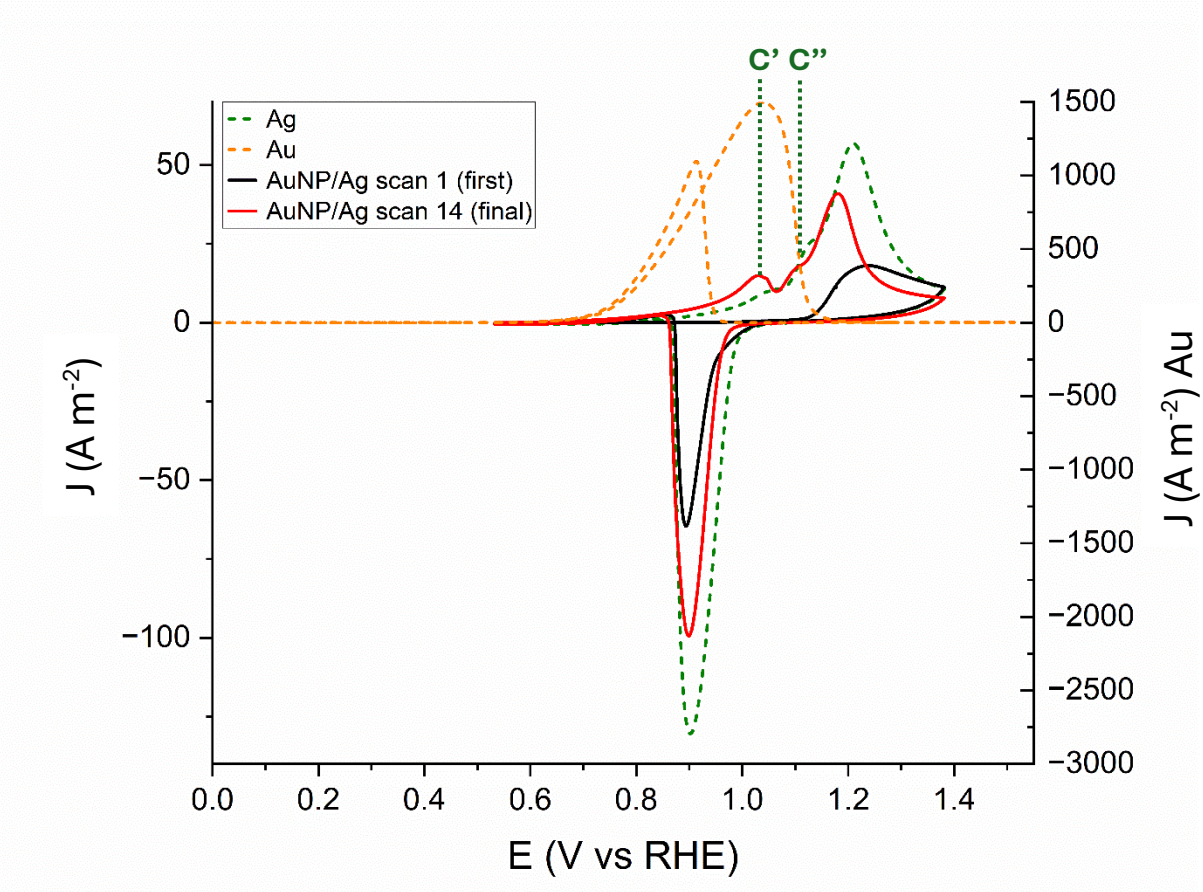

Figure 5.4 CVs of an Ag electrode, (green, left scale), Au electrode (yellow, right scale), and the first (black) and final (red) scans of the Ag electrode modified with Au NPs (left scale). CVs were recorded in 0.1 M NaOH + 0.1 M GlyOH, v = 50 mV s^{-1}. Au ⌀ = 25 µm, Ag ⌀ = 2 mm. Total number of scans = 14.

Measurements were performed in 0.1 M NaOH, into which glycerol was added to achieve a final concentration of 0.1 M glycerol in the cell.

Figure 5.4 presents the first and final scans of the modified electrode, alongside the CVs of the clean Au and Ag electrodes measured in the same electrolyte. The CV of the unmodified Au electrode aligns with literature, displaying a primary oxidation peak in the anodic scan at 1.0 V_{RHE} and a secondary oxidation peak in the cathodic scan at 0.9 V_{RHE}.[10] As expected, the CV of the unmodified Ag electrode in the presence of glycerol closely resembles its CV in NaOH, as Ag is not catalytically active in the electro-oxidation of glycerol.

The first scan of the modified electrode exhibits a different shape from both the clean Ag and Au electrodes. Notably, the first two oxide formation peaks typically observed in the anodic scan of Ag (peaks C' and C'') are absent. By the final scan, the voltammogram of the modified electrode shows a recovery of the Ag substrate, with features closely resembling those of a clean Ag electrode.

The final scan of the modified electrode also shows a difference in comparison with the unmodified Ag electrode, particularly at peak C', which is more pronounced on the modified electrode. While the position of this peak aligns with the primary electro-oxidation peak of a clean Au electrode (approximately 1.0 V_{RHE}), this feature was also observed at the same position when the Ag electrode was modified with Pt NPs (chapter 4.3). There, the peak was not attributed to Pt activity, as the primary oxidation peak for Pt occurs at 0.68 V_{RHE}. This suggests that the peak does not necessarily originate from Au, and so the differences in the voltammogram do not reflect the presence of electrochemically active Au. However, similar to the measurements in 0.1 M NaOH, the

current density values in the final scan do not fully align with those of the clean, unmodified Ag voltammogram.

Figure 5.5 presents all measured scans for the system. Similar to the measurements in 0.1 M NaOH, after the first scan, there is little variation between subsequent scans. The primary difference is the current densities, which increase with potential cycling and progressively grow to those of the clean Ag electrode, due to cleaning and roughening of the electrode surface.

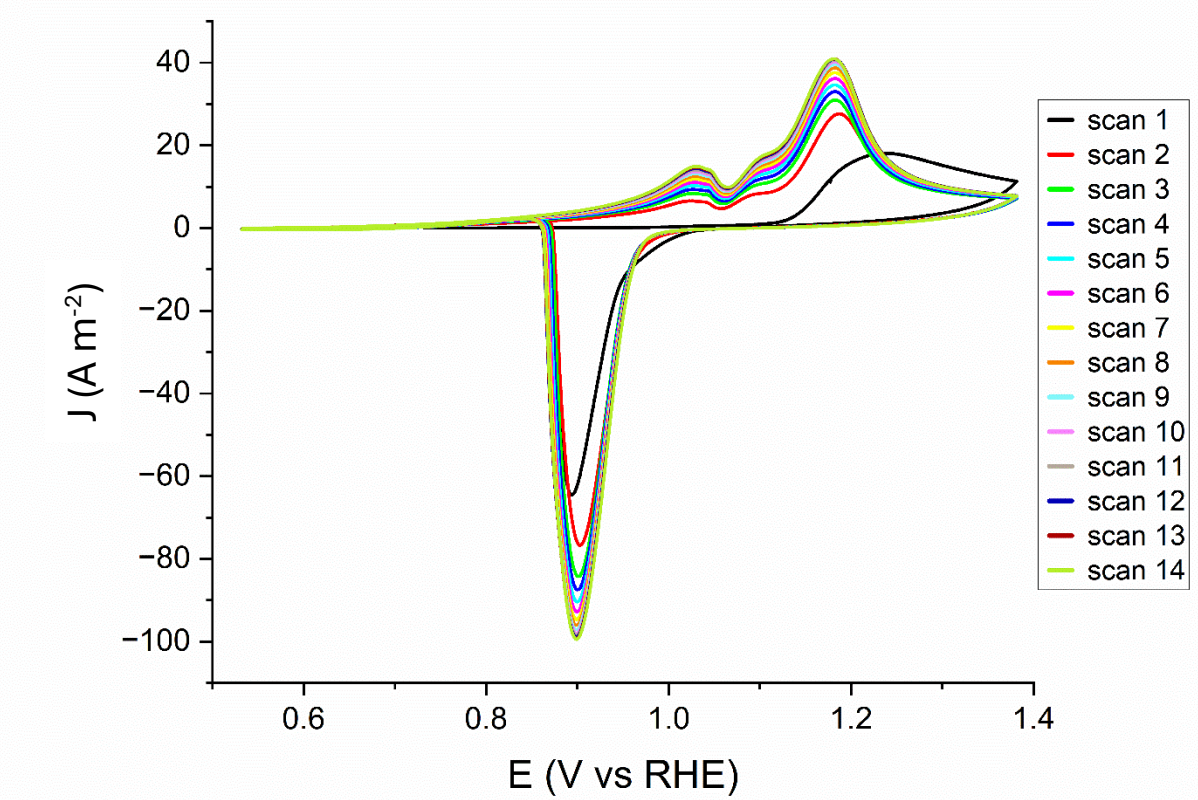

Figure 5.5 All CVs measured over the course of an experiment of the Au-modified Ag electrode in 0.1 M NaOH + 0.1 M GlyOH, v = 50 mV s^{-1}. Au ⌀ = 25 µm, Ag ⌀ = 2 mm.

5.2.3 Discussion

The characterisation of the Ag electrode modified with Au NPs relied solely on electrochemical methods, as no STM or XPS data are currently available. Without direct evidence from surface characterisation, the presence of Au NPs on the Ag substrate cannot be definitively confirmed. However, all the substrates across the systems studied (Ag, Au, and Pt) were modified with NPs using the same immersion protocol. In chapter 3.2, Ag NPs were successfully deposited onto Au substrates, confirmed by XPS, STM, and with their electrochemical contribution also observed. Since the same surface modification protocol was applied to the Ag electrode, it is reasonable to assume that Au NPs were successfully deposited onto the Ag surface.

In 0.1 M NaOH, the first scan of the modified electrode displayed significant differences from the clean Ag and Au electrodes. Only a single oxide formation peak was observed, contrasting with the three distinct peaks typical of clean Ag. Additionally, the reduction peak in the cathodic scan exhibited a shoulder at 0.96 V_{RHE}, a feature not observed in the CVs of clean Ag or Au, but also present in the Pt NP-modified Ag electrode system (chapter 4.3). This suggests that the observed shoulder could be due to silver-thiol interactions rather than an effect of either metal nanoparticle, Au or Pt. As thiol desorption on Ag typically occurs at much lower potentials (around 0 V_{RHE}), the exact source of this reduction feature remains unclear.[11] Subsequent scans indicated partial recovery of the Ag electrode surface, as the voltammogram resembled that of the clean Ag electrode in terms of the redox features. However, some suppression of current densities remained, relative to the CV of the unmodified Ag electrode.

In the presence of glycerol, the first scan of the modified electrode also exhibited notable differences, including the absence of typical Ag oxide reduction peaks. However, as in NaOH, subsequent scans showed the partial recovery of the Ag surface, with the voltammogram closely resembling that of the clean Ag electrode, barring the measured current densities. A more pronounced oxide formation peak was observed in the final scan of the modified electrode compared to the clean Ag electrode. This peak, though aligning with the primary oxidation peak of clean Au (1.0 V_{RHE}), was also present when Ag was modified with Pt NPs, where glycerol is oxidised by Pt at 0.68 V_{RHE}. Thus, it is unlikely that this peak originates from Au on the substrate, as it was observed for both Au and Pt NPs despite the onset of glycerol oxidation being different for each metal.

Overall, the Au NPs do not exhibit distinct electrochemical activity on the Ag substrate. In both 0.1 M NaOH and glycerol, no Au-specific voltammetric features were observed, and the Ag surface was largely recovered from the second cycle onwards. Although the CVs of the modified surface matched those of a clean Ag electrode in terms of features and onset potentials, the current densities were not fully restored, indicating the presence of thiol-protected Au NPs remaining on the surface.

A potential explanation is that the Au NPs remain passivated on the Ag surface, possibly because the S-Au bond is stronger than the S-Ag bond.[3] Expanding the potential window more negatively could potentially reductively desorb the thiols and uncover any Au present. However, attempts to expand the potential window resulted in electrode instability, making this approach impractical for this system.

Based on our data, we conclude that as the Ag substrate is cleaned via potential cycling, the Au NPs are also desorbed from the surface. It appears that the Au remains passivated

prior to its removal, which would explain the absence of any Au-specific electrochemical activity throughout the scans. Although literature reports suggest that Ag and Au preferentially interact to form alloy surfaces in both bulk and nanoscale mixtures, and this was observed in the reverse system, of Ag NPs on Au (chapter 3.2), no such behaviour is evident in the reverse scenario.[12] However, it is important to emphasise that surface coverage and the presence of Au NPs on the Ag substrate require direct confirmation, as our conclusions here rely solely on indirect electrochemical evidence.

5.3 Modification of Platinum Substrates

This subchapter focuses on the characterisation of Pt substrates modified with Au NPs via overnight immersion. The primary objective was to evaluate the stability of Au NPs on Pt substrates by characterising the modified surface through XPS and cyclic voltammetry.

5.3.1 XPS of Au NPs on Pt (111)

The Au NPs were immobilised onto a Pt (111) substrate via overnight immersion in a solution of thiolated Au NPs, as described in 2.3.4 Modification of Metal Substrates with Nanoparticles, and the modified substrate was characterised using XPS. To characterise the binding energy (BE) values of the metal-thiol interactions, the following measurements were conducted; 1-hexanethiol (HT) on Au (111) to determine the S-Au BE, and also on Pt (111) to determine the S-Pt BE, and Au NPs on HOPG to determine the S-Au NP BE. Finally, Au NPs on Pt (111) were measured to assess whether the thiols were preferentially bound to the nanoparticle surface or the Pt substrate.

The XPS spectra for these experiments are presented in Figure 5.6, with binding energy values and their corresponding relative contributions (RC) summarised in Table 5.1.

Table 5.1 Summary of the measured BE values ad their relative contributions (RC) in XPS spectra of measurements on the Au NPs-Au substrate system. Surface modification via immersion was used for all experiments.

Experiment		S2*p* Signal			
		BE (eV)	RC	BE (eV)	RC
1	HT on Au (111)	162.2	66.2%	163.4	33.8%
2	HT on Pt (111)	162.5	36%	163.6	18%
3	Au NPs on HOPG	163.2	69.3%	164.4	30.7%
4	Au NPs on Pt (111)	163.4	12.8%	164.6	6.4%
		162.6	53.9%	163.7	26.9%

Experiment 1 in Table 5.1 presents the results for HT adsorbed on an Au (111) substrate. The XPS spectrum revealed two BE values: 162.2 eV (66.2%) and 163.4 eV (33.8%), aligning well with literature data.[3,13] The lower BE at 162.2 eV is attributed to S-Au binding, indicating the interaction between sulfur and the Au surface. The higher BE at 163.4 eV corresponds to unbound thiol species, likely physisorbed to the surface or present as residual free thiols in the monolayer.[14]

Experiment 2 shows the results for HT adsorbed on a Pt (111) substrate, with BE values of 162.5 eV (36%) and 163.6 eV (18%). The lower BE at 162.5 eV is attributed to S-Pt binding, and the higher BE at 163.6 eV is associated with unbound thiol species, likely trapped or physisorbed within the monolayer.[3]

Experiment 3 presents the results for Au NPs immobilised onto HOPG. The spectrum revealed BE values of 163.2 eV (69.3%) and 164.4 eV (30.7%). Although no experimental XPS data for the S-Au binding in a $Au_{144}(HT)_{60}$ particle has been directly reported in the literature, a BE of 163.2 eV has been attributed to physisorbed thiol on Au, while a higher BE value, around 164 eV, has been associated with chemisorbed thiol species on Au.[15,16] The value of 163.2 eV is similar to the reported BE of 163.4 eV for HT on Au (111), whereas a BE of 164.4 eV was observed only in experiment 3. Thus, the BE value of 164.4 eV was assigned to the S-Au interaction specific to the NP surface (S-Au NP).

In Experiment 4, the Pt (111) substrate modified with Au NPs was measured. The spectrum for this system displayed signals at 163.4 eV and 164.6 eV, which closely match the unbound or physisorbed thiol and S-Au NP binding energies, respectively, recorded in Experiment 3. These peaks contributed 19.2% to the overall spectrum, indicating that

a portion of the thiol remained bound to the Au NPs after deposition onto the Pt substrate. Additional signals at 162.6 eV and 163.7 eV were observed, corresponding to S-Pt binding energies as determined in Experiment 2. These peaks accounted for 80.8% of the spectrum, demonstrating that the majority of the thiol redistributed onto the Pt substrate.

The XPS results indicate that while some thiols remain bound to the Au NPs, the majority preferentially redistribute to the Pt substrate. This redistribution likely contributes to the destabilisation of the Au NP cores, promoting their disintegration upon deposition. In the case of Pt NPs on Au, STM imaging revealed the formation of monoatomic islands. However, for the Au on Pt system, the structural arrangement could not be directly determined in this study due to the absence of STM data. While it is proposed that the Au NPs become unstable and disintegrate upon immobilisation, the extent of this disintegration within the experimental timeframe remains unclear. To further investigate the modified surface, cyclic voltammetry was employed as the next characterisation technique, offering insights into the electrochemical behaviour of the system.

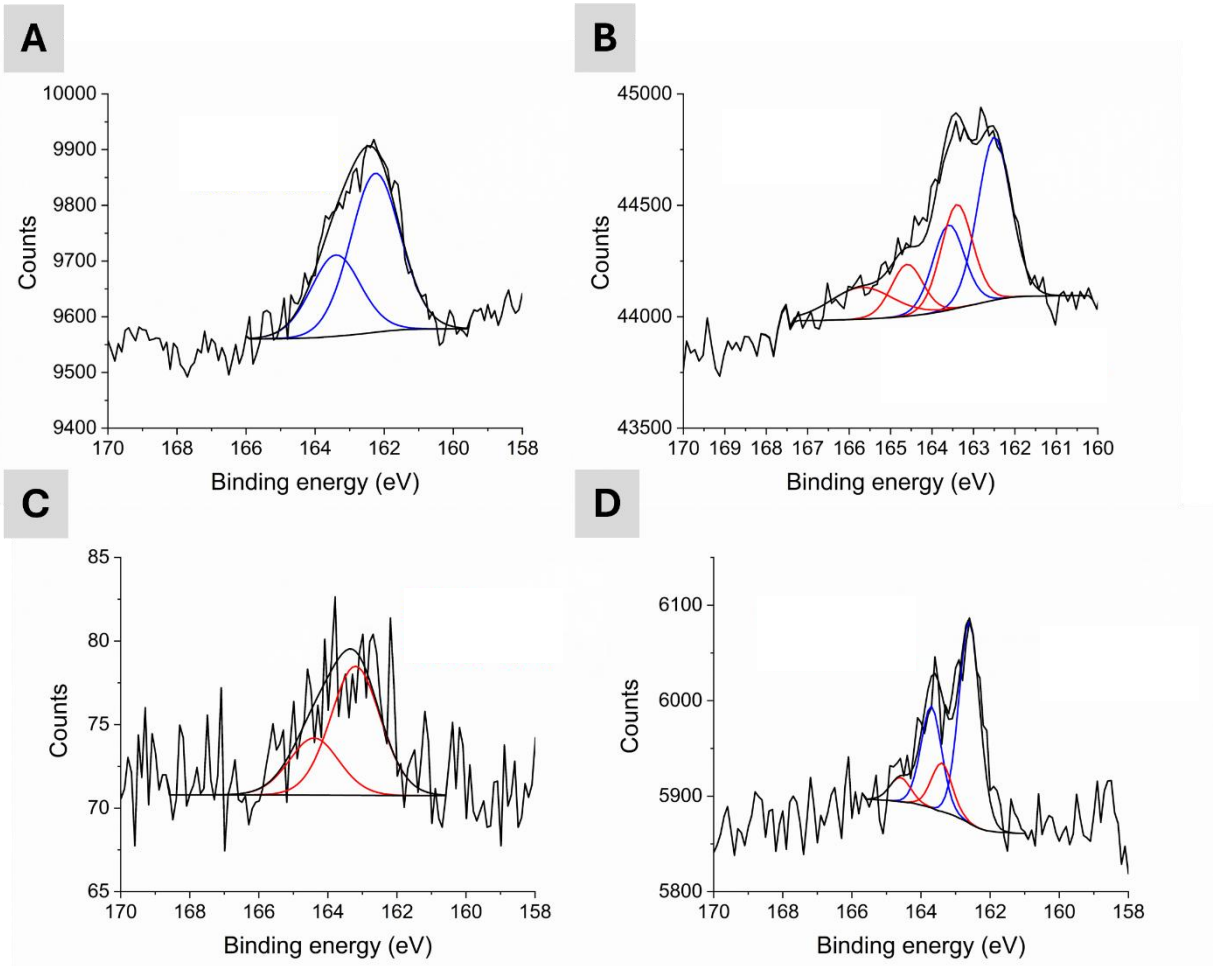

Figure 5.6 XPS spectra of (A) Au NPs drop-cast onto HOPG, (B) SAM of HT on Au (111), (C) SAM of HT on Pt (111), and Au NP immobilised on Pt (111).

5.3.2 Electrochemistry of Au NPs on Pt in 0.1 M NaOH

The electrochemical behaviour of Au NPs immobilised onto a Pt polycrystalline electrode was investigated in 0.1 M NaOH. XPS analysis confirmed that the thiol capping layer redistributed to the Pt substrate, most probably leaving the Au cores partially exposed. Examining the voltammograms of the modified electrode would reveal whether the Au NPs were electrochemically active on the Pt substrate and whether their behaviour mirrored that of bulk Au or was changed due to the influence of the Pt substrate. Given the known miscibility gap between Au and Pt, we anticipated contributions from both metals if both were electrochemically active at the electrode surface.[17] These contributions were expected to resemble the electrochemical behaviour of their respective bulk metal counterparts, consistent with the reverse scenario where Pt NPs were deposited on an Au electrode (see chapter 4.2).

Voltammograms of the Pt electrode, Au electrode, and both the initial and final scans of the modified surface are presented in Figure 5.7. The clean Au and Pt electrodes exhibit their characteristic voltammograms. The Au voltammogram, discussed in the preceding section, displays the expected features of a clean Au surface. The Pt voltammogram reveals the typical electrochemical behaviour of a clean Pt electrode.[18,19] In the anodic sweep, hydrogen desorption is observed at 0.13 and 0.25 V_{RHE}. During the cathodic sweep, hydrogen adsorption occurs at 0.23 and 0.11 V_{RHE}. Extending the potential further into the negative range would lead to the evolution of hydrogen gas. Oxide formation on the Pt surface begins around 0.41 V_{RHE}, with the subsequent reduction of these oxides occurring at 0.57 V_{RHE} during the reverse scan.

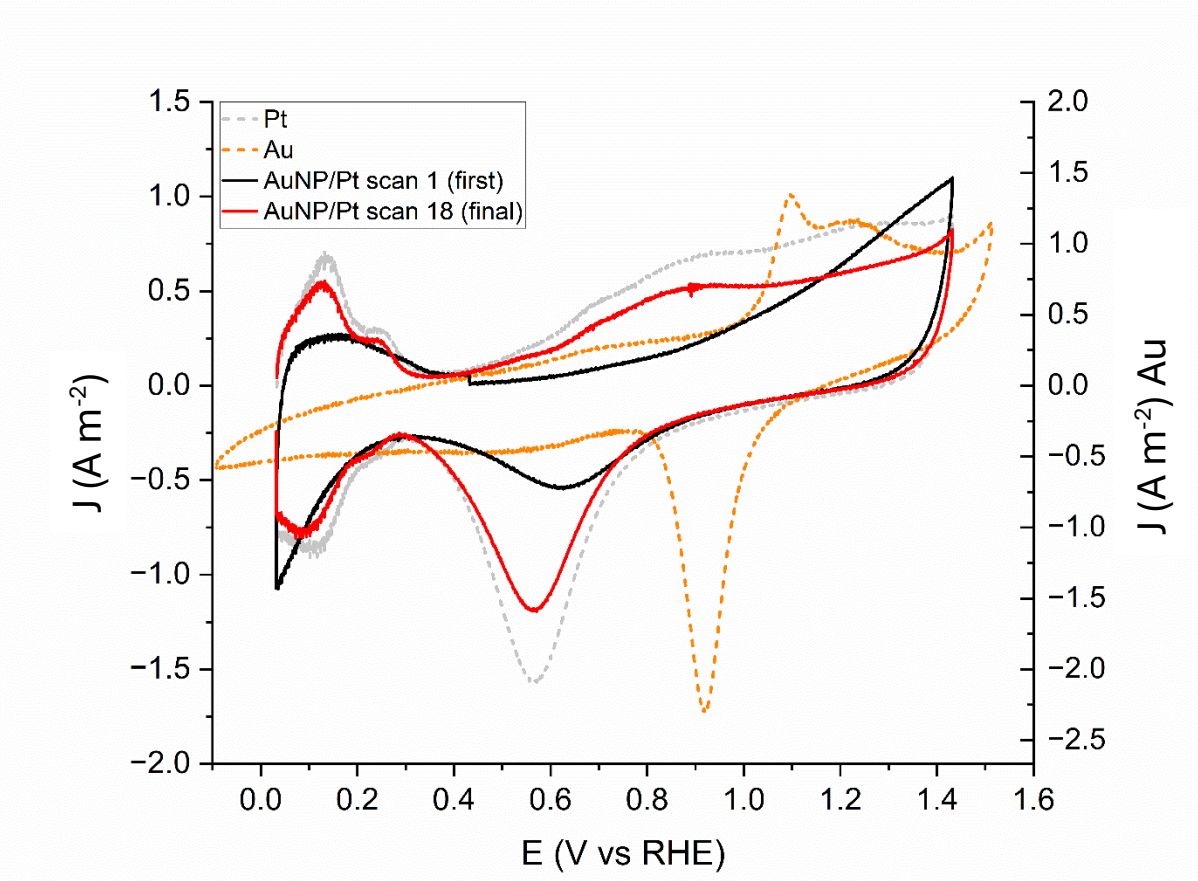

Figure 5.7 CVs of a Pt electrode (grey, left scale) and Au electrode (yellow, right scale), and the first (black) and final (red) scans of the Pt electrode modified with Au NPs (left scale). CVs were recorded in 0.1 M NaOH, v = 50 mV s^{-1}. Pt ⌀ = 25 µm, Au ⌀ = 25 µm. Total number of scans = 18.

The final scan of the modified electrode shows no significant change in voltammetric features compared to the clean Pt electrode, aside from a reduced current density. The first scan of the modified electrode is also presented. It can be noted that the current density suppression is less pronounced in this system than in the reverse case of Pt NPs on an Au electrode, where the first scan of the modified electrode exhibited significantly lower currents (chapter 4.2.3-4). This observation suggests a lower surface coverage of the Pt electrode by Au NPs, compared to the surface coverage of the Au electrode by Pt NPs or that the thiols do not block the Pt surface in the same way as they did the Au.

Figure 5.8 displays all measured scans, showing that after the first scan, there is no significant change as no new features appear. Instead, the subsequent scans show a progressive recovery of the characteristic Pt features, indicating the gradual cleaning of the Pt electrode surface through repeated cycling.

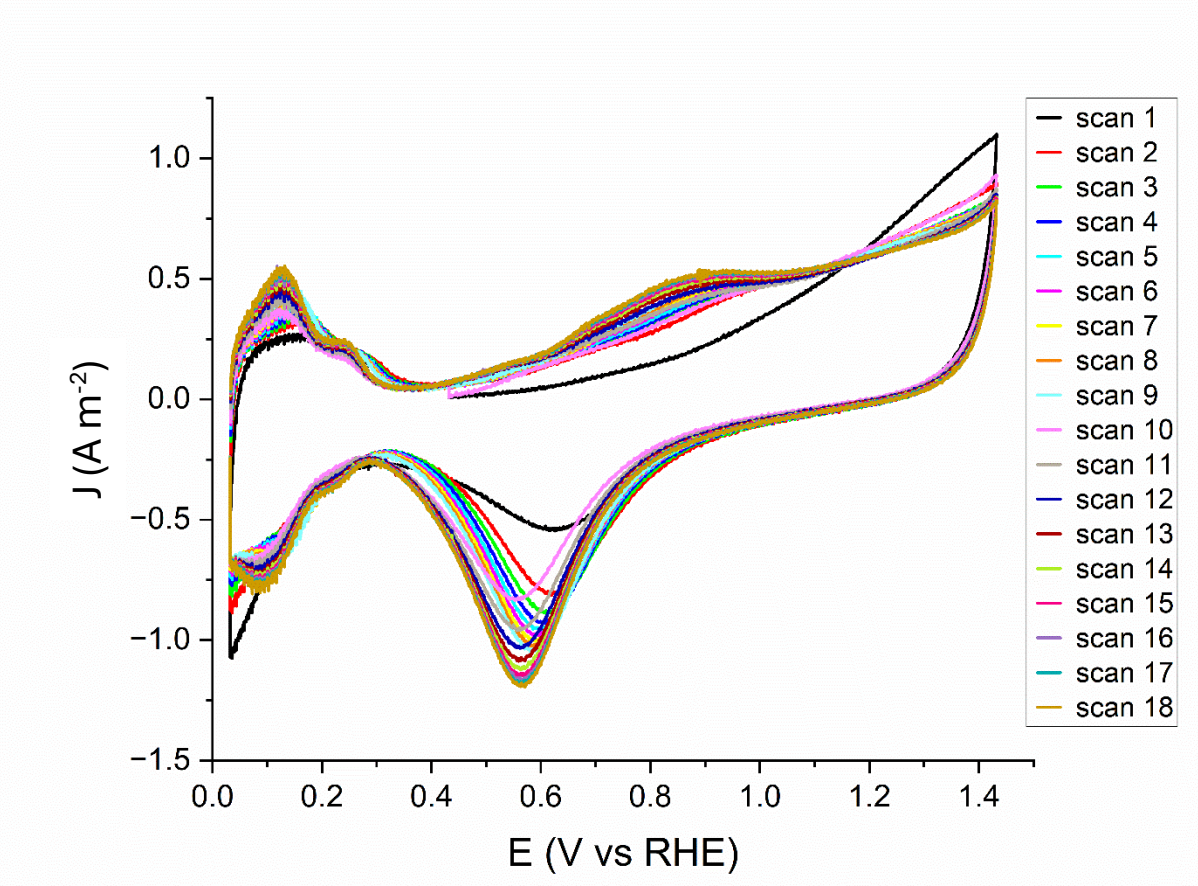

Figure 5.8 All CVs measured of the Au-modified Pt electrode in 0.1 M NaOH, v = 50 mV s^{-1}.

The cyclic voltammograms show no features that can be attributed to the presence of electrochemically active Au on the surface. However, while the Pt electrode surface is progressively recovered with repeated scans, the final stabilised scan reveals that the current density does not fully match that of the clean Pt electrode. This could potentially be due to the presence of thiol or thiol-protected Au remaining on the electrode surface.

To investigate this further, glycerol was introduced to the system to determine whether any Au-specific features would emerge.

5.3.3 Electrochemistry of Au NPs on Pt in 0.1 M NaOH and 0.1 M GlyOH

The modified electrode was measured in the presence of glycerol, as both Au and Pt are electrochemically active toward its electrooxidation. The voltammetric signals from this process are characterised by high current densities and occur at distinct potentials for each metal. Figure 5.9 presents the CV scans of clean Pt, clean Au, and the first and final scans of the modified substrate. The electrochemical responses of both the clean Pt and Au electrodes are consistent with reported literature.[10,20]

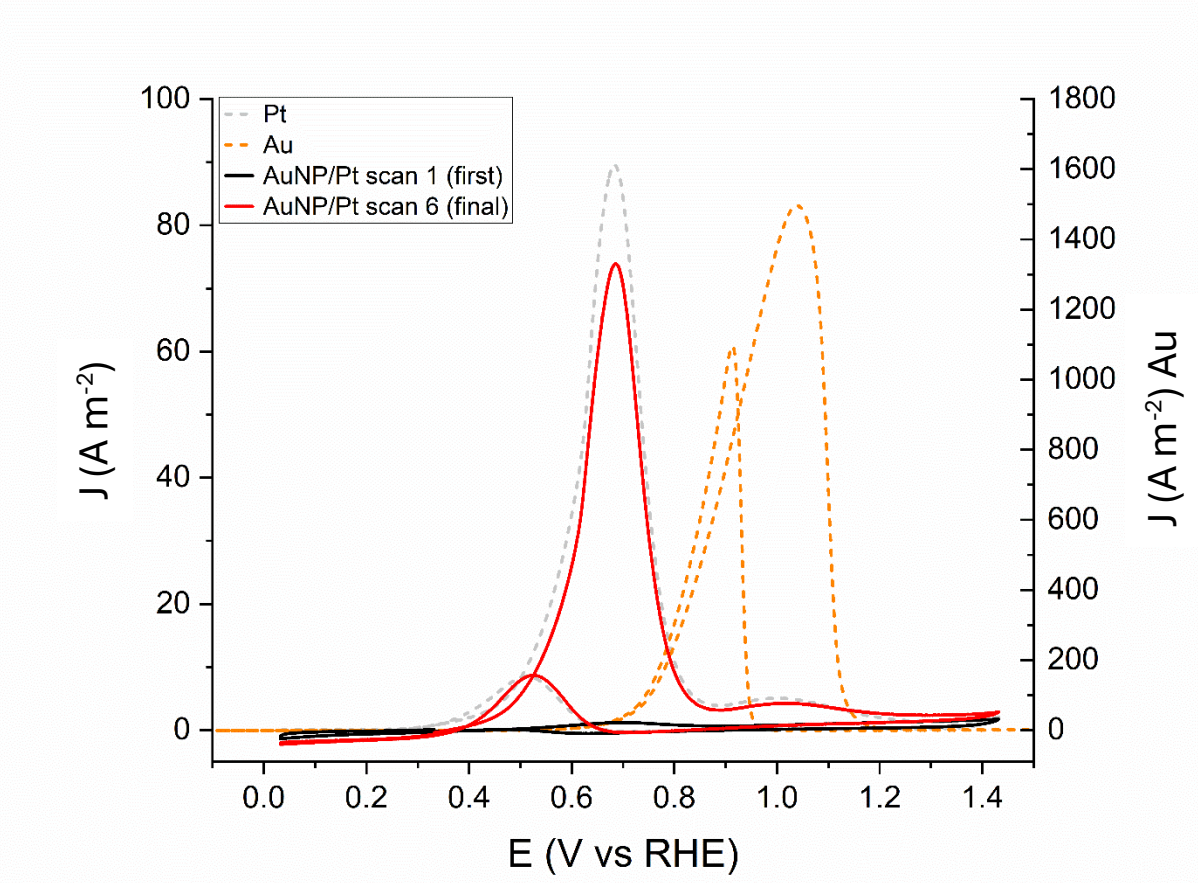

Figure 5.9 CVs of Pt electrode (grey, left scale) and Au electrode (yellow, right scale), and the first (black) and final (red) scans of the Pt electrode modified with Au NPs (left scale). CVs were recorded in 0.1 M NaOH + 0.1 M GlyOH, v = 50 mV s^{-1}. Pt ⌀ = 25 µm, Au ⌀ = 25 µm. Total number of scans = 6.

The first scan of the modified electrode shows a significantly lower current density compared to the clean Pt voltammogram, which is however largely recovered in the final scan. Notably, there is no observable contribution of Au-specific electrochemistry in the voltammograms. The first six CV scans are presented in Figure 5.10, which further confirm that even in the initial scans, no Au-specific voltammetric features are present. These results indicate that Au NPs are not electrochemically active on the Pt substrate in this system.

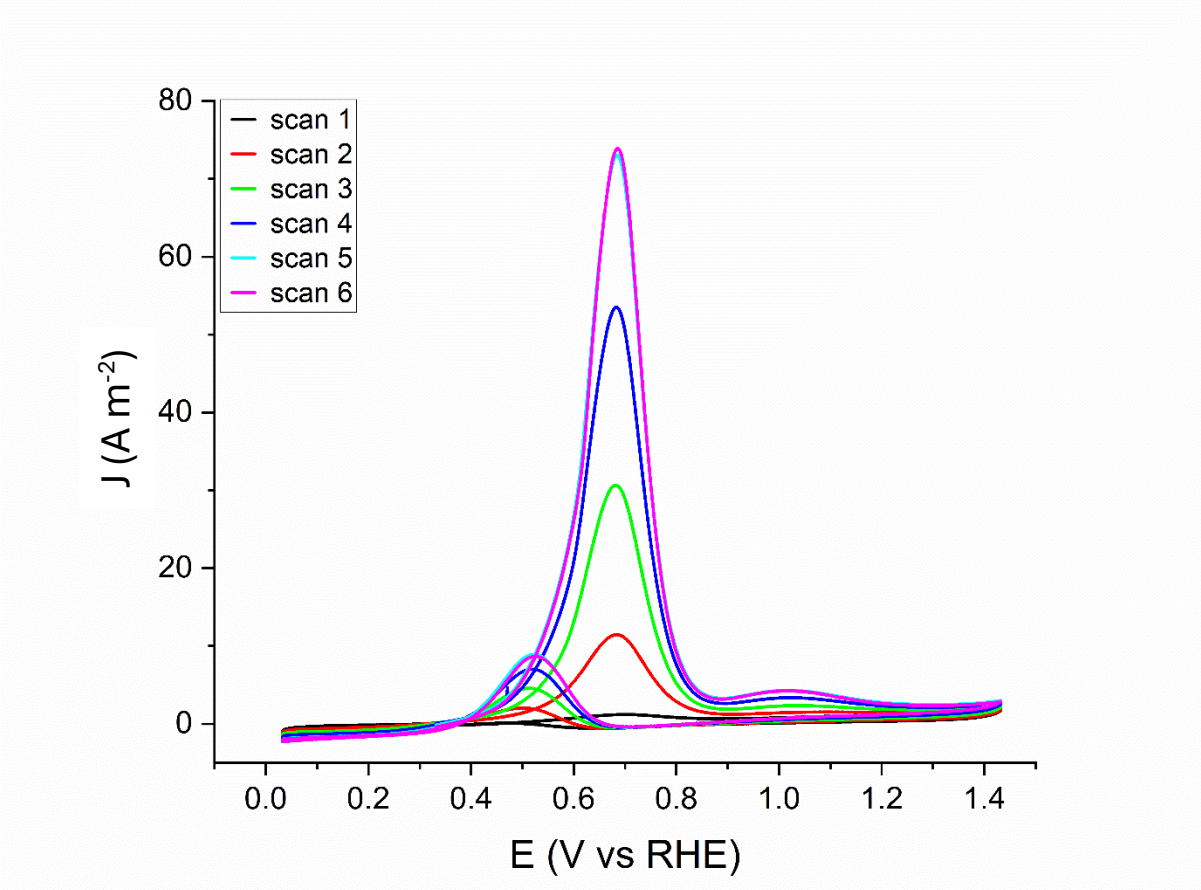

Figure 5.10 All CVs measured of the Au-modified Pt electrode in 0.1 M NaOH + 0.1 M GlyOH, v = 50 mV s^{-1}. Pt ⌀ = 25 µm, Au ⌀ = 25 µm

5.3.4 Discussion

This study aimed to investigate the stability and structural evolution of Au NPs on Pt substrates. XPS and cyclic voltammetry were employed to assess the preferential binding of thiols to either the nanoparticles or the substrate, as well as to evaluate the resulting electrochemical properties of the modified substrate.

XPS results for the Pt (111) substrate modified with Au NPs showed that the majority of the S2*p* signals were attributed to S-Pt bonds (80.8%), with only 6.4% corresponding to S-Au NP binding. These findings provide two key insights. Firstly, we see direct evidence that the immobilisation of Au NPs on the Pt substrate via immersion was successful, confirming the presence of Au NPs on the Pt surface for subsequent electrochemical measurements. Secondly, they show that the thiols redistribute from the Au NP surface and preferentially bind to the Pt substrate, despite the stronger S-Au bond compared to S-Pt (perhaps related to the higher surface energy of Pt), leaving exposed Au features present on the Pt substrate.[3] However, at this stage, the structural nature of these features remains unclear, as it is uncertain whether the Au cores are partially or fully disintegrated.

We know that Au and Pt exhibit a bulk miscibility gap and do not form an alloy, though alloy nanoparticles can be synthesised across various size ranges.[17,21,22] Upon modification with Pt NPs, an Au substrate led to the emergence of Pt-specific features in the voltammogram of the Au electrode, alongside exhibiting Au-specific features. In the reverse system here, one might expect to see Au-specific electrochemical features in the CV of the modified Pt electrode. However, this was not observed here, as only Pt voltammetric features are present across all scans.

Despite the confirmed presence of exposed Au NPs on the Pt substrate, there is no Au contribution to the voltammetry of the modified electrode, either in NaOH or in the presence of glycerol. In both electrolytes, the CV potential window extends into the region where thiol desorption from Au occurs, meaning the Au should not remain passivated by thiols.[23]

The absence of observable Au electrochemistry could be attributed to several factors: (i) Au is not present, (ii) Au is present but passivated, either by thiol or Pt enrichment on the surface, or (iii) the surface coverage of Au is insufficient to significantly contribute to the voltammetry of the modified substrate. XPS measurements confirm the presence of Au, and the potential window used in the experiment should not result in Au remaining passivated. In Pt and Au alloy nanoparticle systems, Au typically shows surface enrichment, making it unlikely that Au is buried beneath Pt.

It is likely then that the measured substrate does not have sufficient Au coverage to be detected electrochemically. The incomplete recovery of current densities for the modified substrate may be attributed to the presence of some Au and the blocking of Pt active sites by thiol, as the potential window used did not extend into the region required for thiol desorption from Pt.

5.4 Conclusion

The aim of this chapter was to investigate the immobilisation of Au nanoparticles on Ag and Pt substrates, focusing on their stability, structural evolution, and the resulting electrochemical behaviour of the modified surfaces. It was anticipated that the stronger Au-S bond, compared to both Pt-S and Ag-S, would result in thiol-protected Au NPs on the substrate. However, it was unclear if the entropic driving force would dominate and drive the thiol redistribution effect, leading to the exposure of the Au cores.

The system of Ag NPs on Au exhibited exposed Ag cores, with new voltammetric features attributed to alloying behaviour. Given the difference in metal-thiol bond strengths, it was uncertain if the same dynamics would apply to the Au NP-Ag system. Cyclic voltammetry of the Au-modified Ag substrate did not indicate the presence of electrochemically active Au cores. In both 0.1 M NaOH and 0.1 M glycerol, the first voltammograms showed features that deviated from those of a clean Ag electrode. However, these features were not specific to Au, as they were also observed in the modification of Ag electrodes with Pt NPs. It is likely that these features were due to interactions between thiols and Ag, as this was the common component in both systems. While electrochemical characterisation suggested the presence of some material on the Ag surface, this material is likely intact, thiol-protected Au NPs.

For Au NPs on Pt, XPS confirmed the successful deposition of Au NPs onto the surface, with thiols bound to the Pt substrate. However, the data also indicated that the Au remained partially protected by thiols. Cyclic voltammetry covered the potential range in which thiol desorption from Au is expected, but the Au NPs did not exhibit distinct electrochemical behaviour, unlike the reverse system of Pt NPs on Au. It was determined

that the Au surface coverage on Pt was insufficient to contribute noticeably to the voltammetry. The surface modification appears to have resulted in partially thiol-protected Au, and a higher concentration of Au NPs may yield electrochemical contributions in future experiments.

For Au NPs on both Ag and Pt substrates, it remains unclear whether the Au features represent intact NPs, monoatomic islands, or intermediate structures. Further investigation, such as in situ STM, would be valuable to confirm the structural state of the Au and verify the immobilisation of the particles onto the substrates. If we assume successful immobilisation of Au for both substrate materials, the stability of Au NPs in both systems appears to be dictated by the strong Au-S bond, which prevents significant thiol redistribution. While this stabilisation preserves the integrity of the NPs, it also limits their electrochemical activity. Future work should seek to explore higher NP concentrations and utilise advanced surface characterisation techniques to provide a more comprehensive understanding of these systems.

5.5 References

1 S. Hosseini, N. Alsiraey, A. J. Riley, T. Zubkov, T. Closson, J. Tye, N. Bodappa and Z. Li, *Langmuir*, 2018, **34**, 15517–15525.

2 N. Awais, P. Rodriguez and T. Albrecht, *ECS Trans.*, 2020, **97**, 885.

3 D. Y. Petrovykh, H. Kimura-Suda, A. Opdahl, L. J. Richter, M. J. Tarlov and L. J. Whitman, *Langmuir*, 2006, **22**, 2578–2587.

4 H. Qian and R. Jin, *Chem. Mater.*, 2011, **23**, 2209–2217.

5 L. D. Burke and P. F. Nugent, *Gold Bull.*, 1997, **30**, 43–53.

6 S. Hebié, T. W. Napporn, C. Morais and K. B. Kokoh, *ChemPhysChem*, 2016, **17**, 1454–1462.

7 S. Chen, B. Wu and C. Cha, *J. Electroanal. Chem.*, 1996, **416**, 53–59.

8 M. López Teijelo, J. R. Vilche and A. J. Arvia, *J. Appl. Electrochem.*, 1988, **18**, 691–698.

9 T. P. Dirkse and D. B. De Vries, *J. Phys. Chem.*, 1959, **63**, 107–110.

10 J. F. Gomes and G. Tremiliosi-Filho, *Electrocatalysis*, 2011, **2**, 96–105.

11 M. Schweizer and D. M. Kolb, *J. Electroanal. Chem.*, 2004, **564**, 85–91.

12 G. Guisbiers, R. Mendoza-Cruz, L. Bazán-Díaz, J. J. Velázquez-Salazar, R. Mendoza-Perez, J. A. Robledo-Torres, J.-L. Rodriguez-Lopez, J. M. Montejano-Carrizales, R. L. Whetten and M. José-Yacamán, *ACS Nano*, 2016, **10**, 188–198.

13 T. Ishida, N. Choi, W. Mizutani, H. Tokumoto, I. Kojima, H. Azehara, H. Hokari, U. Akiba and M. Fujihira, *Langmuir*, 1999, **15**, 6799–6806.

14 D. G. Castner, K. Hinds and D. W. Grainger, *Langmuir*, 1996, **12**, 5083–5086.

15 R. I. Carey, J. P. Folkers and G. M. Whitesides, *Langmuir*, 1994, **10**, 2228–2234.

16 R. G. Nuzzo, B. R. Zegarski and L. H. Dubois, *J. Am. Chem. Soc.*, 1987, **109**, 733–740.

17 V. Ponec and G. C. Bond, *Catalysis by Metals and Alloys*, Elsevier Science, 1995.

18 D. Zhan, J. Velmurugan and M. V Mirkin, *J. Am. Chem. Soc.*, 2009, **131**, 14756–14760.

19 P. Daubinger, J. Kieninger, T. Unmüssig and G. A. Urban, *Phys. Chem. Chem. Phys.*, 2014, **16**, 8392–8399.

20 Y. Kwon, Y. Birdja, I. Spanos, P. Rodriguez and M. T. M. Koper, *ACS Catal.*, 2012, **2**, 759–764.

21 O. Malis, M. Radu, D. Mott, B. Wanjala, J. Luo and C.-J. Zhong, *Nanotechnology*, 2009, **20**, 245708.

22 G. C. Bond, C. Louis and D. T. Thompson, *Catalysis by Gold*, Imperial College Press, 2006.

23 M. A. Floridia Addato, A. Rubert, G. Benítez, E. Zelaya, G. Cabello, A. Cuesta, J. E. Thomas, A. Visintín, R. C. Salvarezza and M. H. Fonticelli, *J. Phys. Chem. C*, 2013, **117**, 7589–7597.

6. Conclusions and Future Work

In Chapter 1, the background work highlighting the instability of thiolated Au nanoparticles (NPs) on Au (111) substrates was introduced. The immobilisation of Au NPs of two different sizes, the disintegration of their ligand shells, and the subsequent formation of Au nanoislands have been well characterised through electrochemistry, in-situ STM imaging, and DFT calculations. The work presented in this thesis aimed to expand upon these studies by exploring systems with different substrate and nanoparticle materials. The goal was to evaluate the stability and structural evolution of nanoparticles upon immobilisation in these mixed-metal systems. Combinations of Ag NPs on Au and Pt, Pt NPs on Au and Ag, and Au NPs on Pt and Ag were investigated using STM, XPS, and cyclic voltammetry techniques.

An important consideration that arose during the interpretation of results is the potential for the presence of excess thiol in the nanoparticle systems synthesised using cathodic corrosion methods—namely Pt and Ag particle solutions. As such, the interpretation of electrochemical results must also consider the potential influence of free thiols on surface behaviour, particularly regarding current suppression and redox peak emergence. This limitation was particularly relevant in the Ag–Pt and Pt–Ag systems, where STM or XPS confirmation of structural decomposition was not available to support interpretation. To address this limitation in future studies, further experiments should include characterisation of NP suspensions using spectroscopic techniques or surface tension measurements to confirm the absence (or quantify the extent) of excess thiol. Additionally, future electrochemical studies should compare the voltammetric

behaviour of nanoparticle-modified electrodes to that of clean electrodes modified with thiols alone, to decouple the contributions from nanoparticle decomposition and thiol-induced passivation. With this caveat in mind, we conclude our findings for each system under the assumption that free thiol is negligible.

The Pt-Ag system was explored in Chapters 3 and 4. Both metals exhibit a significant miscibility gap in their bulk states, and while alloy nanoparticle synthesis has been reported for the two metals, the stability of the resulting particles is highly dependent on factors such as metal ratios and particle size. Electrochemical characterisation of the Ag NP-modified Pt substrate revealed contributions of both Pt and Ag-specific voltammetric features, though the Ag contribution was minimal. Still, this indicated that both the entropic driving force and the stronger Pt-S bond played a role in driving the thiol redistribution process, resulting in exposed, electrochemically active Ag. Importantly, no voltammetric features were observed that could not be attributed to either metal, suggesting that alloying between Pt and Ag did not occur, consistent with the expectation based on their bulk immiscibility. In the inverse scenario, with Pt NPs immobilised on Ag, no Pt-specific electrochemistry was observed in either alkaline media or in the presence of glycerol. The lack of electrochemically active Pt, combined with the incomplete recovery of the Ag surface, suggested the presence of thiol-protected Pt particles on the substrate. This outcome highlighted the role of the stronger Pt-S bond relative to the Ag-S bond in preventing the opening of the thiol shell and the exposure of Pt cores. In both systems, direct evidence of successful nanoparticle deposition was lacking, with only indirect evidence provided by the electrochemical data.

Chapters 3 and 5 reported the characterisation of the Au-Ag system. These metals are known to be miscible, forming alloys both in bulk and at the nanoscale. Beyond investigating the structural stability of nanoparticles of each metal on the other, a key question was whether the alloying behaviour typically observed for Au and Ag would manifest when the two metals existed in different size regimes, namely one in the bulk, the other at the nanoscale.

For Ag NPs immobilised on an Au substrate, STM imaging revealed the formation of monoatomic Ag islands, indicating that the Ag particles were unstable upon immobilisation. XPS binding energy values further suggested that the thiol binding in the modified system was distinct from that observed on each metal individually. Electrochemical characterisation of the mixed-metal system showed voltammetric contributions from Au and Ag, as well as features not assignable to either metal, providing evidence of potential alloying between Au and Ag. The exposure and decomposition of Ag NPs align with expectations, as the entropic favourability of the larger Au substrate surface, combined with the stronger Au-S bond, would drive thiol migration from the Ag NP surface. Interestingly, this study demonstrated that the miscibility of Au and Ag, well established from bulk to nanoscale, also extends to mixed-size regimes. In the reverse system, where Au NPs were immobilised on an Ag substrate, no Au-specific electrochemistry was observed. This was consistent with the enthalpic factor hindering thiol migration due to the stronger Au-S bond compared to the Ag-S bond. It is noteworthy that in this system, the enthalpic factor dominated over entropy in determining the stability of the Au NPs. However, the lack of direct evidence for successful NP deposition in this system highlights the need for caution in interpreting these observations.

The Au-Pt system was characterised in Chapters 4 and 5. The Pt NPs on Au system proved to be particularly interesting, as Pt was shown to undergo a thiol redistribution effect, forming monoatomic Pt islands and contributing significantly to the overall electrochemistry of the modified surface. Both entropic and enthalpic driving forces were likely at play in this system, and both favoured the exposure of Pt cores through the migration of thiols. The observation that Pt exhibited electrochemical features distinct from those of the Au substrate aligns with the known miscibility gap between the two materials, preventing alloying under these conditions. In the reverse system, where Au NPs were immobilised on Pt, it was observed that the Au NPs remained partially protected by thiols, despite some thiol migration to the Pt substrate, as evidenced by XPS. The electrochemical properties of the modified substrate reflected only Pt-specific activity, indicating that the Au NPs were not sufficiently exposed to contribute electrochemically to the system. To better understand the stability of the Au NP cores in this system, further investigation is needed to determine the degree of decomposition of the Au features and whether their partial passivation prevents complete disintegration.

It is important to consider that, for all systems investigated, we are effectively examining a snapshot of the modified surface. It remains unclear whether the systems had reached thermodynamic equilibrium or whether further structural evolution of the particles would occur over time. All characterisation was conducted approximately 24 hours after modification, making the collected "snapshots" comparable across systems, but not necessarily representative of the final state of the surfaces. Further characterisation of these systems would greatly benefit from high-resolution in situ STM imaging. This would not only confirm the presence of nanoparticles on the surfaces where we were not able to do so, but also provide valuable insights into the structural changes that immobilised

particles may undergo over longer timescales. Such imaging could also reveal the formation of thiol domains post-deposition, supporting interpretation of surface passivation and migration behaviour.

Systems of particular interest for future investigation include Ag NPs on Au, Pt NPs on Au, and the reverse configurations of each for comparison. Further work should focus on employing Ag and Pt nanoparticles with well-defined particle and ligand shell structures, enabling in-depth characterisation of the energetics of the decomposition processes, similar to the studies conducted for the Au NP-Au system. A comprehensive understanding of these modified surfaces, particularly as they exhibit electrochemical properties distinct from their bulk counterparts, could provide valuable insights for designing tailored functional surfaces. Such advancements could open new opportunities for applications in catalysis, sensing, and other areas where the unique properties of these metals at the nanoscale can be exploited.